

THEORY, DESIGN, AND APPLICATION OF ELECTRODYNAMIC TRANSFORMERS

By

SHUO CHENG

A DISSERTATION PRESENTED TO THE GRADUATE SCHOOL  
OF THE UNIVERSITY OF FLORIDA IN PARTIAL FULFILLMENT  
OF THE REQUIREMENTS FOR THE DEGREE OF  
DOCTOR OF PHILOSOPHY

UNIVERSITY OF FLORIDA

2011

© 2011 Shuo Cheng

To my wife, Dandan

## ACKNOWLEDGMENTS

This work was supported in part by DARPA Grant N66001-09-1-2095 and ARO Grant W911NF-09-1-0511.

I would like to thank my advisor Dr. David P. Arnold for his continuous support and guidance. His mentorship has not only strengthened my technical skill, but also provided me enormous space to think creatively. Dr. Arnold has also been a thoughtful friend and even like a father throughout my memorable life as a graduate student.

I am grateful to my other committee members Dr. Louis Cattafesta, Dr. Toshi Nishida, and Dr. Jenshan Lin for their time and effort evaluating my work and their valuable improvement suggestions.

I am greatly in debt to the current and previous members of Interdisciplinary Microsystem Group (IMG). Part of this work has been inspired by interesting discussions with Dr. Vinod Challa, Dr. Naigang Wang, Dr. Alex Phipps, Dr. Janhavi Agashe, Yaxing Zhang, and Yuan Rao. I obtained much assistance on experiments from Rutvik Sathe, Raj Natarajan and Vikram Divakar. The microfabrication of the device could not have been successful without the help from Yaxing Zhang, Justin Zito, Ololade Oniku, and Shashank Sawant. I am thankful to Jessica Meloy, Dylan Alexander, Raphael Puzio, and all other IMG committee members for their consistent effort maintaining the operation of all the IMG labs. I also want to appreciate Al Ogden, Bill Lewis, and David Hayes at the Nanoscale Research Facility for their kind technical support on the microfabrication processes.

During the most stressful time of my research, I have been supported by the encouragements from my parents Jinfeng Chen and Zhenping Cheng, and parents-in-law Shuchun Yu and Yafan Xu. I have been fortunate enough to marry my beloved wife

Dandan Xu. I owe everything to her selfless love that nurtured the most delightful time of my life.

# TABLE OF CONTENTS

	<u>page</u>
ACKNOWLEDGMENTS .....	4
LIST OF TABLES .....	9
LIST OF FIGURES .....	10
LIST OF ABBREVIATIONS .....	13
ABSTRACT .....	14
CHAPTER	
1 INTRODUCTION .....	16
1.1. Basic Concepts .....	17
1.2. Motivation .....	20
1.2.1. The Progress of Power Electronic System Power Density Improvement.....	20
1.2.2. Limitation of Existing Magnetic Components .....	22
1.2.3. Alternative Operating Mechanism for Transformers .....	23
1.2.4. Potential Advantages of Electrodynamic Transformers .....	26
1.3. Historical Review .....	28
1.4. Research Objectives and Overview .....	31
2 THEORETICAL BACKGROUND .....	37
2.1. Transducer Modeling Overview .....	37
2.2. Lumped Element Modeling Fundamentals.....	39
2.3. Lumped Element Model within Different Energy Domains .....	43
2.3.1. Mechanical Domain .....	43
2.3.2. Electrical Domain.....	44
2.3.3. Magnetic Domain .....	45
2.4. Inter-domain Interactions .....	50
2.4.1. Electromagnetic Transduction .....	51
2.4.2. Electrodynamic Transduction .....	52
2.5. Modeling Examples.....	55
2.5.1. Lumped Element Model of Inductively Coupled Coils .....	55
2.5.2. Lumped Element Model of an Electrodynamic Transducer.....	58
3 ELECTRODYNAMIC TRANSFORMER THEORY .....	70
3.1. Device Overview .....	70
3.2. Lumped Element Model of Electrodynamic Transformers .....	72
3.3. Electrodynamic Transformer Model Analysis .....	74

3.3.1. Conditions for Ignoring the Inductive Coupling .....	74
3.3.2. Analysis of the Simplified Model .....	77
3.3.2.1. Voltage Gain and Power .....	77
3.3.2.2. Power Efficiency .....	79
3.3.2.3. Power Capacity .....	80
3.4. Performance Limits and Scaling Laws of Electrodynamic Transformers .....	85
3.4.1. Limit of Power Efficiency .....	85
3.4.2. Limit of Power Density .....	89
3.5. Comparison of Electrodynamic Transformers with Other Transformer Technologies .....	93
3.5.1. Comparison with Electromagnetic Transformer.....	93
3.5.2. Comparison with Piezoelectric Transformer .....	97
4 MACROSCALE DEVICE AND MODEL VALIDATION .....	107
4.1. Device Construction.....	107
4.2. Parameter Extraction .....	108
4.2.1. Standalone Measurement of the Coils.....	108
4.2.2. Extraction of the Mechanical and Electromechanical Parameters .....	112
4.3. Performance Prediction and Verification.....	115
4.4. Summary .....	120
5 MICROSCALE DEVICE AND EXAMPLE APPLICATION.....	132
5.1. Device Design.....	132
5.2. Device Fabrication .....	134
5.3. Device Testing.....	135
5.4. Application Example .....	139
5.4.1. Background .....	139
5.4.2. Demonstration of Resonant Inverter Using Electrodynamic Transformer .....	141
5.5. Summary and Discussion .....	142
6 CONCLUSION.....	157
6.1. Summary of Research Contributions.....	157
6.2. Summary of Major Conclusions .....	157
6.3. Future Work .....	159
APPENDIX	
A ELECTRODYNAMIC TRANSDUCTION AND FARADAY'S LAW OF INDUCTION.....	162
B PROPERTIES OF THE GYRATOR.....	165
LIST OF REFERENCES .....	167

BIOGRAPHICAL SKETCH..... 177

## LIST OF TABLES

<u>Table</u>		<u>page</u>
2-1	List of general representations of elements in a transducer lumped element model.....	62
2-2	Conjugate power variables and fundamental elements in different energy domains.....	63
3-1	List of common conductive materials' resistivity and density.....	101
4-1	List of extracted parameters.....	122
B-1	Properties of the gyrator.....	165

## LIST OF FIGURES

<u>Figure</u>	<u>page</u>
1-1 Pictures of switches.....	33
1-2 Block diagram of an electrodynamic transformer.....	33
1-3 Schematic illustration of an example electrodynamic transformer structures. ....	33
1-4 Microprocessor power density increase over time.....	34
1-5 Progress of power converter power density. ....	35
1-6 Trends of passive device size.....	35
1-7 Schematic of a Rosen type PT. ....	36
1-8 AC-DC rotary converters in the powerhouse for the Baltimore Belt Line of the Baltimore and Ohio Railroad, part of the first mainline railroad electrification in 1895.....	36
2-1 One-port and two-port elements.....	63
2-2 Transformer and gyrator.....	64
2-3 Electromagnetic coupling. ....	64
2-4 Illustration of electrodynamic transduction.....	64
2-5 Electrodynamic transduction with non-uniform magnetic field and arbitrary coil. ....	65
2-6 Electrodynamic transduction configuration with straight conductor. ....	65
2-7 Electrodynamic transduction configuration with circular conductor and radial field.....	66
2-8 Illustration of a pair of inductively coupled coils.....	67
2-9 Lumped element model of the inductively coupled coils.....	67
2-10 Transforming the developed lumped element model to the canonical equivalent circuit model of the inductively coupled coils.....	68
2-11 Electrodynamic generator in the example. ....	69
2-12 Lumped element model of the electrodynamic generator.....	69

3-1	Three types of ET topologies.....	102
3-2	Complete lumped element model of an electrodynamic transformer.....	103
3-3	Simplified lumped element model of an electrodynamic transformer where only electrodynamic coupling is considered. ....	103
3-4	Contour plot of efficiency vss coupling strengths.....	104
3-5	Strong uniform magnetic field created by a Halbach cylinder.....	104
3-6	ET structure for power density estimation. ....	105
3-7	Lumped element model of an electromagnetic transformer.....	105
3-8	Lumped element model of a piezoelectric transformer.....	106
3-9	Lumped element models with mechanical domain reflected to the primary electrical domain.....	106
4-1	A picture of the macroscale prototype .....	123
4-2	The series resistance and inductance of the primary coil .....	123
4-3	The series resistance and inductance of the secondary coil .....	124
4-4	Curve fitting of the voltage gain frequency response.....	125
4-5	Force vs. displacement of the spring.....	126
4-6	Force vs. current for the primary and secondary coils.....	127
4-7	Transduction coefficient variation with displacement.....	128
4-8	Transient response of the mechanical resonator.....	128
4-9	Circuit model simulated in LTSpice. ....	129
4-10	Measured and predicted open-circuit voltage gain frequency response.....	129
4-12	Measured and model predicted output power vs. load resistance.....	131
5-1	Schematic of the microscale electrodynamic transformer. ....	145
5-2	Finite element simulation of the magnetic assembly. ....	145
5-3	Fabrication process of the microfabricated part of the electrodynamic transformer (side view). ....	146

5-4	Top-view photograph of the microfabricated beam structures of the electrodynamic transformer. ....	147
5-5	Measured impedance of the top and the bottom beams.....	147
5-6	The microscale electrodynamic transformer under test on a probe station. ....	148
5-7	Open-circuit voltage gain frequency response with different beams as the primary conductor.....	149
5-8	Input and output power, and efficiency measurements at different load resistances. ....	150
5-9	Block diagram of a resonant converter. ....	150
5-10	Resonant converters using a piezoelectric transformer.....	151
5-11	Circuit diagram of an LLC-PRC resonant inverter showing components that can potentially be replaced by an electrodynamic transformer. ....	151
5-12	Implementation of LLC-PRC resonant inverter using an electrodynamic transformer. ....	152
5-13	Waveforms captured for the resonant inverter.....	153
5-14	Input/output power and efficiency of the resonant inverter at different load resistances. ....	154
5-15	Transverse flux density vs. distance from the magnet surface. ....	155
5-16	Electrodynamic transformer with tapered beam. ....	156

## LIST OF ABBREVIATIONS

EMF	Electromotive force
EMI	Electromagnetic interference
EMT	Electromagnetic transformer
ET	Electrodynamic transformer
FEM	Finite element model
LEM	Lumped element model
LLC-PRC	Parallel resonant converter using two inductors and one capacitor
LTI	Linear-time-invariant
MEMS	Microelectromechanical system
MMF	Magnetomotive force
PT	Piezoelectric transformer
RF	Radio frequency
ZCS	Zero-current switching
ZVS	Zero-voltage switching

Abstract of Dissertation Presented to the Graduate School  
of the University of Florida in Partial Fulfillment of the  
Requirements for the Degree of Doctor of Philosophy

THEORY, DESIGN, AND APPLICATION OF ELECTRODYNAMIC TRANSFORMERS

By

Shuo Cheng

December 2011

Chair: David P. Arnold

Major: Electrical and Computer Engineering

This dissertation explores a two-port electromechanical device coined an “electrodynamic transformer (ET).” An ET is an energy transfer device that consists of two independent electrical coils that are electromechanically coupled to a mechanical oscillator via a static magnetic field. Electrical energy input to the primary coil is converted to mechanical motion via electrodynamic transduction. The mechanical motion is then converted back to electrical energy in the secondary coil.

Lumped element modeling techniques are used to investigate the functional behavior and scaling of the ET. Using these models, the ET is compared with a conventional electromagnetic transformer (EMT) and a piezoelectric transformer (PT). The study shows that the ET can potentially achieve higher power efficiency than an EMT and potentially higher power density, as well as superior noise isolation and better long term reliability than a PT. In addition, the ET has favorable scaling for improved efficiency and power density at the microscale.

The model is experimentally validated with a macroscale ET prototype. A microscale ET is also fabricated and characterized, which shows promising performance. The utility of the ET is also demonstrated in a functional power converter

application using the microscale prototype. A compact resonant dc/ac inverter is built that takes advantage of the resonant behavior of the ET. The results show promise for future adoption of ET and encourages continued research in this area.

## CHAPTER 1 INTRODUCTION

Throughout scientific history, one can find interesting examples of obsolete technologies that have been revived by the “push” of new enabling discoveries or the “pull” of new applications. For example, consider a classical mechanical relay, which employs electromechanical actuation to open or close a circuit. The rapid growth of semiconductor transistors in the mid-20<sup>th</sup> century made such mechanical switches obsolete in most integrated circuits. However, the rise of microelectromechanical systems (MEMS) and the associated manufacturing technologies has stimulated new applications for advanced micro-switches, especially in radio frequency (RF) integrated circuits [1]. [Figure 1-1](#) illustrates the progress of relay switch technology over the past 150 years.

In the above example, an old technology (the relay switch) was reinvigorated by a new technology (MEMS microfabrication). This dissertation investigates another “old” technology, which has similar potential for re-invention. The old technology here is an outdated mechanical power converter concept that uses mechanical motion to transfer and convert electrical power. Using rotating machinery, such mechanically based power converters were once commonplace for use in electrical power conversion in times before modern power electronics. Like the MEMS-enabled micro-switched mentioned above, this dissertation explores a new implementation of the concept, enabled by advanced microelectromechanical design and fabrication technologies. A magnetically based, resonating electromechanical device—coined an “electrodynamic transformer (ET)”—is introduced and explored both theoretically and experimentally. This effort is

driven by the application goal of improving the power density of modern power converters.

This chapter is organized as follows: [Section 1.1](#) introduces basic electromechanical transducer concepts, electrodynamic transduction, and the working principle of the ET; [Section 1.2](#) presents a fuller description of the motivation for the research; [Section 1.3](#) reviews the historical background related to the research topic; [Section 1.4](#) summarizes the objectives of the research and provides an overview of the dissertation.

### **1.1. Basic Concepts**

Electrical and mechanical energy are two of the most common forms of energy that have served the world over the last century. Electrical energy is more easily transmitted over long distance, and can be directly used to achieve many functionalities, such as lighting, heating, computing, etc. However, stable, manageable electrical energy sources are not directly found in nature. On the other hand, mechanical energy is abundant in the environment in the forms of water flow, wind, tides, ocean waves, etc. However, the transmission of mechanical energy over long distance is typically difficult and inefficient. In modern times, the direct use of mechanical energy finds fewer applications than that of electrical energy.

Electromechanical and mechano-electrical devices (commonly known as machines, motors, generators, transducers, etc.) are used to bridge the gap between the two energy domains and take advantage of both. Electromechanical devices convert electrical energy to mechanical domain, and mechano-electrical devices generate electrical energy from mechanical energy. In the literature [2-4], the generic term "transducer" is used to describe both types of energy conversion devices, and this

dissertation adopts the same terminology. Also, unless otherwise stated, the term "electromechanical" will be used throughout the work to represent energy conversion in both directions.

Electromechanical energy conversion can be implemented through many different transduction mechanisms. The most ubiquitous—electrodynamic energy conversion—was inspired by Ørsted's first discovery of electrodynamic interactions in 1821. It makes use of the interaction between moving electric charge and a magnetic field. An electric charge moving in the reference frame of a magnetic field is subject to a Lorentz force. Depending on whether the electric charge movement is externally driven by electric current or mechanical motion of the conductor, the Lorentz force converts electrical energy to mechanical energy (as in a motor) or mechanical energy to electrical energy (as in a generator). The latter is also interpreted as Faraday's Law of Induction. More detailed description of electrodynamic transduction is provided in [Appendix A](#).

In the modern literature, electrodynamic transduction is often referred to as magnetic, inductive, or electromagnetic transduction. To the author's knowledge, there is little agreement in the community regarding to the difference between these terminologies. However, the term "electrodynamic" has been used extensively in acoustic community [5-8] and is clearly defined as an electromechanical transduction mechanism where "motor and generator action are produced by the current in, or the motion of, an electric conductor located in a fixed transverse magnetic field" [9]. As explained in [Appendix A](#), Faraday's Law of Induction divides the induced voltage or EMF into two components: motional EMF and transformer EMF. The former is a result of the relative motion between the conductor and the magnetic field source, while the

latter is a result of the variation of the magnetic field generated by the field source with time (e.g. time-varying current in an electromagnet, or temperature-induced magnetization variation in a permanent magnet). Electrodynamical transduction only deals with the motional EMF, because of the "fixed transverse magnetic field." In this dissertation, the term "inductive" is reserved for the phenomenon where only transformer EMF is in effect, for example, the mutual inductive coupling between two coils, which is an electrical-magnetic-electrical interaction.

Having driven the world for almost two centuries, electrodynamic transducers are still expanding into new applications such as electric vehicles [6, 10], renewable power generation [11-13], energy storage [14-16], etc. Offering the advantages of high power density, direct energy conversion, contactless force interaction, and numerous other benefits, electrodynamic transducers have maintained a long-lasting predominant role in electromechanical energy conversion.

This dissertation investigates the use of electrodynamic transducers to transfer electrical energy between two electrically insulated circuits. The ET device concept, shown in [Figure 1-2](#), is a combination of an electrodynamic motor and an electrodynamic generator, where the mechanical motions of the two are shared. In operation, the electrical current in one circuit creates a mechanical motion (Lorentz force), which is used to induce a voltage on the other circuit (Faraday's Law). As a net effect, electrical energy may be transferred from the first circuit to the second. The devices explored here use oscillating (vibrating) motors and generators, as opposed to the rotating systems used in classical electromechanical power converters (more on this in [Section 1.3](#)).

Figure 1-3 shows an example configuration of the ET. In this configuration, the primary and the secondary coils are attached to the frame, while the magnet is attached to the spring and free to oscillate. An ac current in the primary coil drives the magnet to oscillate, the motion of which generates a voltage in the secondary coil.

## **1.2. Motivation**

The research effort on the ET is primarily motivated by the ever growing demand for compact, power-dense power electronics solutions for the modern electronic systems. The ET is explored for its potential as a compact, high-power-density alternative to a conventional electromagnetic transformer (EMT). In this section, a general description of the challenges for increasing a power converters' power density is first presented. Next, a specific discussion on the power density limits of magnetic components (inductors and transformers) is provided. Then, the use of electromechanical transducers as an alternative power transformer mechanism is described as a potential solution to overcome the power-density challenges. Furthermore, an existing implementation of an electromechanical approach—the piezoelectric transformer (PT)—is described. Last, the potential benefits of the ET compared to the PT are discussed.

### **1.2.1. The Progress of Power Electronic System Power Density Improvement**

The rapid progress of integrated circuit technology has enabled implementation of more sophisticated systems (e.g. portable electronics, telecommunication systems, medical devices, etc.) within more compact physical form factors. However, power consumption of these systems has not scaled proportionally with the size. In fact, to fulfill their increasing transistor density and ever-growing functionality, many modern electronic systems are becoming more and more power hungry and thus power dense.

For example, [Figure 1-4](#) shows a progress chart of the microprocessor power density, which is almost doubled every two years, and is estimated to reach  $1 \text{ kW/cm}^2$  in 2015 [17]. The need for more power in smaller packages places enormous demands on the supporting power systems. For portable devices, energy sources such as batteries must provide high energy- and power-density. Similarly, the demand for compact power conversion/management electronics with high power density has never been stronger.

The past few decades have seen a dramatic improvement in power handling capability of power converters. As can be seen from [Figure 1-5](#), the power density of power converters has roughly doubled every ten years since 1970, reaching over  $100 \text{ W/cm}^3$  during the last decade [18]. The major space occupiers in a modern power converter system are the passives, specifically inductors, capacitors, and transformers.

To reduce the physical size (which generally corresponds to the inductance or capacitance), switching power supplies are being designed with higher and higher operating frequencies, as shown in [Figure 1-6](#). Over the last decade, the operating frequency of passive components has been increased by 20x from  $\sim 1 \text{ MHz}$  to  $20 \text{ MHz}$ . However, to transfer the same amount of power, a 2x size reduction of these passive components requires roughly a 10x increase in operating frequency. Increasing the frequency is not an eternal (or easy) solution for increasing the power density of a converter. As the frequency increases, more power loss occurs in the transistor switches, magnetic components, and other system components where power loss is an increasing function of the frequency.

Due to these frequency-related loss mechanisms, as well as material limitations and manufacturing hurdles, further reduction of passive components size will be more

and more difficult. It has been predicted that the size of passive components will become one of the major barriers for further improvement of converter power density [19]. In order to maintain the long lasting trend and meet the relentless demands for modern applications, industry is calling for broader scope research efforts that may lead to revolutionary breakthroughs.

### 1.2.2. Limitation of Existing Magnetic Components

The development of compact, high-power-density, low-loss magnetic components (inductors and transformers) has been limited by the properties of soft magnetic core materials [18]. The ideal material needs to possess high saturation flux density to maximize the density of magnetic energy storage. In general, magnetic energy density stored in a core is proportional to the square of the saturation flux density.

Assuming linear magnetic properties, the magnetic energy density in a magnetic core material is given by

$$S_{mag} = \frac{B_{sat}^2}{2\mu_r\mu_0} \quad (1-1)$$

where  $B_{sat}$  is the saturation flux density of core,  $\mu_r$  is the relative permeability of the core, and  $\mu_0$  is the free space permeability ( $4\pi \times 10^{-7}$  H/m). A maximum saturation flux density of 2.4 T may be achieved in certain iron-cobalt alloys. Meanwhile, high permeability is required to achieve high self or mutual inductance, and minimize unwanted magnetic flux leakage and electromagnetic interference (EMI). Therefore, the effective relative permeability of a magnetic core (considering added air gap) should be no less than 10. With these aggressive assumptions, the maximum magnetic energy density is only on the order of 100 kJ/m<sup>3</sup>.

Besides energy density, the requirement for overall efficiency needs high resistivity and low coercivity in order to minimize eddy current loss and hysteresis loss, respectively. Last, but not the least, the fabrication of the magnetic material needs to be compatible with the manufacturing process of the whole device (e.g. wafer-level microfabrication for on-chip micro-inductors). The combination of all these requirements presents a challenge to the development of high-performance, power-dense, small-scale magnetic inductors and transformers.

Properties of the magnetic materials place a fundamental limit to the performance of the magnet components and the overall power electronic system. To overcome this material barrier, air-core devices have been advocated by some researchers [18, 20]. However, without the flux concentration of the magnetic core, the achievable range of self or mutual inductance is limited by the available area for the air-core winding and the tolerable coil resistance. In addition, the unconfined magnetic flux presents potential EMI problems [21]. Shielding materials can be introduced to mitigate EMI, but these shields create similar core loss issues. Since the operating frequency of the air-core magnetic components may be higher than cored components, the eddy current loss and hysteresis loss in nearby shielding material can be quite significant.

### **1.2.3. Alternative Operating Mechanism for Transformers**

Transformers are devices that transfer electric energy between two or more electrically insulated circuits. Although the design and fabrication technology of transformers has been continuously renovated, the fundamental working principle of the most widely used transformers has not changed since Faraday's first ring transformer was built in 1831 [22]. The simple, reliable, and efficient electromagnetic-induction-based transformers have been "too perfect" to be challenged for over a hundred years.

However, due to the urge for size reduction, modern industry has begun to regard the EMT as one of the biggest hurdles for power system design. It is suggested here that the inherent magnetic material limitations of conventional EMTs (as discussed in 1.2.2) may be better overcome by investigating energy transfer devices with fundamentally different operating mechanisms.

The invention of the PT in the mid-20<sup>th</sup> century [23-25] opened a new path for small-size, high-power-density transformers. This revolutionary concept utilizes mechanical energy instead of magnetic energy as the energy transfer medium, along with piezoelectric instead of electromagnetic transduction as the energy conversion mechanism. A PT converts electrical energy first into mechanical vibration using the reverse piezoelectric effect; this mechanical energy is then converted back to electrical energy using the direct piezoelectric effect.

Figure 1-7 shows the schematic of a “Rosen type” PT. In this device, the piezoelectric material is polarized in two directions. When a voltage is applied to the primary electrode, a stress along the thickness direction is induced by the left part of the material, resulting in a change in thickness. The change in thickness induces a change in the length, which excites the right part of the material, generating a voltage on the secondary electrode. PTs usually operate at the mechanical resonant frequency (typically 10 kHz – 10 MHz) to achieve high efficiency, voltage gain, and output power.

The key benefits of PTs include small size, low EMI, non-flammability and high voltage conversion ratio [26]. There are two categories of PTs: step-up (high voltage) PTs and step-down (low voltage) PTs. Step-up PTs have been used to generate high voltage in lighting applications [27-30]. Step-down PTs have also being investigated for

dc power supply applications [31]. Although certain limitations such as comparatively high cost, low power density, and common-mode noise problems (will be discussed in 1.2.4) restrict their wide application, PTs have clearly demonstrated the promise of energy transfer and electrical energy conversion through mechanical vibration.

In general, mechanical energy storage can achieve energy density orders of magnitude higher than magnetic energy storage in a core. A higher energy density implies that more energy can be processed per unit volume per cycle, which for operation at a given frequency leads to high power density.

To demonstrate this, consider mechanical potential energy stored in a deformed material (as in the case of PTs) with Young's modulus of  $E$ . Assuming linear mechanical properties, when the material is subject to the maximum yield stress  $T_{max}$ , the energy density in this material is given by

$$S_{mech} = \frac{kx_{max}^2}{2V} = \frac{T_{max}^2}{2E}, \quad (1-2)$$

where  $k$  is the stiffness,  $x_{max}$  is the maximum deformation,  $V$  is the volume of the material. For example, the maximum energy density in PZT (lead zirconate titanate), the most common piezoelectric material, is on the order of 1 MJ/m<sup>3</sup>. In silicon, the maximum energy density can reach 100 MJ/m<sup>3</sup>. This is much higher than the maximum energy density in a magnetic core of an EMT, which is only on the order of 100 kJ/m<sup>3</sup>, as estimated in [Section 1.2.2](#).

In addition to higher energy density, the use of mechanical resonance provides frequency selectivity. The mechanical resonance in a PT magnifies the desired frequency content while suppressing out-of-band spectral content. This additional property is very useful in applications such as resonant converters [32-34]. The

embedded mechanical resonator of a PT eliminates the need for resonant tank (typically implemented using at least one inductor and one capacitor) and significantly reduces the overall size of the system. Moreover, the quality factor (will be explained later in [Section 1.3](#)) of a mechanical resonator can be several orders of magnitude higher than what can be achieved using electrical components [35-37]. This further improves the frequency selectivity and harmonic suppression capability of the electromechanical circuit.

Since piezoelectricity is not the only transduction mechanism to convert energy between the electrical and mechanical domain, alternative transduction mechanisms such as electrodynamic, electrostatic, and magnetostrictive might offer benefits that can offset the limitations of PTs. Because electrodynamic transduction has been investigated and used for almost two centuries, and it is still a predominant transduction mechanism in the modern energy conversion applications, it makes natural sense to investigate electrodynamic transduction for electromechanical energy transfer.

#### **1.2.4. Potential Advantages of Electrodynamic Transformers**

From the discussion in [Section 1.2.3](#), the amount of energy being stored and transferred in a mechanical resonator is limited by the yield strength of the compliance material. In a PT, the yield strength of the piezoelectric material limits the maximum amount of energy stored in the mechanical resonator of the PTs. This places a limit on the maximum mechanical energy transferred per cycle of vibration, which corresponds to the power capacity [38]. Unfortunately, the yield strength of the best performing piezoelectric materials are not exceptionally high. Moreover, the requirement to survive frequent deformation places additional challenge to the material selection. Fatigue [39-41], depolarization [42-44], and even catastrophic failure [45, 46] are common problems

when driving piezoelectric materials to high strain levels. Also, the deformation induced thermoelastic loss in the piezoelectric material increases the temperature in the material, especially at elevated power densities. The increased temperature can degrade the performance of the piezoelectric material and cause unwanted deformation (called thermoelastic displacement [47, 48]). As a consequence, to ensure reliable long-term operation, piezoelectric materials are typically operated substantially below their ultimate limits.

In comparison, the proposed ET architectures, like the example shown in [Figure 1-3](#), may use a separate compliance element that possesses exceptionally high yield strength and good long-term reliability. This is contrast to the piezoelectric transduction in a PT, where the energy conversion mechanism and material are inseparable. In an ET, the energy conversion elements—the conductor and the magnetic field source—are generally subjected to negligible stress, strain, or friction. This greatly improves the overall reliability of the system and reduces difficulty in material selection. The power density and efficiency could potentially be increased by using stronger, lower-loss compliance materials. Admittedly, the use of separate compliance element would increase the overall physical volume of the device, which tends to decrease the overall power density. However, through careful design and optimization, the compliance element could have very small physical size. If it is desired, as will be discussed in [Chapter 3](#) and demonstrated in [Chapters 5](#) and [6](#), ETs can also have an “integrated” compliance element as in PT, where the conductor is used as the compliance element.

As noted in [Section 1.2.3](#), the primary and secondary side of a PT share common ground electrode [49]. This enables transmission of common mode noise from the

primary to the secondary side, which reduces the noise isolation capability of the PTs, and to some extent, offsets the benefit of the low EMI. The noise from the primary side (e.g. switching noise) could potentially transmit to the secondary side through the common ground, which may cause interference on the load. Similar to the conventional EMT, the terminals of the input and output coils in an ET would not generally be electrically connected. This provides reliable galvanic isolation, which is desirable in many applications.

One of the major concerns of many piezoelectric transducers is the lead-containing material. Due to the attractive piezoelectric property, PZT (lead zirconate titanate) is the most widely used piezoelectric material in PTs. Although lead-free piezoelectric materials are also available (such as PVDF, NaKNb, BiFeO<sub>3</sub>, etc.), their properties are still less competitive than PZT [50]. On the other hand, almost all common magnetic materials that would be used in electrodynamic transducers are lead-free, and are friendlier to the environment. Furthermore, the aging effect of the magnetic materials is in general less pronounced than that of the piezoelectric materials [41, 51-53]. The long term reliability of the electrodynamic transducers has been proved for over a century.

### **1.3. Historical Review**

The idea of using electromechanical coupling to transfer electrical energy is not new. Back in the 19<sup>th</sup> century, when stationary power conversion technology was not available, the electric power industry relied on such mechanisms to perform various power conversions [54-59]. For example, different types of motors and generators were cascaded to convert ac and dc power from one form to another. For instance, when the output of an ac motor was mechanically connected to a dc generator, the input ac

electrical power was first converted to mechanical rotation by the ac motor, and then to dc electric power by the dc generator, forming an ac/dc converter. Such a system was called a "motor-generator." A revised form of the motor-generators was the "rotary converter," where the motor and the generator shared the same armature and field coils. A picture of an ac/dc rotary converter is shown in [Figure 1-8](#). This converter, installed as a part of railway electrification in 1895, was used to convert 13,200 V three-phase ac voltage to 675 Vdc.

Motor-generators and rotary converters were also used to step up or step down dc voltages, rectify ac voltage to dc, invert dc voltage to ac, and change the frequency or number of phases of an ac voltage. Although rotational devices could also perform ac voltage step-up or step-down, stationary EMTs, which existed before the rotary converters [60], were used instead for their higher efficiency and simpler construction.

Today, advancements in solid-state power electronic devices typically provide more compact solutions for most modern power converter applications. However, owing to their extremely high reliability, low output impedance, great isolation and low input output harmonic distortion [61], rotary converters are still being used today in high-power applications, such as electric railway traction power systems [24, 62]. They are also still found in specialized power networks, such as large ship power systems. With ongoing progress in contactless (levitating) bearings and high-temperature superconducting technologies [63-65], rotary converters may even experience a resurgence in the near future.

Although the intended functionality of these motor-generators and rotary converters are different from that of the proposed ET, they are the closest "ancestors" of

the proposed technology. They all share the common concept of using electrodynamically coupled mechanical motion to transfer electrical energy. One major difference for the proposed ET is the use of oscillatory motion, as opposed to rotational motion.

As the system scales down, the tribological scaling of a rotating pivot becomes extremely unfavorable [66, 67]. Smaller rotating machines are subject to much higher friction, and therefore lower efficiency and shorter life time. Due to restrictions on the cost, space, and available technology, contactless bearing systems would be difficult to implement in most small scale systems such as portable electronics, sensors, etc. This limits the miniaturization of the rotary converters.

Unlike continuous rotations, mechanical oscillations can achieve very low mechanical loss even at micro scales. The quality factor is often used to characterize the loss property of a mechanical oscillator. Quality factor is proportional to the ratio of the energy stored in the oscillator to the energy dissipated per cycle of oscillation:

$$Q = 2\pi \times \frac{\textit{Energy stored}}{\textit{Energy dissipated per cycle}}. \quad (1-3)$$

The scaling of the quality factor makes microscale implementation of mechanical oscillators not only feasible but also attractive. Quality factors of 1,000 to 50,000 have been reported for devices with feature sizes of micrometers [68-71]. On the other hand, the quality factor of electrical oscillators are usually <100. This spurs the development small scale application area, where mechanical vibration is used to transfer electrical energy.

#### **1.4. Research Objectives and Overview**

The goal of the dissertation is to explore the characteristics of the ET and to investigate its potential applications in candidate power electronic systems. Because this is preliminary research of an under-investigated topic, the research constitutes a feasibility study that is exploratory in nature. Consequently, the work is presented with a majority of theoretical development, followed by experimental demonstrations to validate the theory and concepts. In order to set this research in the context of the state-of-the-art, side-by-side comparison among the EMT, PT and ET are performed through theoretical analysis and literature review. Eventually, conclusions are made on the merit of the ET concept and future works are suggested for performance improvement and application areas.

To achieve these objectives, a generalized energy-domain-based, lumped element modeling approach is first developed to model and analyze the ET. This modeling approach also enables comparison of the three types of transformers on a common theoretical framework, i.e. equivalent circuit models. Side-by-side comparisons are performed on the efficiency, power density, scalability and other practical considerations.

The experimental work is composed of four parts. The first part is construction and demonstration of a macroscale ET prototype. The second part is experimental model validation using the macroscale prototype. The third part is a demonstration of a microscale ET prototype. In the fourth part, an application example of the ET is presented in a resonant converter using the microfabricated prototype.

The dissertation is presented with the following structure:

[Chapter 1](#) provides the general background of the topic (motivation of the work and literature review) and presents the objectives of the research.

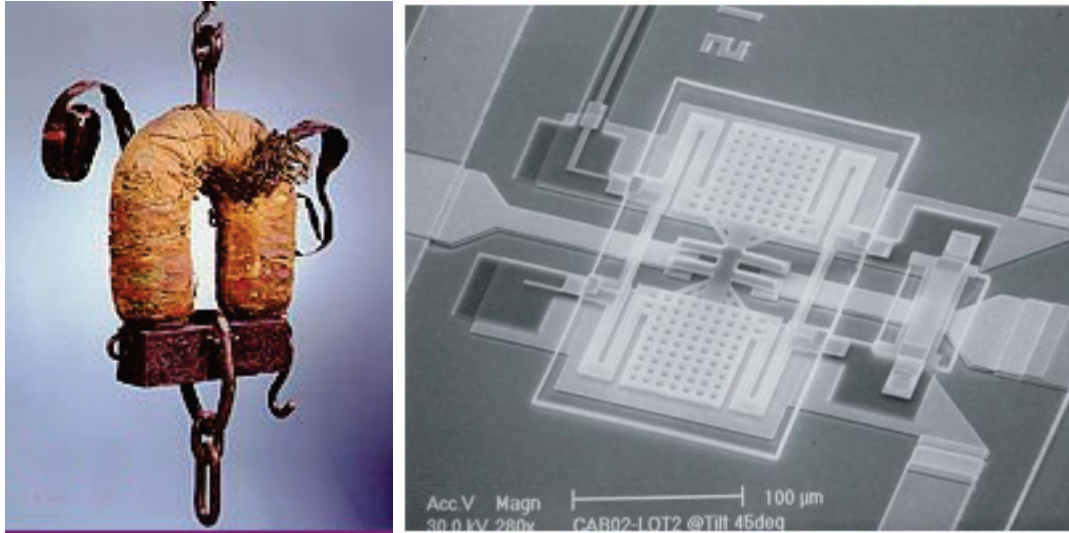
[Chapter 2](#) introduces the theory of transducer modeling using lumped element models.

[Chapter 3](#) explores the operation, scaling, and performance bounds of the ET using the modeling technique introduced in [Chapter 2](#), and compares the predicted performance of the ET with the EMT and PT.

[Chapter 4](#) presents a macroscale experimental prototype and experimentally validates the ET model.

[Chapter 5](#) presents the design, fabrication and characterization of a microfabricated ET, and demonstrates an application of the ET in a resonant dc/ac inverter.

[Chapter 6](#) concludes the dissertation with a summary of the major results and contributions and a suggestion of future works.



A

B

Figure 1-1. Pictures of switches. A) a relay switch by Joseph Henry (1797-1878). B) A MEMS switch by Rockwell Scientific. [72]. (Reprinted from "RF MEMS switches: status of the technology" in *TRANSDUCERS, 12th International Conference on Solid-State Sensors, Actuators and Microsystems 2003*, pp. 1726-1729, by G. M. Rebeiz, Copyright 2003, with permission from IEEE.)

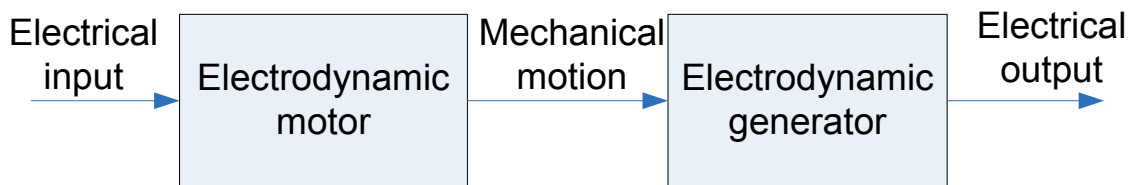


Figure 1-2. Block diagram of an electrodynamic transformer.

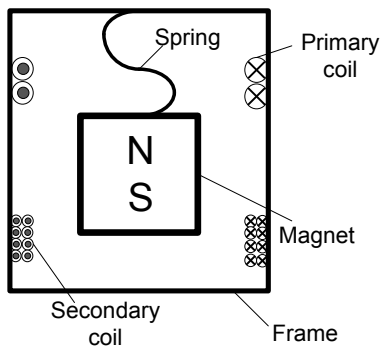


Figure 1-3. Schematic illustration of an example electrodynamic transformer structures.

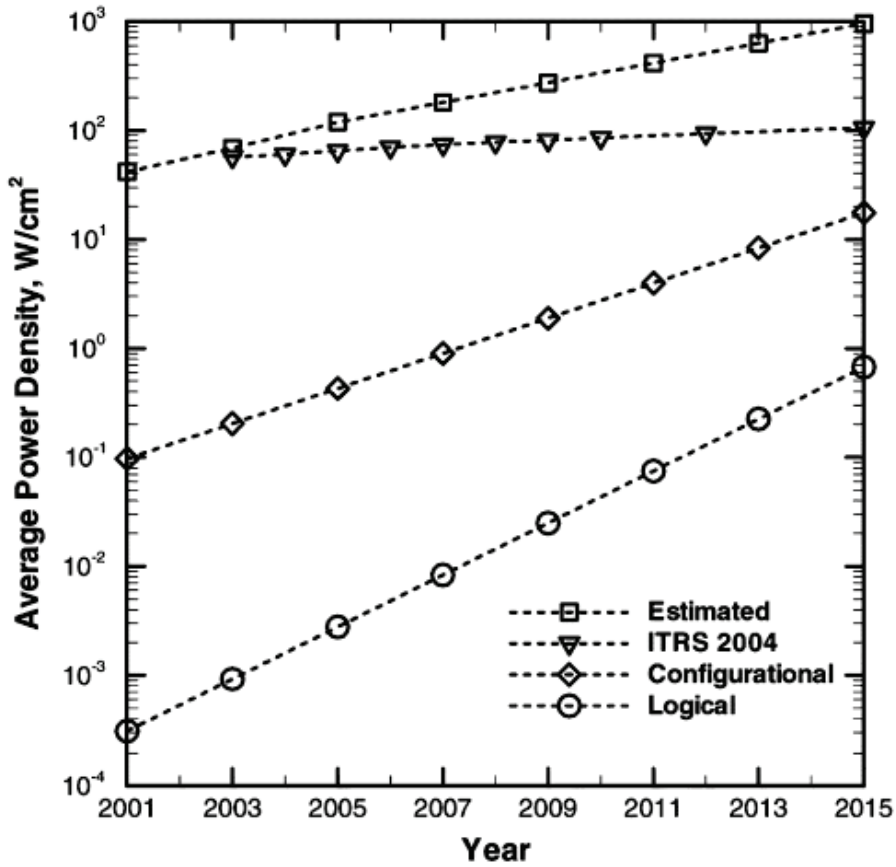


Figure 1-4. Microprocessor power density increase over time. (Reprinted from, "Towards a Thermal Moore's Law" in *Advanced Packaging, IEEE Transactions on*, vol. 30, pp. 462-474, by S. Krishnan, S. V. Garimella, G. M. Chrysler, and R. V. Mahajan, Copyright 2007, with permission from IEEE.)

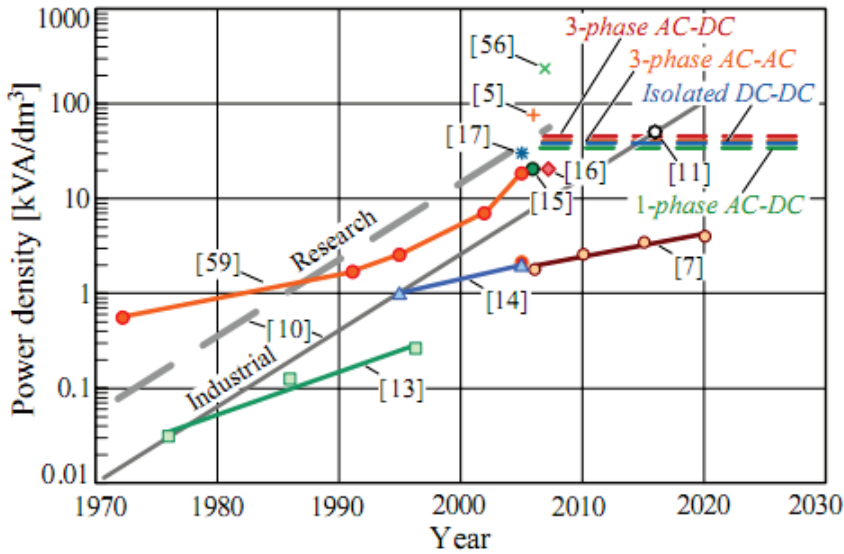


Figure 1-5. Progress of power converter power density. (Reprinted from "PWM Converter Power Density Barriers," in *Power Conversion Conference - Nagoya, 2007. PCC '07*, pp. P-9-P-29, by J. W. Kolar, U. Drofenik, J. Biela, M. L. Heldwein, H. Ertl, T. Friedli, and S. D. Round, Copyright 2007, with permission from IEEE.)

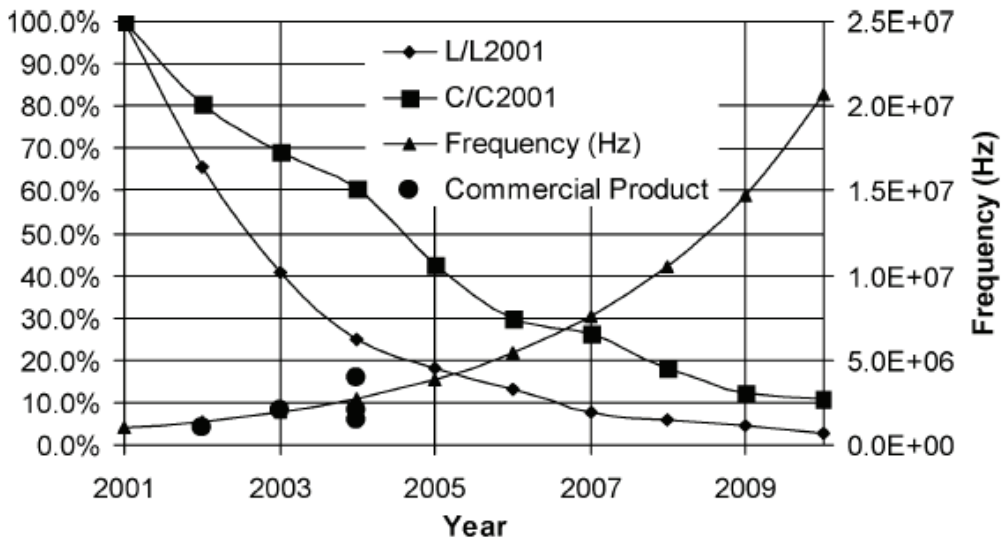


Figure 1-6. Trends of passive device size (inductor/capacitor value normalized to 2001 values) and operating frequency versus time for single-phase buck converters [73]. (Reprinted from "Magnetics on silicon: an enabling technology for power supply on chip" in *IEEE Transactions on Power Electronics*, vol. 20, pp. 585–592, by S. C. O. Mathuna, T. O'Donnell, W. Ningning, and K. Rinne, Copyright 2005, with permission from IEEE.)

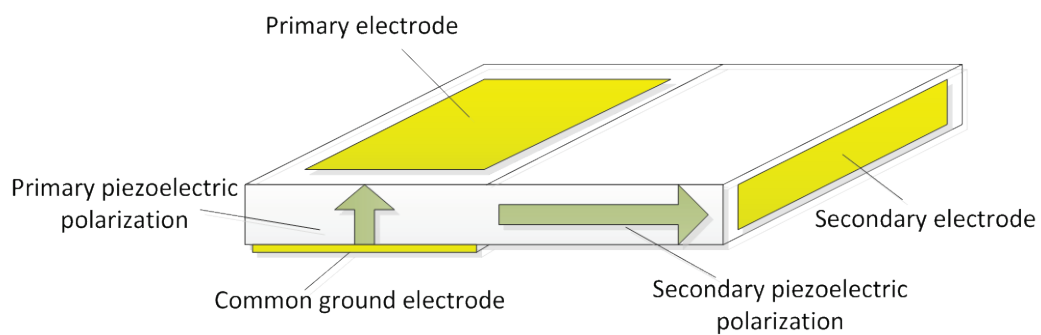


Figure 1-7. Schematic of a Rosen type PT.

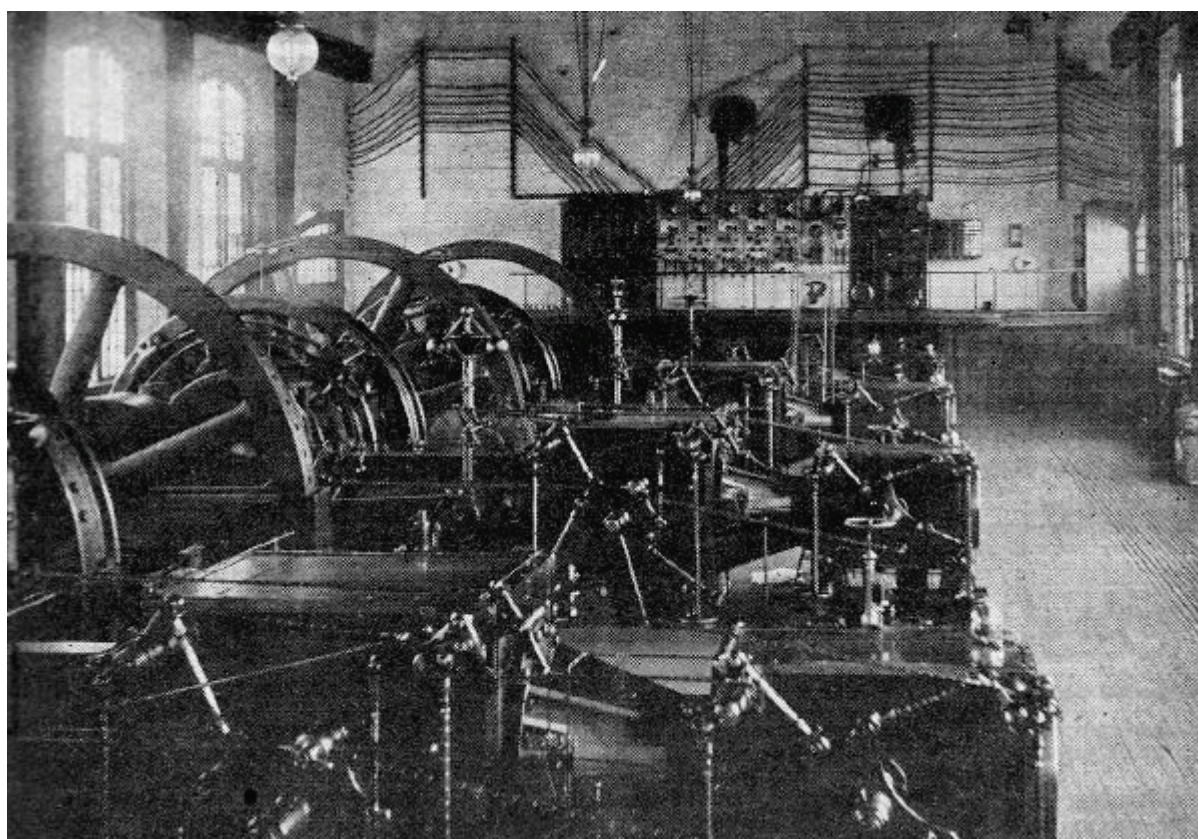


Figure 1-8. AC-DC rotary converters in the powerhouse for the Baltimore Belt Line of the Baltimore and Ohio Railroad, part of the first mainline railroad electrification in 1895 (public domain image at [http://en.wikipedia.org/wiki/Rotary\\_converter](http://en.wikipedia.org/wiki/Rotary_converter)).

## CHAPTER 2 THEORETICAL BACKGROUND

An electrodynamic transformer is a complicated device that consists of electrical, mechanical and magnetic subsystems. In the major energy transfer path, the electrical energy in the primary coil is converted to mechanical energy, and then back to electrical energy in the secondary coil, where both energy conversions are via electrodynamic transduction. There is also a “parasitic” energy transfer path that consists of the air-core electromagnetic transformer, where the magnetic domain acts as the intermediate domain, and electromagnetic transduction is in effect. Appropriate reduced-order models are desired to enable design and optimization of the overall performance.

The goal of this chapter is to lay out a fundamental background for the modeling approaches used. First, a general overview of transducer modeling will be presented. Next, the lumped element modeling (LEM) technique will be introduced. The LEM technique will then be applied to construct modeling frameworks for the energy domains involved in the ET. Specifically, basic concepts and LEM building blocks in the mechanical, electrical and magnetic domains will be introduced, and the modeling of the inter-domain interactions (electromagnetic and electrodynamic transductions) will be explained. Finally, two example LEM equivalent circuit models will be presented for physical transducers relevant to the full ET modeling.

### **2.1. Transducer Modeling Overview**

A transducer is a device that converts, or “transduces,” one type of energy into another. For example, an electromechanical transducer converts energy between electrical and mechanical domains. Although all transducers convert energy from one domain to another, there are two general categories of transducers that differ

significantly in terms of performance evaluation. In the first category, the merit of the transducers is mainly evaluated from the energy or power perspective. For example, electric power generators are mainly evaluated by how much power can be generated, how efficient is the energy conversion, etc. The second category of transducers emphasizes more on the signal representation performance. As an example, a microphone is evaluated by how accurately the output signal can represent the input quantity, the dynamic range of the measured signal, etc. In this dissertation, the term "transducer" is exclusively referred to the first category.

All the transducers discussed in this chapter are assumed to be passive, linear, and time-invariant (LTI) systems. Passive means that the transducer itself does not produce any power, and that all the power flow is sourced from the input of the transducer. Linear means that the transducer satisfies properties of superposition and homogeneity. Specifically, if the output variable ( $y$ ) of a transducer is related to the input ( $x$ ) as

$$y = f(x), \tag{2-1}$$

the function  $f(x)$  must meet the following conditions:

$$\begin{aligned} f(x_1 + x_2) &= f(x_1) + f(x_2) \\ f(\alpha x) &= \alpha f(x) \end{aligned} \tag{2-2}$$

Time-invariant means that the transducer parameters do not change with time.

For all real physical phenomena, the system energy is distributed in space and time. A precise model of a transducer would then consist of an infinite number of continuously distributed elements. If all these are to be included in an equivalent circuit model, the model will consist of infinite number elements. Analytical models that provide space-continuous solutions are not always available for complicated transducers. On

the other hand, numerical models such as finite element model (FEM) that use a large amount of discrete elements require large computations and provide less physical insight for analysis and design of transducers. In this work, the lumped element modeling (LEM) technique will be used as the primary modeling tool. As will be explained in [Section 2.2](#), LEM is a simple and effective tool that provides physical insight and adequate accuracy engineering analysis for design purposes.

LEM enables equivalent circuit representations of transducers involving multiple energy domains. In order to use electrical circuit elements to represent elements in non-electrical domains, an analogy system between other energy domains and electrical domain needs to be established. Therefore, conjugate power variables and elements in each energy domains are related, and the physical interactions between two domains are modeled using appropriate circuit representations (as described in [Sections 2.3](#) and [2.4](#)).

## **2.2. Lumped Element Modeling Fundamentals**

Lumped element modeling (LEM) is a simple but effective tool for modeling systems involving multiple energy domains [5, 6, 74]. In an LEM, the complexity of a multi-energy-domain physical system is reduced by breaking down the system into discrete elements based on the system's interaction with energy. As long as the greatest dimension of the discrete element is much smaller than the characteristic length scale of the physical phenomena (e.g. wavelength, diffusion length scale), the spatial variations of the quantities of interest can be decoupled from the temporal variations. As a result, the dynamic behavior of the element can be described with an ordinary differential equation where time is the only independent variable. In this case,

the distributed energy storage/dissipation mechanism is “lumped” into a single point in the space, and therefore represented with a single circuit element.

In a LEM, energy flows in and out of the lumped elements. It can be found that for every energy domain, the power transfer can be expressed as the product of two variables. One of these variables quantifies a “flow” through the element, while the other one quantifies an “effort” acting across the element. The former is defined as the “flow variable” ( $\tilde{f}$ ), while the latter is defined as the “effort variable” ( $\tilde{e}$ ). Together, they form the “conjugate power variables” of an energy domain. For example, in the electrical domain, power can be expressed as the product of current and voltage, where the current is a measurement of the charge flow, and the voltage is the “effort” that acts across the element. Therefore, current and voltage are the electrical conjugate power variables, and the current is the flow variable, while the voltage is the effort variable.

Elements in a LEM interact with each other or the outside world through “ports”. A port consists of two terminals that satisfy the port condition: the flow variable into one terminal must equal to the flow variable out from the other terminal [75]. The effort variable of one terminal may be higher than that of the other. When the flow is directed from the high effort terminal to the low effort terminal, power flows into the element; when the flow is directed from the low effort terminal to the high effort terminal, power flows out of the element; when the effort of the two terminals are the same, there is no net power flow at the port. In most conventions, a positive flow direction is defined such that the power flows into the element, i.e. a positive flow is directed from the high effort terminal to the low effort terminal of a port.

In the transducers involved in this work, the lumped models employ one-port and two-port elements, which are summarized in [Table 2-1](#). Illustrations of generalized one-port and two-port elements are shown in [Figure 2-1](#), One-port elements are used to model elements inside a specific energy domain, while two-port elements are used to interface two energy domains.

One-port elements can be categorized into three types depending how flow and effort variables interact with each other. The three types are: generalized inertance, generalized compliance and generalized resistance. In a generalized inertance, the effort variable is proportional to the time derivative of the flow variable:

$$\tilde{e} \propto \frac{d\tilde{f}}{dt}. \quad (2-3)$$

In a generalized compliance, the effort variable is proportional the time integral of the flow variable:

$$\tilde{e} \propto \int \tilde{f} dt. \quad (2-4)$$

In a generalized resistor, the effort variable is directly proportional to the flow variable:

$$\tilde{e} \propto \tilde{f}. \quad (2-5)$$

There are two types of two-port elements that depict different physical interactions between energy domains. They are the transformer and the gyrator, as shown in [Figure 2-2](#). In a transformer, the effort variable across one port is proportional to that across the other port; the flow variable through one port is also proportional that of the other port:

$$\tilde{e}_2 = T\tilde{e}_1, \quad (2-6)$$

and

$$\tilde{f}_2 = -\frac{1}{T} \tilde{f}_1. \quad (2-7)$$

where  $T$  is defined as the transformer ratio. In a gyrator, the effort variable across on port is proportional to the flow variable through the other port.

$$\tilde{e}_1 = G\tilde{f}_2, \quad (2-8)$$

and

$$\tilde{e}_2 = -G\tilde{f}_1. \quad (2-9)$$

where  $G$  is defined as the gyration resistance. It is termed a “resistance” because it represents the ratio of an effort and a flow. Note that in both (2-7) and (2-9), the negative sign means that the power flows into port 1 and out of port 2.

With all the generalized elements defined, the LEM can be represented as an equivalent circuit. In the equivalent circuit, the flow variable is represented by electrical current, and the effort variable is represented by the electrical voltage. The generalized inertance, compliance and resistor are equivalent to the electrical inductor, capacitor and resistor, respectively. The proportionality constant of their constitutive equations are represented by the inductance, reciprocal of capacitance and resistance, respectively.

The input excitation source of the transducer can also be modeled using generalized one-port elements: flow source and effort source. A flow source generates constant flow, while an effort source generates a constant effort. “Ideal” sources can be represented with an ideal electrical current source and voltage source, respectively.

The circuit representations of all the elements discussed above along with their constitutive equations are listed in [Table 2-1](#). With the equivalent circuit representation, the LEM can be analyzed with standard circuit analysis techniques, such as mesh and node methods, Thévenin and Norton equivalent circuits, and two-port network analysis

theories. Also, system simulation can be easily implemented with circuit simulation tools.

### 2.3. Lumped Element Model within Different Energy Domains

This section extends the generalized LEM modeling framework introduced in the last section to specific energy domains. Implementations of LEM in mechanical, electrical and magnetic domains will be presented. The descriptions in the mechanical and electrical domains will be brief compared to the magnetic domain, because the lumped element modeling technique in the mechanical and electrical domains is much better known than in the magnetic domain. The LEM representations of the mechanical, electrical and magnetic domain conjugate variables and fundamental elements are summarized in [Table 2-2](#) in advance.

#### 2.3.1. Mechanical Domain

In the mechanical domain with rectilinear motion, force ( $f$ ) and velocity ( $u$ ) are the effort and flow variables, respectively [5]. Three fundamental elements in the mechanical domain are the mass, spring, and damper.

For a mass ( $m$ ), the force is the proportional to the time derivative of the velocity:

$$f = m \frac{du}{dt}. \quad (2-10)$$

The constitutive equation (2-10) agrees with that of the generalized inertance as in (2-3). Therefore, a mass is a generalized inertance. Equation (2-10) indicates that the velocity in mass cannot change abruptly given a finite force, or that a mass has the tendency to maintain its velocity. Therefore, a mass is a kinetic energy storage. Similarly, generalized inertance in all energy domains has the tendency to maintain its

flow. Therefore, generalized inertances are all kinetic energy storage from a general aspect.

For a spring, the force is proportional to the time integral of the velocity (the displacement):

$$f = k \int u dt, \quad (2-11)$$

where  $k$  is the spring constant of the spring. By comparing (2-11) with (2-4), it can be concluded that a spring is a generalized compliance. Equation (2-11) indicates that the force on a spring cannot change abruptly with a finite velocity, or that the spring has a tendency to maintain a force. Therefore, a spring is a potential energy storage. The same applies to generalized compliances in other energy domains, where the tendency to maintain an effort is shown. Therefore, generalized compliances are all potential energy storage in a broader sense.

For a viscous damper, the force is proportional to the velocity:

$$f = bu, \quad (2-12)$$

where  $b$  is the damping coefficient of the damper. Thus, a viscous damper is a generalized resistor according to (2-5). As a damper has no tendency to maintain a force or a velocity, any energy applied to a damper is dissipated immediately.

Therefore, a damper is an energy dissipater. Similar conclusion also applies to generalized resistors in other energy domains. Generalized resistors are used to model energy dissipaters in all other energy domains.

### **2.3.2. Electrical Domain**

The electrical domain conjugate power variables are the voltage ( $u$ ) and the current ( $i$ ). As has been explained in [Section 2.2](#), voltage is the effort variable and

current the flow variable. The inductor, capacitor, and resistor are the basic elements in the electrical domain.

For an inductor, the voltage is proportional to the time derivative of the current:

$$v = L \frac{di}{dt}, \quad (2-13)$$

where  $L$  is the inductance of the inductor. This constitutive equation indicates that an inductor is a generalized inertance. It is a kinetic energy storage in the electrical domain, because it tends to maintain a current flow.

For a capacitor, the voltage is proportional to the time integral of the current (the charge):

$$v = \frac{1}{C} \int i dt, \quad (2-14)$$

where  $C$  is the capacitance of the capacitor. This equation indicates that a capacitor is a generalized compliance. It is a potential energy storage that maintains the voltage across its terminals.

A resistor behaves similarly to a mechanical damper:

$$v = Ri, \quad (2-15)$$

where  $R$  is the resistance. A resistor is apparently a generalized resistor in LEM and an energy dissipater in the electrical domain.

### 2.3.3. Magnetic Domain

The magnetic domain constitutive relations can be found by using the electromagnetic duality. According to electromagnetic duality, electrical field ( $E$ ) is related to the magnetic field ( $H$ ), and electrical charge density or flux density ( $D$ ) is related to the magnetic flux density ( $B$ ). The effort variable in the electrical domain is

voltage, which is the negative line integral of the electric field. By the duality analogy, one can deduce that in the magnetic domain, the effort variable should be the line integral of the magnetic field ( $\vec{H}$ ),

$$\text{Magnetic effort} = -\int_l \vec{H} \cdot d\vec{l} = -MMF, \quad (2-16)$$

where  $MMF$  is the magnetomotive force. Therefore, the magnetic effort variable is defined as the negative  $MMF$ . Now consider Ampère's Law, which relates the electrical current with the magnetic field:

$$\oint_{\partial s} \vec{H} \cdot d\vec{l} = \iint_s \left( \vec{J}_f + \frac{\partial \vec{D}}{\partial t} \right) \cdot d\vec{A} = i \quad (2-17)$$

where  $\vec{J}_f$  is the free current density, and  $\frac{\partial \vec{D}}{\partial t}$  is the displacement current density.

Equation (2-17) states that the electrical flow variable (current) enclosed by a contour is equal to the line integral of the magnetic field along the contour. Analogously, Faraday's Law states that the line integral of the electric field along a contour is equal to the negative time rate change of magnetic flux ( $-\dot{\phi}$ ) within the area surrounded by the contour ( $\vec{A}$ )

$$\oint_{\partial s} \vec{E} \cdot d\vec{l} = -\iint_s \frac{\partial \vec{B}}{\partial t} \cdot d\vec{A} = -\dot{\phi} \quad (2-18)$$

where  $\vec{B}$  is the magnetic flux density inside the contour. Therefore, by comparing (2-18) and (2-17), and using the electromagnetic duality, the flow variable in the magnetic domain is observed to be the negative time rate change of magnetic flux ( $-\dot{\phi}$ ). Since both the effort variable and the flow variable in the magnetic domain have a negative sign, it is more convenient and reasonable to ignore both negative signs, so that the

effort variable is the MMF, and the flow variable is the time rate change of magnetic flux. The only effect of ignoring the negative sign is the interfacing between the electrical and magnetic domains, which will be covered in [Section 2.4](#). Note that the effort variable in the magnetic domain has a unit of Ampère, and the flow variable has a unit of Volt. This is consistent with the electromagnetic duality theory.

With the effort and flow variables established, the magnetic inertance, compliance and resistance can be defined using their constitutive relations. The inertance is the ratio between the effort variable and the time derivative of the flow variable, which in the magnetic domain is given by

$$\text{Magnetic inertance} = \frac{MMF}{\dot{\phi}} \quad (2-19)$$

The magnetic inertance is the tendency for a magnetic structure to maintain the time rate change of the flux, when it is subjected to a finite *MMF*. To better understand this, assuming that the *MMF* is generated by *N*-turn current carrying coil, the *MMF* is given by

$$MMF = Ni, \quad (2-20)$$

and the voltage induced on the coil is given by

$$v = N\dot{\phi} \quad (2-21)$$

Substituting (2-20) and (2-21) into (2-19),,

$$\text{Magnetic inertance} = N^2 \frac{i}{\dot{v}} \quad (2-22)$$

Note, the ratio  $\frac{i}{\dot{v}}$  is the equivalent electrical capacitance of the coil. Therefore it is concluded that the magnetic inertance is equivalent to the electrical compliance (capacitance) times a "conversion factor" ( $N^2$ ).

These results initially seem to be counter-intuitive. However, since the electrical effort variable ( $v$ ) is proportional to the magnetic flow variable ( $\dot{\phi}$ ) according to Faraday's law, and the magnetic effort variable ( $MMF$ ) is proportional to the electrical flow variable ( $i$ ) according to (2-20), it is inevitable that an electrical compliance appears as a magnetic inertance, and vice versa.

As stated in [Section 2.3.3](#), a generalized inertance is a kinetic energy storage. However, since the magnetic inertance appears as electrical compliance, it is a potential energy storage from the electrical domain's view point. In fact, as far as the author's knowledge, the so-called "magnetic inertance" can only be implemented in the electrical domain via electric field energy storage.

On the other hand, the generalized compliance is the ratio between the time integral of the flow variable and the effort variable, which in the magnetic domain is given by

$$\text{Magnetic compliance} = \frac{\int \dot{\phi} dt}{MMF} = \frac{\phi}{MMF} = \frac{1}{\mathfrak{R}} = \Lambda \quad (2-23)$$

where  $\mathfrak{R}$  is the reluctance of the magnetic flux path (in A/Wb), and  $\Lambda$  is the permeance of the magnetic flux path (in Wb/A). Again, suppose that the MMF is generated by an  $N$ -turn current carrying coil. Substituting (2-20) and (2-21) into (2-23),

$$\text{Magnetic compliance} = \frac{\int \dot{\phi} dt}{MMF} = \frac{\int \frac{v}{N} dt}{Ni} = \frac{1}{N^2} \frac{\int v dt}{i} \quad (2-24)$$

As has been predicted, (2-24) states that the magnetic compliance is equivalent to the electrical inertance (inductance) divided by  $N^2$ . Again, since a generalized compliance is a potential energy storage, and the magnetic compliance appears as an inertance in the electrical domain, it can be concluded that magnetic potential energy storage appears as kinetic energy storage in the electrical domain.

From the above analysis, it is concluded that the magnetic inertance and electrical compliance are defining the same physical phenomena (that occurs in the electrical domain) from different perspectives. The same is true for the magnetic compliance and the electrical inertance, where the physical phenomena occurs in the magnetic domain. When modeling a system, only one representation can be counted from each pair. In the magnetic compliance/electrical inertance pair, the energy is physically stored in the magnetic domain as a magnetic field instead of the electrical domain; therefore magnetic compliance is a more reasonable definition from physical standpoint. Similarly, in the magnetic inertance/electrical compliance pair, the energy is stored in an electrical field, so electrical compliance is more reasonable. However, since the electrical inertance has been used conventionally instead of magnetic compliance, its continued usage should not be unjustified. After all, the choice of definition does not affect the analysis result, just the physical insight. An example will be given in [Section 2.5.1](#), where the modeling of an air-core transformer is performed in both magnetic and electric domains, yielding equivalent results.

For the magnetic resistance, since there is no “free magnetic current” due to the lack of magnetic monopole, nothing physically exists in the magnetic domain where the effort is proportional to the flow. However, due to the electromagnetic duality, electrical

conductance (reciprocal of resistance) appears as magnetic resistance. Another use of the magnetic resistance is to model the energy dissipaters in the magnetic domain. The loss mechanisms in the magnetic domain originate from a variety of nonlinear behaviors such as hysteresis, saturation, etc. These behaviors are much more complicated than what a generalized resistor can describe. The use of magnetic resistance can only model the energy loss in the magnetic energy dissipaters, but not the constitutive relations. In this case, the closest analogy to the magnetic resistance is a conceptualized resistance in the electrical domain that approximates the dielectric loss that is caused by certain nonlinear behaviors in the dielectric materials. Such an electrical resistance is often referred to as the equivalent series resistance (ESR) of a dielectric material.

#### **2.4. Inter-domain Interactions**

The previous section generalized the representation of basic elements in each of the three energy domains (mechanical, electrical, and magnetic) in LEM. In a transducer, two or more energy domains are related through energy conversion (transduction) mechanisms. This section introduces the interactions between the electrical, magnetic and mechanical domains. Energy is converted between electrical and magnetic domains through electromagnetic transduction. This is the primary mechanism that supports the operation of EMTs. Energy conversion between electrical and mechanical domains is electromechanical transduction. There are numerous ways to implement electromechanical transduction. In the PT, the electromechanical energy conversion is implemented using piezoelectric transduction. In the ET, it is implemented using electrodynamic transduction. In the remainder of this subsection, electromagnetic

and electrodynamic transductions will be introduced. Due to its importance in ET modeling, more emphasis is placed on electrodynamic transduction.

#### 2.4.1. Electromagnetic Transduction

Electromagnetic transduction occurs wherever a time-varying electric field or magnetic field exists. Instead of dealing with a general case where a time-varying electric field induces a magnetic field or vice versa, this subsection only treats a specific case that is most relevant to the context of the work: a current carrying multi-turn filamentary solenoid and its associated magnetic field, as shown in [Figure 2-3](#).

In this specific case, a current  $i$  flows in the  $N$ -turn coil, generating a magnetic field  $\vec{H}$  that surrounds the conductors. For any magnetic flux path that encloses all the coil turns,

$$Ni = \oint_L \vec{H} \cdot d\vec{l} = MMF \quad (2-25)$$

When the current is time-varying, the magnetic flux in the coil is also time-varying, inducing an EMF on the coil:

$$v = -N\dot{\phi} \quad (2-26)$$

Since this EMF (often called a “back EMF”) is operating against the current flow, the right hand side of (2-26) has a negative sign. As explained in [Figure 2.3\(a\)](#),  $v$  and  $i$  are the effort and flow variables in the electrical domain, while  $MMF$  and  $\dot{\phi}$  are the effort and flow variables in the magnetic domain. It is noted in both (2-25) and (2-26) that the proportionality constant  $N$  links the two domains. These two governing equations agree with to the general governing equations of a gyrator as in (2-8). Therefore,

electromagnetic transduction can be modeled in LEM with a gyrator with gyration resistance equal to the number of coil turns as shown in [Figure 2-3\(b\)](#).

### 2.4.2. Electrodynamic Transduction

In electrodynamic transduction, electrical to mechanical transduction is governed by the Lorentz force. Suppose that an electric current  $i$  flows through a unit segment of a filamentary conductor (with length  $d\vec{l}$ , and cross section area  $A = 0$ ) that is subjected to a magnetic field with flux density  $\vec{B}$ , as shown in [Figure 2-4](#). The moving electrons in the conductor segment experience a magnetic force

$$d\vec{f} = i\vec{B} \times d\vec{l}. \quad (2-27)$$

If the conductor segment moves at a velocity of  $\vec{u}$ , the mechanical to electrical transduction occurs at the same time. This transduction is governed by the “motional” part of Faraday’s Law of Induction (as explained in [Appendix A](#)),

$$dv = -\vec{u} \cdot \vec{B} \times d\vec{l}, \quad (2-28)$$

where  $dv$  is the differential voltage generated on the segment of conductor.

In order to represent the transducer in an equivalent circuit, all the conjugate power variables need to be scalars, rather than vectors. Equations (2-27) and (2-28) are rewritten as

$$f = i \int_{l_c} \hat{f} \cdot \vec{B} \times d\vec{l}, \quad (2-29)$$

and

$$v = -u \int_{l_c} \hat{u} \cdot \vec{B} \times d\vec{l}, \quad (2-30)$$

where  $f$  and  $u$  are the magnitudes of the force and the velocity, respectively;  $\hat{f} = \frac{\vec{f}}{f}$  and

$\hat{u} = \frac{\vec{u}}{u}$  are the unit vector directions of the force and velocity, respectively;  $l_c$  is the total

length of the conductor. Note that in single-degree-of-freedom systems that are concerned in this study, the directions of the force and the velocity are the same, or

$$\hat{f} = \hat{u}. \quad (2-31)$$

Therefore (2-29) can be rewritten as

$$f = i \int_{l_c} \hat{u} \cdot \vec{B} \times d\vec{l}. \quad (2-32)$$

Note that in (2-30) and (2-32) the effort variable in the electrical domain is proportional to the flow variable in the mechanical domain, and the effort variable in the mechanical domain is proportional to the flow variable in the mechanical domain. Therefore, electrodynamic transduction can also be modeled with a gyrator, where the gyration resistance is

$$K = \oint_{l_c} \hat{u} \cdot \vec{B} \times d\vec{l}. \quad (2-33)$$

$K$  is defined as the “transduction coefficient”, this definition is more general than the one seen in most literatures [74]:

$$K = Bl_c, \quad (2-34)$$

which is only true when the velocity, flux density and conductor length are everywhere perpendicular to each other.

For example, consider an arbitrary coil arrangement in a non-uniform magnetic field, as depicted in [Figure 2-5](#). At a given position along the conductor, if the angle

between  $\vec{B}$  and  $d\vec{l}$  is  $\alpha$ , and the angle between  $\vec{B} \times d\vec{l}$  (the direction of the plane containing  $\vec{B}$  and  $d\vec{l}$ ) and  $\hat{u}$  is  $\beta$ , the transduction coefficient is given by

$$K = \oint_{l_c} \hat{u} \cdot \vec{B} \times d\vec{l} = \oint_{l_c} B \sin \alpha \cos \beta dl, \quad (2-35)$$

where  $B$  is the magnitude of the flux density at the position  $l$ . Note that  $B$ ,  $\alpha$  and  $\beta$  are all functions of  $l$  (the position along the conductor). Equation (2-34) holds if and only if

$$\forall l, \alpha = 90^\circ \text{ and } \beta = 0^\circ, \quad (2-36)$$

or equivalently,  $\hat{u}$ ,  $\vec{B}$  and  $\vec{l}$  are perpendicular to each other at any point of the conductor.

In fact, the special case in (2-34) is often desired in a well-designed electrodynamic transducer, because the transduction coefficient is maximized in this case. Electrodynamic transducers that meet the condition of (2-36) are defined here as “orthogonal electrodynamic transducer”. There are two common configurations that meet the “orthogonal” condition.

The first configuration is shown in [Figure 2-6](#). In this configuration, the magnetic flux lines point into the paper, a straight conductor is allowed to move in the direction perpendicular to its length. The flux lines, the conductor and the velocity vector form a rectangular coordinate. This simple configuration is easy to implement in small size. For example, a microfabricated ET prototype described in [Chapter 5](#) implements this configuration using a clamped-clamped copper beam as the conductor, and magnet assembly is placed on each side of the beam to create the field perpendicular to the beam. However this configuration only allows the conductor to be a straight line, which means that the total length of the conductor can be at most as large as the maximum

dimension of the design space. This strictly reduces the maximum achievable transduction coefficient within a given space.

A second configuration is shown in [Figure 2-7](#). This configuration uses a circular conductor and a radial field pattern, and the conductor is allowed to move along its axis. In this configuration,  $\hat{u}$ ,  $\vec{B}$  and  $\vec{l}$  form a cylindrical coordinate. The circular conductor pattern makes it easy to implement multiple turns, which can increase the transduction coefficient without taking additional design space. A macroscale prototype of this configuration are described in [Chapter 4](#).

## 2.5. Modeling Examples

Using the LEM techniques introduced in [Sections 2.2](#) through [2.4](#), this section demonstrates the modeling procedure for two cases: a pair of inductively coupled coils and an electrodynamic transducer. These two systems are building blocks of the full ET model that will be discussed in [Chapter 3](#). Additionally, a figure of merit coined “coupling strength” for an electrodynamic transducer will be introduced as an important concept that will be used in [Chapter 3](#).

### 2.5.1. Lumped Element Model of Inductively Coupled Coils

Inductively coupled coils are the centerpiece of an EMT. An illustration of a pair of inductively coupled coils is shown in [Figure 2-8](#). The primary coil has  $N_1$  turns. A time-varying current  $i_1$  flows in the primary coil, establishing a time-varying magnetic flux  $\phi_1$ . Some of the magnetic flux lines go through the  $N_2$ -turn secondary coil, inducing a voltage  $v_2$  across the secondary coil. When a load is applied to the secondary coil, a current  $i_2$  flows out from the positive terminal of the secondary coil and back into the negative terminal. The secondary coil current also induces a magnetic flux  $\phi_2$  that

interacts with the field generated by the primary coil and establishes a new field pattern. In this newly established field pattern, some of the magnetic flux lines go through the primary coil and contributes to the voltage drop on the primary coil ( $v_l$ ) which tends to act in opposition to the original current  $i_l$ , and some loop around each individual coils. The portion of the total flux that goes through both coils is the mutually coupled flux ( $\phi_M$ ), while the flux that goes solely through the primary coil is the primary leakage flux ( $\phi_{L1}$ ), and the flux that goes solely through the secondary coil is the secondary leakage flux ( $\phi_{L2}$ ). The relationships between all the flux components are given by

$$\phi_1 = \phi_M + \phi_{L1}, \quad (2-37)$$

and

$$\phi_2 = \phi_M + \phi_{L2}. \quad (2-38)$$

The LEM of the system is shown in [Figure 2-9](#). The model consists of three parts: the primary and the secondary electrical domains and the magnetic domain. Two gyrators with gyration resistance  $N_1$  and  $N_2$  are used to couple the primary and the secondary electrical domains to the magnetic domain.

The primary and the secondary electrical domains include the primary and the secondary coil resistances ( $R_1$  and  $R_2$ ). The source connected to the primary electrical domain can either be voltage source ( $v_s$ ) or current source ( $i_s$ ). The source impedance is ignored for this example. The load connected to the secondary electrical domain is a complex load ( $Z_L$ ). The parasitic capacitances of the coils are assumed to be negligible for this example.

The magnetic domain consists of three permeances:  $\Lambda_M$ ,  $\Lambda_{L1}$  and  $\Lambda_{L2}$ , denoting the permeances of the mutually coupled flux ( $\phi_M$ ) path, the primary and the secondary leakage flux ( $\phi_{L1}$  and  $\phi_{L2}$ ) paths, respectively.

Since the time rate change of the flux, instead of the flux itself, is the flow variable in the magnetic domain, the flows through these three permeances are  $\dot{\phi}_M$ ,  $\dot{\phi}_{L1}$  and  $\dot{\phi}_{L2}$ . Also annotated in the equivalent circuit model are the time rate changes of the total flux through the primary ( $\dot{\phi}_1$ ) and the secondary ( $\dot{\phi}_2$ ) coils. These flows are proportional to the EMFs ( $v_1$  and  $v_2$ ) in the electrical domain.

Since the equivalent circuit model of the inductively coupled coils is well-known in the literature, it is essential to compare this more detailed LEM derived here with the widely accepted electrical-only model. [Figure 2-10](#) demonstrates the process of transforming the LEM in [Figure 2-11](#) to the widely accepted electrical model of the inductively coupled coils.

In step one, the components in the magnetic domain are moved to the primary electrical domain using the properties of the gyrator detailed in [Appendix B](#). After the transformation, all the magnetic compliances are converted to electrical inertances as expected. The equivalent inductance of a permeance  $\Lambda$  is given by

$$L = N^2 \Lambda, \quad (2-39)$$

where  $N$  is the number of coil turns (gyration ratio). Also note that the  $\Pi$ -network in the magnetic domain transforms to a T-network, and the series connected elements have become parallel connected.

In step two, the two cascaded gyrators are combined into a transformer with turns-ratio of  $N_1:N_2$ . This step is also explained with the properties of the gyrator detailed in [Appendix B](#).

In the last step, the inductance  $N_1^2\Lambda_{L2}$  in the primary side of the EMT is moved to the secondary side and becomes  $N_2^2\Lambda_{L2}$ . Finally, the LEM becomes identical to the canonical equivalent circuit, where the leakage inductances ( $L_{L1}$  and  $L_{L2}$ ) are proportional to the leakage permeances ( $\Lambda_{L1}$  and  $\Lambda_{L2}$ ), and the magnetizing inductance ( $L_M$ ) is proportional to the mutually coupled permeance ( $\Lambda_M$ ). This canonical circuit is well-accepted as the standard equivalent circuit model for EMTs operating at low frequency (<1 MHz) [76].

Comparing to the canonical circuit, the LEM derived here provides better physical insights, which is advantageous from the design perspective. Specifically, the model directly shows the parameters of the magnetic domain. This could be helpful to the design of the magnetic circuit. However, from the parameter extraction perspective, the parameters of the canonical circuit are easier to be measured. This will be demonstrated in the model validation process presented in [Chapter 4](#).

### **2.5.2. Lumped Element Model of an Electrodynamic Transducer**

An electrodynamic transducer can operate as a generator or an actuator. In [Section 2.4.2](#), the electrodynamic transduction is introduced from an actuator's perspective. For completeness, this example will be modeled and analyzed as if it is a generator. The transducer models are the same whether it operates as an actuator or a generator, differing only in the positions of the source and the load.

The transducer modeled in this example is shown in [Figure 2-11](#). In this transducer, the force ( $f_s$ ) is directly provided from an external source and drives the coil to move. As the coil moves, the spring force, mechanical damping force, and inertial force are in effect, counteracting the driving force. In addition, the motion induces a voltage across the coil due to the electrodynamic interaction. If a load is connected to the coil, a current will flow, which introduces a magnetic force that also counteracts the driving force.

The lumped element model of the electrodynamic generator is shown in [Figure 2-12](#). In the model, the mechanical domain consists of an effort source  $f_s$  that represents the driving force, generalized inertance  $m$ , resistance  $b$  and compliance  $1/k$  ( $k$  is the stiffness of the cantilever beam) that represents the effective moving mass, mechanical damping coefficient, and the compliance of the cantilever beam, respectively. The electrical domain consists of the coil resistance  $R$  and inductance  $L$ , and the load impedance  $Z_L$ . The mechanical domain is coupled to the electrical domain via a gyrator that represents the electrodynamic transduction. The gyration resistance  $K$  is equal to the electrodynamic transduction coefficient of the device. This lumped element model is in agreement with the equivalent circuit model of electrodynamic generators in the literatures [77, 78].

For simplicity, the operating frequency and the coil inductance are assumed to be sufficiently low so that the reactance of the inductance is much smaller than the coil resistance. In this case, the coil inductance can be ignored. Further assuming that the load is purely resistive ( $R_L$ ), the force to load voltage transfer function can be obtained as

$$\frac{V_L(s)}{F_s(s)} = \frac{K \frac{R_L}{R+R_L}}{ms + b + \frac{k}{s} + \frac{K^2}{R+R_L}}. \quad (2-40)$$

With a sinusoidal force excitation at the mechanical natural frequency  $f_n = \frac{1}{2\pi} \sqrt{\frac{k}{m}}$ , the load voltage amplitude goes to a maximum:

$$V_L = \frac{F_s K R_L}{b(R+R_L) + K^2}. \quad (2-41)$$

The average load power is given by

$$P_{out} = \frac{V_L^2}{2R_L} = \frac{F_s^2 K^2 R_L}{2[b(R+R_L) + K^2]^2}. \quad (2-42)$$

The maximum power is obtained when the load resistance is equal to the output impedance of the transducer:

$$R_{L\_opt} = R + \frac{K^2}{b}, \quad (2-43)$$

and the maximum load power is given by

$$P_{out\_max} = \frac{F_s^2 K^2}{8b(Rb + K^2)} = \frac{F_s^2}{8b \left( \frac{1}{\gamma} + 1 \right)}, \quad (2-44)$$

where  $\gamma = \frac{K^2}{Rb}$  is defined as the “coupling strength” of the electrodynamic transducer.

The coupling strength is a useful non-dimensional metric that measures the effectiveness of electrodynamic transduction. In this example, the higher the coupling strength, the more power can be generated on the load, given that the excitation force amplitude is constant. When the coupling strength is much greater than 1, or

$$\gamma = \frac{K^2}{Rb} \gg 1, \quad (2-45)$$

the load power will approach the absolute maximum  $\frac{F_s^2}{8b}$ . In this case, the transducer is called “strongly coupled”.

In order to increase the coupling strength of a transducer, a large transduction coefficient, as well as a small conductor resistance and damping coefficient is desired. Since orthogonal transducers introduced in [Section 2.4.2](#) tend to maximize the transduction coefficient, orthogonal transducer topologies are favorable designs that are going to be used for the ETs in this work.

Table 2-1. List of general representations of elements in a transducer lumped element model.

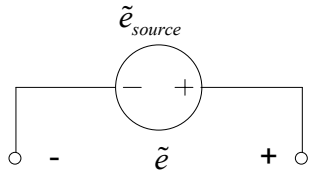
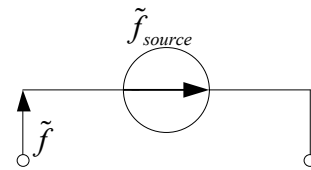
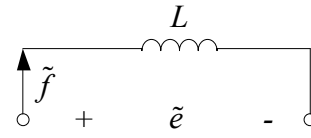
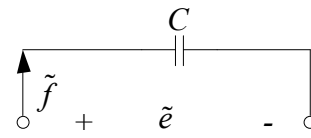
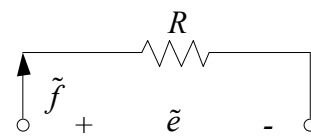
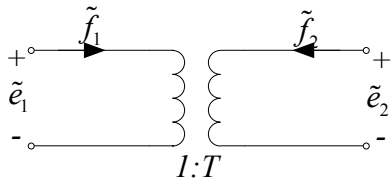
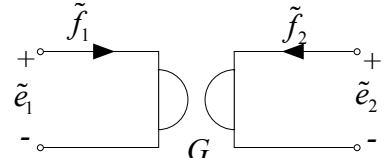
Element	Symbol	Characteristic equation
Effort source		$\tilde{e} = \tilde{e}_{source}$
Flow source		$\tilde{f} = \tilde{f}_{source}$
Generalized inductance		$\tilde{e} = L \frac{d\tilde{f}}{dt}$
Generalized capacitance		$\tilde{f} = C \frac{d\tilde{e}}{dt}$
Generalized resistance		$\tilde{e} = R\tilde{f}$
Transformer		$\tilde{e}_2 = T\tilde{e}_1$ $\tilde{f}_2 = -\frac{1}{T}\tilde{f}_1$
Gyrator		$\tilde{e}_2 = G\tilde{f}_1$ $\tilde{f}_2 = -\frac{1}{G}\tilde{e}_1$

Table 2-2. Conjugate power variables and fundamental elements in different energy domains.

Variables and elements	Mechanical domain	Electrical domain	Magnetic domain
Flow variable	Linear velocity ( $u$ )	Current ( $i$ )	Time rate change of flux ( $\dot{\phi}$ )
Effort variable	Force ( $f$ )	Voltage ( $v$ )	Magnetomotive force ( $MMF$ )
Generalized inertance	Mass ( $m$ )	Inductance ( $L$ ) <sup>*</sup>	Undefined
Generalized compliance	Compliance, or inverse of spring constant ( $1/k$ )	Capacitance ( $C$ )	Permeance, or inverse of reluctance ( $\Lambda = 1/\mathfrak{R}$ ) <sup>*</sup>
Generalized resistance	Damping coefficient ( $b$ )	Resistance ( $R$ )	Undefined

\* Inductance and permeance are repeated definition of a same physical phenomenon, only one should be used.

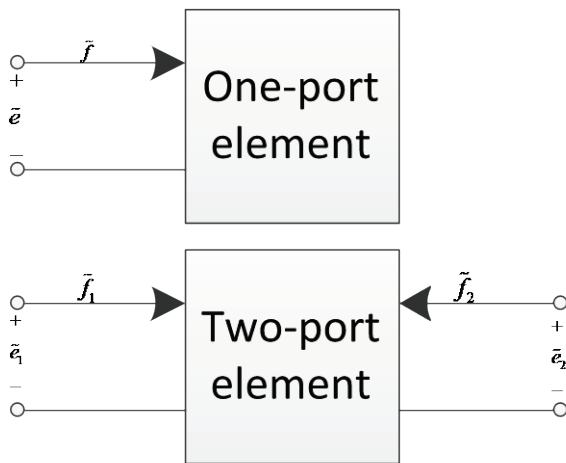


Figure 2-1. One-port and two-port elements.

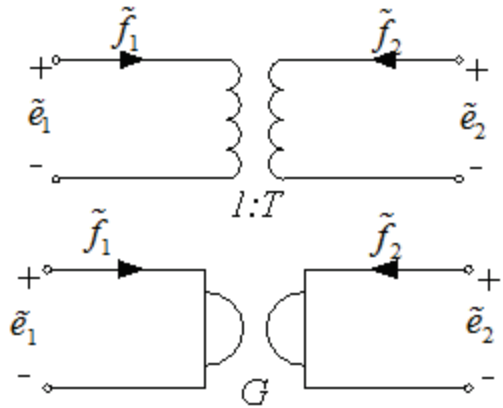


Figure 2-2. Transformer and gyrator.

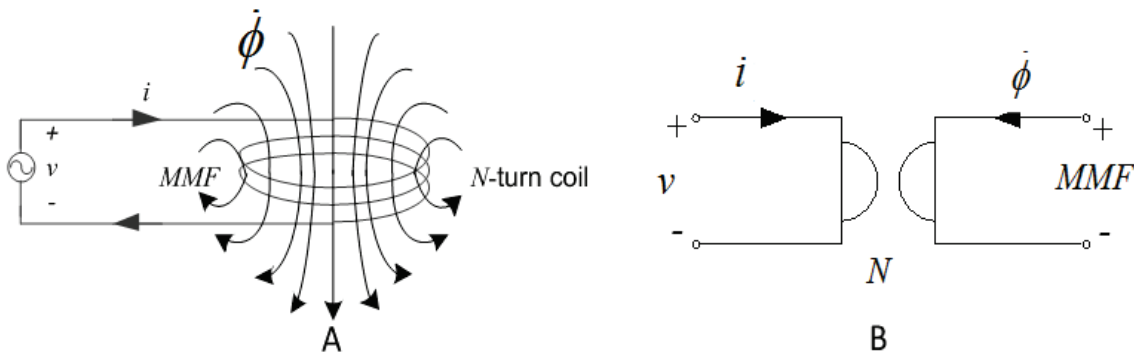


Figure 2-3. Electromagnetic coupling. A) The illustration. B) The lumped element model.

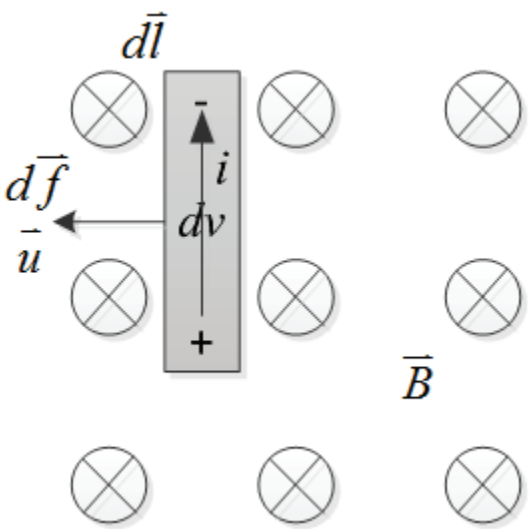


Figure 2-4. Illustration of electrodynamic transduction.

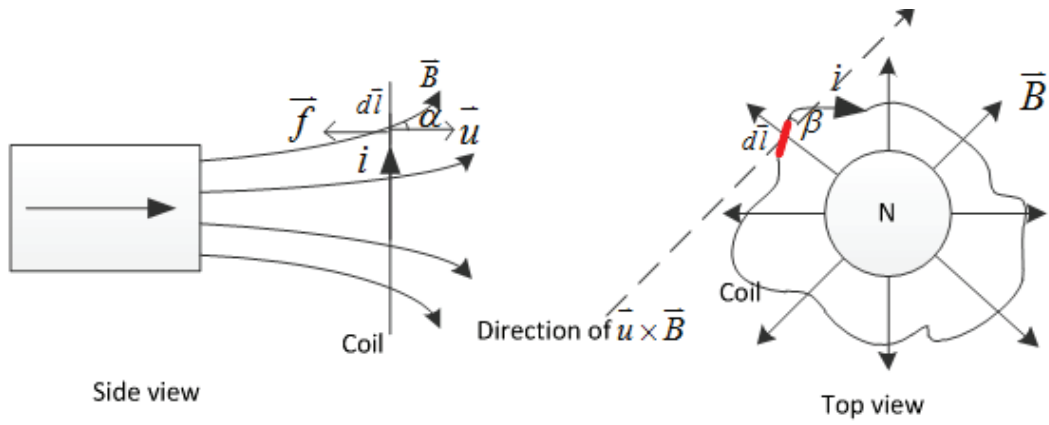


Figure 2-5. Electrodynamic transduction with non-uniform magnetic field and arbitrary coil.

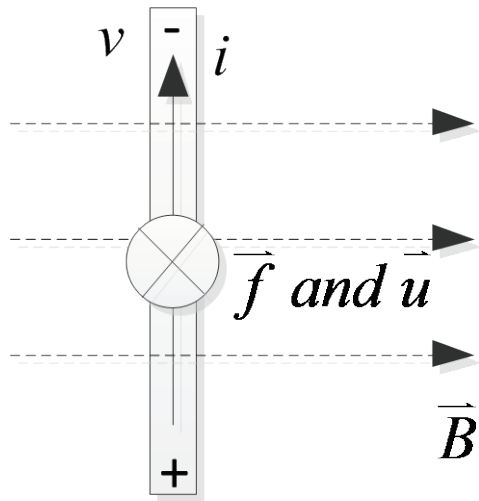


Figure 2-6. Electrodynamic transduction configuration with straight conductor.

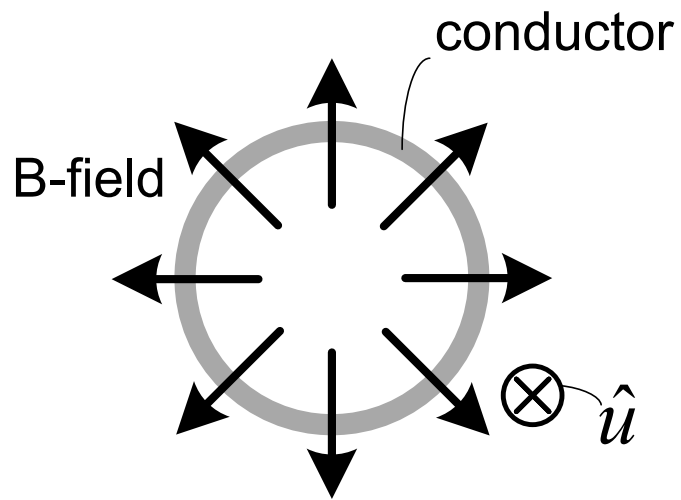


Figure 2-7. Electrodynamics transduction configuration with circular conductor and radial field.

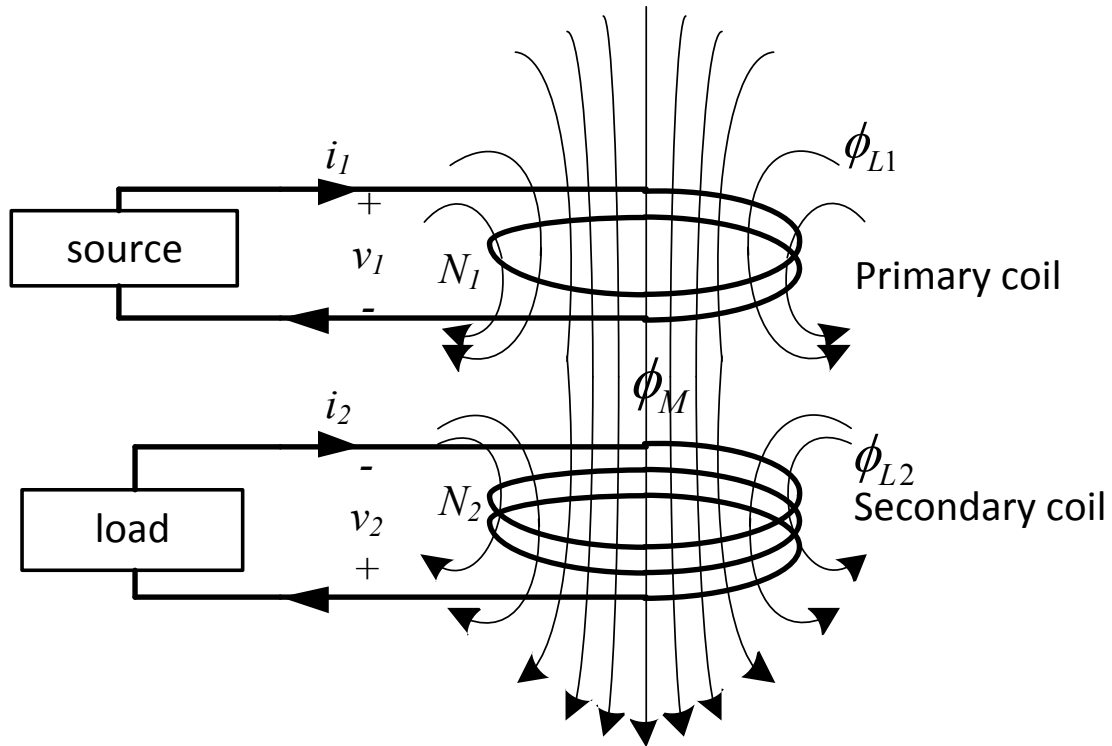


Figure 2-8. Illustration of a pair of inductively coupled coils.

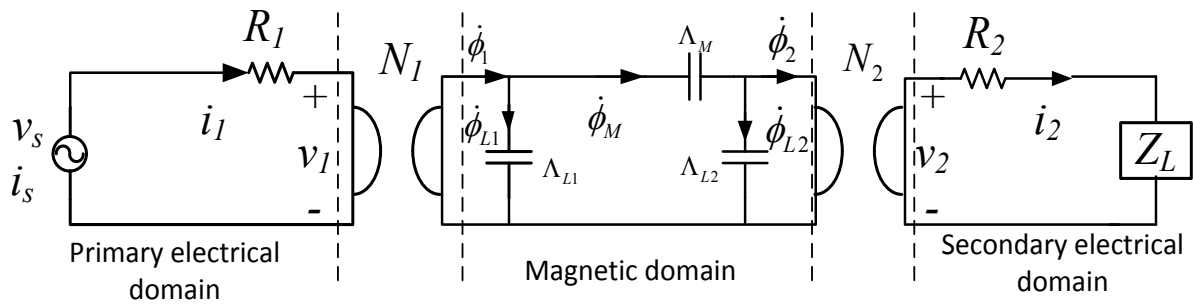


Figure 2-9. Lumped element model of the inductively coupled coils.

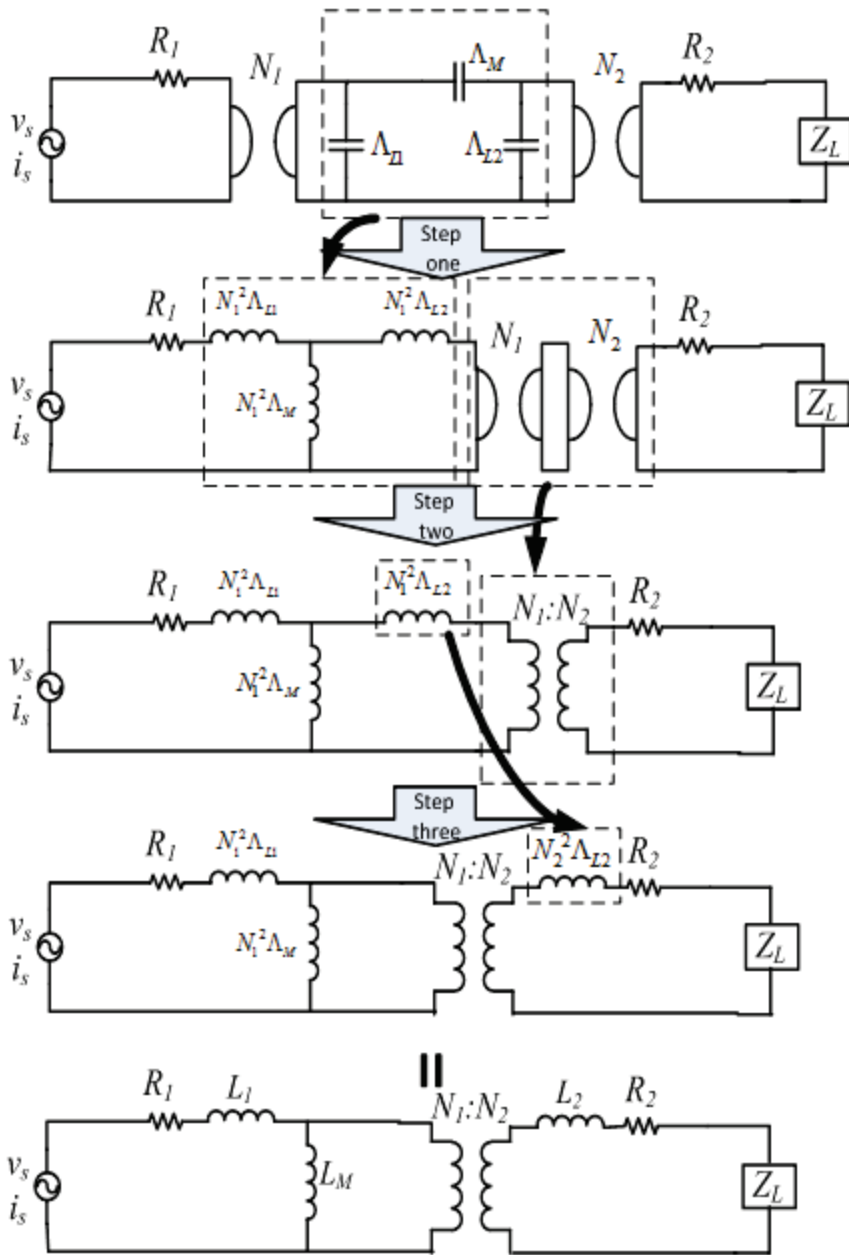


Figure 2-10. Transforming the developed lumped element model to the canonical equivalent circuit model of the inductively coupled coils.

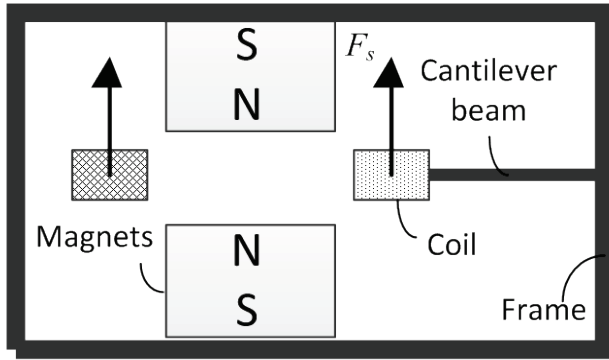


Figure 2-11. Electrodynamic generator in the example.

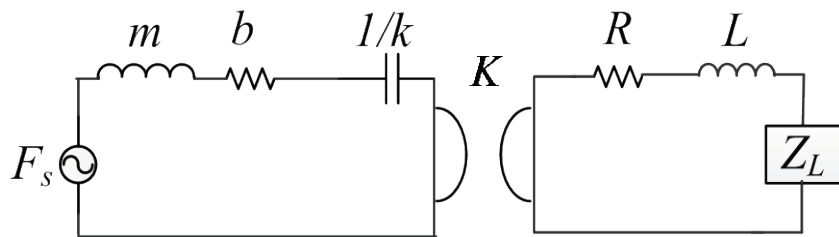


Figure 2-12. Lumped element model of the electrodynamic generator.

## CHAPTER 3 ELECTRODYNAMIC TRANSFORMER THEORY

Based on the general transducer theory developed in [Chapter 2](#), this chapter focuses on the theory of the ET and its comparison with the other types of transformers. The first section provides a detailed description of the ET's working principle and possible implementations. In the next section, a generic LEM of the ET is developed for theoretical analysis. The performance of ET is then analyzed with the LEM and compared with EMT and PT transformer technologies. It should be noted that this model will be validated in [Chapter 4](#) through experiments on a prototype device.

### **3.1. Device Overview**

An ET consist of six essential functional elements: a magnetic assembly that establishes a magnetic field to enable electrodynamic transduction, a primary conductor that provides the input port of the device and carries current to create the electrodynamic force that drives the vibration, a secondary conductor that senses the vibration and generates output voltage/current, a moving mass that carries the vibrational kinetic energy, a compliance element that constrains the mechanical vibration and creates resonance, and a frame that holds the device elements together and provides anchor point for the compliance element. However, one single component can play the roles of multiple elements. For example, the magnets or the conductors can have dual function as the moving mass, the compliance element, or even the frame. Typically, a dedicated moving mass is not necessary and is undesired from a design standpoint, because both magnets and conductors have significant density and already occupy a large fraction of the functional volume. Even if additional mass is needed, increasing the volume of the conductors and the magnets are generally more beneficial

to the overall performance than adding a dedicated “dead” mass. To implement electrodynamic transduction, the magnetic assembly must move relative to the conductors. Furthermore, in order not to add complexity, the two conductors do not move with regards to each other.

Based on the constraints established above, there are at least three possible ET implementations:

- Type A: the conductors form a rigid moving mass, the magnetic assembly is fixed to the frame, and a dedicated spring is used to provide compliance between the mass and the frame.
- Type B: the magnetic assembly forms a rigid moving mass, the conductors are fixed to the frame, and a dedicated spring is used to provide compliance between the mass and the frame.
- Type C: the conductors form a bending, compliant moving mass, and the magnetic assembly is fixed to the frame.

Type A implementation is illustrated in [Figure 3-1\(a\)](#). Since the magnetic assembly is fixed to the frame, it is easier for this type of ET to establish a desired magnetic field pattern that maximizes the coupling coefficient. However, since the conductors are moving, it is comparatively difficult to establish electrical connections with the external circuit. The wire connections inevitably increase the mechanical damping and stiffness of the compliant element, along with the associated uncertainties. A demonstration of type A device can be found in [Section 4.1](#).

Type B implementation is shown in [Figure 3-1\(b\)](#). In this type of device, the conductors are fixed to the frame, therefore making the electrical connections easier. However, the design of a moving magnetic assembly is challenging due to the limited space. Experimental demonstration of Type B implementation is not presented in the dissertation.

Type C implementation is shown in [Figure 3-1\(c\)](#). Similar to the Type A implementation, the conductors serve as the moving parts. However, to alleviate the wire connection issue, the compliance element is also implemented by the conductors. Therefore, the Type C implementation combines the benefits of Type A and Type B implementations. In addition, since no dedicated spring is needed, future microfabrication of Type C device may be simplified, although the design space may be more constrained since the use of the conductors as the compliance element limits the dimensions and material selection. A microfabricated Type C ET is demonstrated in [Chapter 5](#).

### **3.2. Lumped Element Model of Electrodynamic Transformers**

The LEM is primarily concerned about the fundamental energetic elements that are included in the device, no matter how these elements are physically implemented. For example, even if the conductors and the moving mass share the same physical body, they are modeled separately in the LEM. Therefore, all three types of implementations share the same LEM topology. The difference only lies in the relative values of different parameters. For example, as will be explained later, the parasitic inductive and capacitive coupling between the two conductors may be stronger in Type A and Type C devices as compared to Type B devices, because the conductors may be closer to each other.

The complete model of an ET is shown in [Figure 3-2](#). The LEM includes three energy domains: electrical, mechanical and magnetic. The electrical domain models the resistance of the conductors, parasitic capacitance of the input and output ports, and parasitic coupling capacitance between the conductors. The mechanical domain models

the effective moving mass, spring compliance, and mechanical damping coefficient. The magnetic domain models the permeances of the ac flux paths.

Between the source and the load, there are two primary energy flow paths: the electrodynamic coupling path and the inductive coupling path. The electrodynamic coupling path is the primary path. It consists of the primary conductor electrical domain, the primary electrodynamic transduction, the mechanical domain, the secondary electrodynamic transduction, and the secondary conductor electrical domain. This energy flow path is simply a cascaded electrodynamic actuator and generator. The inductive coupling path consists of the primary conductor electrical domain, the primary electromagnetic transduction, the magnetic domain, the secondary magnetic transduction, and the secondary conductor electrical domain. This energy flow path is identical to the inductively coupled coils.

It should be mentioned that there exists a third possible energy transfer path via capacitive coupling. The capacitive coupling path would consist of the primary electrical domain, the parasitic coupling capacitance, and the secondary electrical domain. However, in this work, the devices being investigated have feature sizes from centimeters down to millimeters and operate at frequencies in the audio range (from tens of Hertz to tens of kilo Hertz). In this case, the parasitic capacitances (including self capacitances and coupling capacitance) are typically below nano Farads, and corresponding parallel reactances are typically very high ( $> 100 \text{ k}\Omega$ , or  $>1000$  times higher than the typical net ET input impedance). Thus, in an equivalent circuit representation, the capacitive elements can be safely ignored (treated as open-circuits).

In the moving-magnet topology (Type B), since the two conductors may be located far from one another on the frame, the inductive coupling energy flow path may be small and thus negligible. However, for moving-conductor topologies (Type A and Type C), the conductors are typically much closer to each other, the inductive coupling may be significant. The ability to neglect the electromagnetic coupling has great implication on the complexity of the supporting models. This issue will be more fully explored in the next section.

### **3.3. Electrodynamic Transformer Model Analysis**

The complete LEM of the ET is useful for performance prediction using circuit simulation tools (LTSpice simulation is demonstrated in [Chapter 4](#)). However, the analytical expressions (e.g. transfer function, power efficiency) derived from the LEM is too complicated to perform design-oriented analysis. This section attempts to simplify the model by imposing reasonable assumptions, so that simplified analytic expressions can be derived. The primary simplifying assumption is that the inductive coupling is negligible, i.e. the magnetic domain energy transfer path can be ignored. A further simplification is defined when the ET can be considered “strongly coupled.” In this section, the conditions for the simplifications are first discussed. Then, the simplified model that ignores the inductive coupling is analyzed for its voltage gain, power efficiency and power capacity. Performance predictions are provided for the general case, and for the “strongly coupled” case.

#### **3.3.1. Conditions for Ignoring the Inductive Coupling**

The primary electrical domain interacts with the rest of the model via two series-connected gyrators: one for the electrodynamic transduction, the other for the electromagnetic transduction. If the electromagnetic transduction has much smaller

impact than the electrodynamic transduction, its effect can be ignored. To quantify the impact, the voltage drop across each gyrator on the primary side is calculated. A similar argument can be made for the secondary electrical domain.

For the primary electrodynamic transduction, the amplitude of the voltage drop is given by

$$V_{ed\_1} = K_1 U, \quad (3-1)$$

where the subscript “ed” stands for electrodynamic, and “1” stands for the primary side, and  $U$  is the amplitude of the vibration velocity. For the electromagnetic transduction, the amplitude of the voltage drop is given by

$$V_{em\_1} = 2\pi f N_1 (\Phi_{L1} + \Phi_M) = 2\pi f N_1 [N_1 I_1 \Lambda_{L1} + (N_1 I_1 - N_2 I_2) \Lambda_M], \quad (3-2)$$

where the subscript “em” stands for electromagnetic,  $f$  is the operating frequency,  $\Lambda_{L1}$  and  $\Lambda_M$  are the leakage permeance of the primary conductor and the mutual permeance between the primary and secondary inductors, respectively,  $N_1$  and  $N_2$  are the primary and the secondary number of coil turns, respectively, and  $I_1$  and  $I_2$  are the current amplitudes in the primary and secondary conductors, respectively. It is clear that when  $V_{ed\_1} \gg V_{em\_1}$ , the electromagnetic transduction can be ignored from the primary side. This analysis ignores any phase information between these two voltages; the argument is purely based on the magnitude. For the secondary side, the result is similar:

$$V_{ed\_2} = K_2 U, \quad (3-3)$$

$$V_{em\_2} = 2\pi f N_2 (\Phi_M - \Phi_{L2}) = 2\pi f N_2 [(N_1 I_1 - N_2 I_2) \Lambda_M - N_2 I_2 \Lambda_{L2}], \quad (3-4)$$

and the condition to ignore the electromagnetic coupling is  $V_{ed\_2} \gg V_{em\_2}$ .

The results above are difficult to interpret from a physical standpoint. However, assuming that the device operates at the mechanical natural frequency ( $f=f_n$ ) and that the currents in the primary and the secondary conductors are in phase (these assumptions will be justified later in this subsection), the velocity amplitude is given by

$$U = \frac{K_1 I_1 - K_2 I_2}{b}. \quad (3-5)$$

Substituting (3-5) into (3-1) and (3-3), the conditions for ignoring the electromagnetic coupling on both side, and therefore ignoring the whole magnetic domain at the mechanical natural frequency is given by

$$f_n \ll \frac{K_1 I_1 - K_2 I_2}{2\pi b} \min \left\{ \frac{K_1}{N_1 [N_1 I_1 \Lambda_{L1} + (N_1 I_1 - N_2 I_2) \Lambda_M]}, \frac{K_2}{N_2 [(N_1 I_1 - N_2 I_2) \Lambda_M - N_2 I_2 \Lambda_{L2}]} \right\}. \quad (3-6)$$

Equation (3-6) only gives the condition for ignoring the magnetic domain at the mechanical natural frequency where the primary and the secondary currents are in phase. However, further observation will find that if the frequency is not equal to the natural frequency, and there is a phase difference between the primary and the secondary currents, then the average velocity of the translator for given  $I_1$  and  $I_2$  would be even higher than what is predicted by (3-5). Thus, the electrodynamic contribution to the electrical domain voltage drop would be even larger than the electromagnetic contribution. Therefore, it is safe to state that for any operating frequency, the magnetic domain (inductive coupling) can be ignored as long as

$$f \ll \frac{K_1 I_1 - K_2 I_2}{2\pi b} \min \left\{ \frac{K_1}{N_1 [N_1 I_1 \Lambda_{L1} + (N_1 I_1 - N_2 I_2) \Lambda_M]}, \frac{K_2}{N_2 [(N_1 I_1 - N_2 I_2) \Lambda_M - N_2 I_2 \Lambda_{L2}]} \right\}. \quad (3-7)$$

It needs to be noted that ignoring the inductive coupling in an ET model is different from ignoring the coil inductance in the electrodynamic transducer model discussed in [Section 2.5.2](#). In the transducer case, the impact of the inductance is compared to that of the coil resistance via its reactance, while in the ET case, the impact of the inductive coupling is compared to the impact of the electrodynamic coupling via its voltage contribution in the electrical domains.

### 3.3.2. Analysis of the Simplified Model

When the ET meets the conditions defined by (3-7), the ET model can be simplified by ignoring the inductive coupling (i.e. ignoring the magnetic domain). The simplified model is shown in [Figure 3-3](#). From this simplified model the voltage gain, input/output power, efficiency, and power capacity of the ET are analyzed.

#### 3.3.2.1. Voltage Gain and Power

With a voltage source  $V_s$  connected to the primary port, the open-circuit voltage transfer function is given by

$$\frac{V_{oc}(s)}{V_s(s)} = \frac{K_1 K_2}{R_1 \left( ms + b + \frac{k}{s} \right) + K_1^2}. \quad (3-8)$$

The voltage gain goes to maximum when the operating frequency matches the mechanical natural frequency. Under this condition, the maximum open-circuit voltage gain is

$$\left. \frac{V_{oc}}{V_s} \right|_{f = \frac{1}{2\pi} \sqrt{\frac{k}{m}}} = \frac{K_2}{K_1} \frac{K_1^2}{R_1 b + K_1^2} = \frac{K_2}{K_1} \frac{1}{\gamma_1 + 1}, \quad (3-9)$$

It can be seen that if the primary side is strongly coupled, the open-circuit voltage gain will be close to the ratio of the two transduction coefficients. As will be discussed in

Section 3.3, this is very similar to the behavior of EMT, where the open-circuit voltage gain is close to the turns ratio if the inductive coupling is strong.

Also note that at the natural frequency, the output voltage is in phase with the source voltage. Therefore, if a resistive load is attached, the primary and the secondary currents are in phase. This validates one assumption made in deriving (3-6) in Section 3.3.2.1.

Now assuming that the ET operates at the natural frequency and with a resistive load  $R_L$  connected to the secondary port, the voltage gain is given by

$$\frac{V_L}{V_s} = \frac{K_2}{K_1} \frac{1}{\left(1 + \frac{1}{\gamma_1}\right) \left(1 + \frac{R_2}{R_L}\right) + \frac{\gamma_2 R_2}{\gamma_1 R_L}}. \quad (3-10)$$

Therefore the average load power is

$$P_{out} = \frac{V_L^2}{2R_L} = \frac{V_s^2}{2R_L} \left[ \frac{K_2}{K_1} \frac{1}{\left(1 + \frac{1}{\gamma_1}\right) \left(1 + \frac{R_2}{R_L}\right) + \frac{\gamma_2 R_2}{\gamma_1 R_L}} \right]^2. \quad (3-11)$$

On the other hand, the average power provided by the source is given by

$$P_{in} = \frac{V_s^2}{2 \left[ R_1 + \frac{K_1^2}{b + \frac{K_2^2}{R_2 + R_L}} \right]} = \frac{V_s^2}{2R_1 \left[ 1 + \frac{\gamma_1 (R_2 + R_L)}{(1 + \gamma_2) R_2 + R_L} \right]}. \quad (3-12)$$

The voltage gain and power expressions in (3-10), (3-11) and (3-12) can be further simplified if the ET is “strongly coupled,” which requires that both the primary and the

secondary transduction satisfy (2-45). In a strongly coupled ET, the voltage gain is simplified to

$$\left. \frac{V_L}{V_s} \right|_{strong} = \frac{K_2}{K_1} \frac{1}{1 + \left(1 + \frac{\gamma_2}{\gamma_1}\right) \frac{R_2}{R_L}}. \quad (3-13)$$

The output power can be simplified to

$$P_{out\_strong} = \frac{V_s^2 \gamma_2 R_2}{2\gamma_1 R_1 R_L} \left[ \frac{1}{1 + \left(1 + \frac{\gamma_2}{\gamma_1}\right) \frac{R_2}{R_L}} \right]^2. \quad (3-14)$$

The input power can also be simplified to

$$P_{in\_strong} = \frac{V_s^2 (\gamma_2 R_2 + R_L)}{2R_1 [(\gamma_1 + \gamma_2) R_2 + \gamma_1 R_L]}. \quad (3-15)$$

Note that the use of the strongly coupled assumption increases the calculated voltage gain and the output power, while decreases the input power. The discrepancy between this “ideal” behavior and the actual (non-strongly coupled) behavior increases as the actual coupling strength decreases.

### 3.3.2.2. Power Efficiency

The expression of power efficiency for non-strongly coupled ET is too complicated to provide any physical insight. Therefore, strongly coupled assumption is directed applied, and the power efficiency can be obtained as

$$\eta_{strong} = \frac{P_{out\_strong}}{P_{in\_strong}} = \frac{\gamma_1 \gamma_2 R_2 R_L}{(\gamma_2 R_2 + R_L) [ \gamma_1 R_L + (\gamma_1 + \gamma_2) R_2 ]}. \quad (3-16)$$

By using an optimum load resistance, a maximum efficiency of

$$\eta_{\max} = \frac{1}{\left( \sqrt{\frac{1}{\gamma_1} + \frac{1}{\gamma_2} + 1} \right)^2} \quad (3-17)$$

is obtained when

$$R_L = \sqrt{\frac{(\gamma_1 + \gamma_2)\gamma_2}{\gamma_1}} R_2. \quad (3-18)$$

Note that (3-17) predicts a higher efficiency than does the non-strongly coupled model, because the higher output power and lower input power caused by the use of strongly coupled assumption. As the actual coupling strength decreases, the prediction error increases.

Using the strongly coupled efficiency equation, i.e. (3-17), a contour plot of efficiency vs.  $\gamma_1$  and  $\gamma_2$  is shown in [Figure 3-4](#). It can be seen that over 90% efficiency is possible when  $\gamma_1$  and  $\gamma_2$  are both greater than 1000. Here the accuracy of the plot increases with decreasing coupling strength. In order to estimate the efficiency with the full model, the knowledge of the primary and secondary conductor resistances is necessary.

### 3.3.2.3. Power Capacity

The maximum possible output power is limited by the stress and strain limits of the compliance element, and also by the maximum current density in the primary and secondary conductors. The maximum stress and strain may be limited by the material strength or spatial limit. The maximum current density may be limited by the heat dissipation condition or electromigration effect. Suppose that the stress and strain limits are interpreted as the maximum force ( $F_{max}$ ) and displacement ( $X_{max}$ ) amplitudes of the spring, and the maximum current density is interpreted as the maximum primary ( $I_{I_{max}}$ )

and secondary ( $I_{2max}$ ) current amplitudes. For a given device, one of these four limiting factors may become dominant. The power capacity when each of the four limiting factors become dominant are analyzed below.

### Force limited case

In this case, the force amplitude on the spring reaches the limit before any of the other three does. When the maximum load power is achieved in this case, the following conditions apply:

$$F = F_{\max}, X = \frac{U}{2\pi f_n} \leq X_{\max}, \text{ and } I_{1,2} \leq I_{1,2\max}. \quad (3-19)$$

The velocity amplitude is given by

$$U = \frac{F_{\max}}{b}. \quad (3-20)$$

Therefore the load voltage is given by

$$V_L = \frac{K_2 U R_L}{R_2 + R_L} = \frac{K_2 F_{\max}}{b} \frac{R_L}{R_2 + R_L}, \quad (3-21)$$

and the load power is given by

$$P_{out} = \frac{V_L^2}{2R_L} = \frac{K_2^2 F_{\max}^2 R_L}{2b^2 (R_2 + R_L)^2} \leq \frac{K_2^2 F_{\max}^2}{8b^2 R_2}, \quad (3-22)$$

where the maximum output power is achieved when the load resistance is equal to the secondary conductor resistance. Note that the power capacity specified in (3-22) is true only when (3-19) is satisfied. Specifically, the designed space for motion must be greater than or equal to the stroke corresponding to the maximum force; the secondary current under the load condition must be smaller than or equal to the limit; and the input

voltage must be sufficiently large that the mechanical force reaches the limit, but the primary current must still within the limit.

### Displacement limited case

In this case, the strain of the compliance element reaches the material limit, or the stroke of the moving part reaches the designed space limit, before any other limit is reached. If the maximum power is reached in this case, the following conditions apply:

$$F \leq F_{\max}, X = \frac{U}{2\pi f_n} = X_{\max}, \text{ and } I_{1,2} \leq I_{1,2\max}. \quad (3-23)$$

The velocity amplitude is given by

$$U = 2\pi f_n X_{\max}. \quad (3-24)$$

Therefore the load voltage is given by

$$V_L = \frac{K_2 U R_L}{R_2 + R_L} = \frac{2\pi f_n X_{\max} K_2 R_L}{R_2 + R_L}. \quad (3-25)$$

And the load power is given by

$$P_{out} = \frac{V_L^2}{2R_L} = \frac{2\pi^2 f_n^2 X_{\max}^2 K_2^2 R_L}{(R_2 + R_L)^2} \leq \frac{\pi^2 f_n^2 X_{\max}^2 K_2^2}{2R_2}, \quad (3-26)$$

where the maximum output power is achieved when the load resistance is equal to the secondary conductor resistance. Note that the power capacity specified in (3-26) is true only when (3-23) is satisfied. In this case, the compliance material must be sufficiently strong to withstand the stress corresponding to the displacement; the source must provide sufficient voltage to drive the vibration to the displacement limit, while the primary and the current still within the limit.

### Primary current limited case

In this case, the primary current amplitude reaches the limit before any of the other three does:

$$F \leq F_{\max}, X = \frac{U}{2\pi f_n} \leq X_{\max}, I_1 = I_{1\max}, \text{ and } I_2 \leq I_{2\max}. \quad (3-27)$$

The velocity amplitude is given by

$$U = \frac{V_s - R_1 I_{1\max}}{K_1}. \quad (3-28)$$

Therefore the load voltage is given by

$$V_L = \frac{K_2 U R_L}{R_2 + R_L} = \frac{K_2 (V_s - R_1 I_{1\max}) R_L}{K_1 (R_2 + R_L)}. \quad (3-29)$$

And the load power is given by

$$P_{out} = \frac{V_L^2}{2R_L} = \frac{K_2^2 (V_s - R_1 I_{1\max})^2 R_L}{2K_1^2 (R_2 + R_L)^2} \leq \frac{K_2^2 (V_s - R_1 I_{1\max})^2}{8K_1^2 R_2}, \quad (3-30)$$

where the maximum output power is achieved when the load resistance is equal to the secondary conductor resistance. The conditions for achieving this power capacity are that: the source must provide sufficient current so that the primary current limit is reached; and the mechanical force and displacement limits, as well as the secondary current limit must be able to sustain such amount of input current, under the optimum loading condition.

#### Secondary current limited case.

In this last case, the secondary current limit is reached before the others:

$$F \leq F_{\max}, X = \frac{U}{2\pi f_n} \leq X_{\max}, I_1 \leq I_{1\max}, \text{ and } I_2 = I_{2\max}. \quad (3-31)$$

And the load power is directly calculated as

$$P_{out} = \frac{I_{2max}^2 R_L}{2}. \quad (3-32)$$

It seems like the load power in this case is not bounded as long as the load resistance keeps increasing. However, this is not true because the generator must be able to supply sufficiently high voltage so that the secondary current is kept at the maximum. Therefore, there is a limit to the load resistance, as well as to the load power. The maximum load resistance must meet the following conditions:

$$R_{Lmax} \leq \frac{K_2}{I_{2max}} \min \left\{ 2\pi f_n X_{max}, \frac{F_{max}}{b}, \frac{V_s - R_1 I_{1max}}{K_1} \right\} - R_2. \quad (3-33)$$

The maximum load power can be estimated by substituting (3-33) into (3-32).

In order to find the true power capacity of an ET device, the primary limiting factor of the device needs to be first estimated, and the equations discussed above can be used to estimate the corresponding load condition of the maximum load power. Once this condition is specified, a simulation or analytical calculation can be performed to confirm the primary limiting factor. If the conditions for the primary limiting factor are not met, another primary limiting factor must be used.

It needs to be noted that in real ET devices, the system behavior may become highly nonlinear before these limits are approached. The sources of nonlinearity include over bending of the beam, increase of resistivity due to the high current induced temperature rise, variation of the transduction coefficient due to the wide range of motion, etc. In this case, a model that takes into account the nonlinearity needs to be used to calculate the power capacity. This work only attempts to investigate the potential of the ET concept, therefore accurately predicting the performance of a

practical device requires a substantial amount of research beyond the scope of this work.

### 3.4. Performance Limits and Scaling Laws of Electrodynamic Transformers

[Section 3.3](#) investigated the maximum efficiency and power capacity for a certain ET device. The optimum source and/or loading conditions have been discussed for a certain device to reach maximum efficiency or output power. In this section, a higher-level investigation is performed to estimate absolute performance limits of the ET and their relationship to the device physical scale. The limits discussed in this section are not bounded by the parameters of a certain device. Instead, they are determined by the fundamental nature of the ET's working principle and feasibility of the material properties.

#### 3.4.1. Limit of Power Efficiency

It is evident from (3-17) that the maximum power efficiency of a strongly coupled ET is an increasing function of the primary and secondary coupling strengths. The limit of the maximum power efficiency is equivalent to the limit of the achievable coupling strength. Therefore, coupling strength is revisited here with more depth.

The definition of coupling strength in [Section 2.5.2](#) is rewritten here,

$$\gamma = \frac{K^2}{Rb}. \quad (3-34)$$

According to the definition of transduction coefficient in [Section 2.4.2](#),

$$K = \oint_{l_c} B \sin \alpha \cos \beta dl = B_{eff} l_c, \quad (3-35)$$

where

$$B_{eff} = \frac{1}{l_c} \oint_{l_c} B \sin \alpha \cos \beta dl \quad (3-36)$$

is the effective flux density, which is equal to the line average flux density component that is perpendicular to the conductor length and the velocity. In the case of a circular conductor, this flux density is the average radial flux density component along the conductor; for straight conductor, it is the average transverse flux density component along the conductor.

Also note that the conductor resistance is given by

$$R = \frac{\rho_c l_c}{A_c}, \quad (3-37)$$

where  $\rho_c$  is the resistivity of the conductor, and  $A_c$  is the average cross section area of the conductor. Further note that the damping coefficient can be written as

$$b = \frac{\sqrt{mk}}{Q} = 2\pi f_n m = 2\pi f_n \rho_m \mathcal{V}_m, \quad (3-38)$$

where  $Q$  and  $f_n$  are the mechanical quality factor and natural frequency of the resonator, respectively, and  $\rho_m$  and  $\mathcal{V}_m$ , are the density and the effective motional volume of the mass (may be smaller than the actual volume, for example in a beam), respectively.

Substituting (3-35), (3-37), and (3-38) into (3-34),

$$\gamma = \frac{B_{eff}^2 Q \mathcal{V}_c}{2\pi f_n \rho_c \rho_m \mathcal{V}_m} = (B_{eff}^2) \left( \frac{Q}{2\pi f_n} \right) \left( \frac{1}{\rho_c \rho_m} \right) \left( \frac{\mathcal{V}_c}{\mathcal{V}_m} \right), \quad (3-39)$$

where  $\mathcal{V}_c = l_c A_c$  is the volume of the conductor. It can be seen that the coupling strength depends on four major factors: the magnetic field pattern, mechanical performance, material properties, and device topology. Each factor is represented by the quantities in

one of the brackets in (3-39). They are discussed separately in the following paragraphs.

The magnetic flux density can be increased by strategically arranging the magnets. For example, a uniform flux density over 2 T is possible inside a Halbach cylinder [79] as shown in [Figure 3-5](#). For circular conductor, since a radial field pattern is needed for orthogonal transduction, a more complicated structure is required to create such high flux density. It is generally easier for moving conductor type topologies to achieve higher flux density.

The coupling strength is also proportional to the ratio between the quality factor and the natural frequency. Since the quality factor is equal to  $2\pi$  times the number of oscillation cycles before the mechanical energy decreases to  $1/e$  of its initial value,

$\frac{Q}{2\pi f_n}$  is equal to the time (in seconds) required before the resonator's mechanical

energy decreases to  $1/e$  of its initial value. Therefore, this factor is inversely proportional to the decay rate of the resonator. It is hard to estimate the limit of this term, because the underlying physics of mechanical quality factor is too complicated to generalize.

However, from the demonstration device that will be shown in [Chapter 4](#), this factor can at least reach  $\sim 1$  s.

On the material perspective, a highly conductive conductor and a low density mass are desired. In the case of moving conductor topology where the mass and the conductor are the same, a low resistivity and low density material is desired. [Table 3-1](#) lists the resistivity and density of common conducting materials. It can be seen for

aluminum, the  $\frac{1}{\rho_c \rho_m}$  factor is the highest  $\sim 1.31 \times 10^4 \text{ m}^2 / (\Omega \cdot \text{kg})$ , which is about twice that of the copper.

The last term is the volume ratio between the conductor and the effective mass. For moving conductor type topologies (Type A and Type C), this term is fixed to the ratio of the effective mass to the mass. In the Type A topology, this factor is generally smaller than in the Type C topology. This is because that the additional compliance element adds to the effective mass of a Type A device, but for type C topology, the conductor itself is the compliance element, and the effective mass (volume) can be smaller than the total mass (volume) of the conductor. For example, in the clamped-clamped beam structure shown in [Figure 3-1\(c\)](#), this factor is  $\sim 1.22$  [80].

To give a rough estimation of achievable coupling strength, assuming that a Type C device with aluminum conductor operating within a magnetic field provided by a 2 T Halbach cylinder, and that  $\frac{Q}{2\pi f_n}$  equals to 1 s, the resulting coupling strength is about  $6.3 \times 10^5$ . With such coupling strength value for both sides, the resulting maximum efficiency is estimated to be almost 99%. Even with a very conservative assumption with 0.5 T field, resulting with a coupling strength of  $4 \times 10^4$ , a maximum efficiency of 95.6% can still be achieved.

This estimation indicates that a highly efficiency ET is possible through design optimization. The factors of exceptional importance are the magnetic flux density and the mechanical properties. The reason for the former is due to the quadratic relationship between the coupling strength the magnetic flux density. For the latter, the variation of

the  $\frac{Q}{2\pi f_n}$  can be drastic: from  $\sim 1$  s in the [Chapter 4](#)'s macroscale prototype to  $\sim 1$  ms in the [Chapter 5](#)'s microscale prototype.

From the above analysis, the only size-scale-sensitive factor of the coupling strength is the term  $\frac{Q}{2\pi f_n}$ , where the natural frequency is inversely proportional to the square of the length scale:

$$f_n \propto \sqrt{\frac{k}{m}} \propto \sqrt{\frac{1/l}{l^3}} = \frac{1}{l^2}. \quad (3-40)$$

However, the scaling law of the quality factor is generally unknown. Very few published work can be found that systematically investigate the problem. A most comprehensive work by Emboden *et al.* [81] performed a series of measurements on different sized diamond oscillators in the MHz range. The work estimated that the quality factor is inversely proportional to  $l^3$  to  $l^5$ . If this were true,  $\frac{Q}{2\pi f_n}$  would scale favorably for microscale device.

### 3.4.2. Limit of Power Density

The estimation of power density is somewhat complicated, due to the four possible power-bounding scenarios (see [Section 3.3.2.3](#)). However, it is reasonable to make a hypothesis that at the absolute maximum power capacity condition, all four limits are met at the same time, so that no design margin is “wasted”. A validation of this hypothesis will be attempted later. It is stated here as a reason for randomly choosing any of the four limiting cases as the starting point and expecting that the resulting conclusions would converge. For convenience, the last one (secondary current limited case) is chosen here, and the absolute power capacity is then written as

$$P_{out\max} = \frac{I_{2\max}^2 R_{L\max}}{2}, \quad (3-41)$$

where

$$R_{L\max} = \frac{K_2}{I_{2\max}} \min \left\{ 2\pi f_n X_{\max}, \frac{F_{\max}}{b}, \frac{V_s - R_1 I_{1\max}}{K_1} \right\} - R_2. \quad (3-42)$$

Equations (3-41) and (3-42) imply that when the absolute maximum load power is reached, the secondary conductor current limit, as well as at least one of the other three limits are reached. Specifically, one of the other three limiting factors determines the maximum possible velocity (the terms inside the bracket), which determines the maximum voltage on the secondary side.

It needs to be noted that as long as one of the first three cases applies to the ET, the optimum load resistance that gives the maximum power is equal to the secondary conductor resistance. Using this condition

$$R_{L\max} = \frac{K_2}{I_{2\max}} \min \left\{ 2\pi f_n X_{\max}, \frac{F_{\max}}{b}, \frac{V_s - R_1 I_{1\max}}{K_1} \right\} - R_2 = R_2. \quad (3-43)$$

or

$$R_{L\max} = R_2 = \frac{K_2}{2I_{2\max}} \min \left\{ 2\pi f_n X_{\max}, \frac{F_{\max}}{b}, \frac{V_s - R_1 I_{1\max}}{K_1} \right\}, \quad (3-44)$$

and

$$P_{out\max} = \frac{I_{2\max}^2 R_{L\max}}{2} = \frac{I_{2\max} K_2}{4} \min \left\{ 2\pi f_n X_{\max}, \frac{F_{\max}}{b}, \frac{V_s - R_1 I_{1\max}}{K_1} \right\}. \quad (3-45)$$

Therefore, the maximum load power is determined by the product of the maximum secondary current, the secondary transduction coefficient, and the velocity. The product of the first two can be rewritten as

$$\frac{I_{2\max} K_2}{4} = \frac{J_{2\max} A_2 B_{\text{eff}} l_2}{4}, \quad (3-46)$$

where  $J_{2\max}$  is the maximum current density of the secondary conductor,  $A_2$  and  $l_2$  are the area and length of the secondary conductor, respectively. It can be seen that this term is limited by the maximum current density and volume of the secondary conductor, and the effective flux density.

To find the limit of the velocity, note that the second term in the bracket can be rewritten as,

$$\frac{F_{\max}}{b} = \frac{F_{\max} Q}{2\pi f_n m}. \quad (3-47)$$

It can be seen that the first and the second terms are contradicting in response of the frequency. For example, if the minimum of the three is the first term, the first term can be increased by increasing the natural frequency. However, increasing the natural frequency decreases the second term. At some point, the second term will be equal to the first term. Beyond this point, the second term will become the minimum. Therefore, the minimum of the first two terms is maximized at the intersection point when

$$2\pi f_n X_{\max} = \frac{F_{\max} Q}{2\pi f_n m} = \sqrt{\frac{F_{\max} X_{\max} Q}{m}}. \quad (3-48)$$

Note that the third term does not play an important role, because it can be increased by increasing the source voltage, with does not contradict with the other two terms.

Physically, the maximum velocity is reached when the device is designed such that the maximum force and maximum displacement are reached at the same time. Therefore, the maximum power is given by

$$P_{out\ max} = \frac{J_{2\ max} A_2 B_{eff} l_2}{4} \sqrt{\frac{F_{\max} X_{\max} Q}{m}}. \quad (3-49)$$

In order to calculate the maximum power density of the ET, assume that the ET structure is shown in [Figure 3-6](#). In this structure, the Type C topology is assumed, where the conductors and the mechanical resonator are formed by a clamped-clamped beam made with copper (because the maximum current density of copper is better known), and the magnetic field is created by a square Halbach cylinder with inner width of  $a_i$  and outer width of  $a_o$ , and length of  $l$ . The magnets used in the Halbach cylinder are NdFeB grade N50 (remanent flux density  $B_r=1.45$  T). In this case, the effective flux density is approximately given by [79]

$$B_{eff} = B_r \ln \frac{a_o}{a_i}. \quad (3-50)$$

Further assume that the beam is as long and as wide as the cylinder, and the maximum force allows a displacement amplitude that is about to touch the beam with the inner wall of the cylinder:

$$l_1 = l_2 = l, A_1 = A_2 = \frac{a_i t}{2}, X_{\max} = \frac{a_i - t}{2}. \quad (3-51)$$

where  $l_1$ ,  $l_2$ ,  $A_1$  and  $A_2$  are the length and cross section area of the two conductors, and  $t$  is the thickness of the whole beam (consisting of two conductors). The maximum current density of copper ranges from  $10^7$  A/m<sup>2</sup> for macroscale devices [82] to  $10^{10}$  A/m<sup>2</sup> for microscale devices [83]. The maximum applicable force on the beam is given by

$$F_{\max} = 2T_{\max} t a_i, \quad (3-52)$$

where  $T_{\max}$  is the shear strength of copper ( $\sim 1.7 \times 10^8$  Pa). The maximum power density can be calculated as

$$\begin{aligned}
S_{\max} &= \frac{J_{2\max} B_r t a_i \ln\left(\frac{a_o}{a_i}\right) l}{8 a_o^2 l} \sqrt{\frac{T_{\max} t a_i (a_i - t) Q}{0.41 \rho_c a_i t l}} \\
&= \frac{J_{2\max} B_r}{5.12} \sqrt{\frac{T_{\max} Q}{\rho_c}} \frac{t a_i \ln\left(\frac{a_o}{a_i}\right)}{a_o^2} \sqrt{\frac{a_i - t}{l}}.
\end{aligned} \tag{3-53}$$

From (3-53), assuming that the quality factor is on the order of 10, the maximum power density of ET is estimated to be on the order of  $10^8$  to  $10^{10}$  W/m<sup>3</sup>, or 100 to 10,000 W/cm<sup>3</sup>. Equation (3-53) shows no dependence of the ET power density on the physical scale. However, since the maximum current density and quality factor are known to scale favorably with decreased size, the actual power density may also scale favorably to decreased size. It needs to be noted that the analysis assumes that the skin effect and proximity effect can be ignored due to the sufficiently thin conductor and sufficiently low operating frequency. Nevertheless, the potentially feasible power density limits are least quite attractive compared to the theoretical maximum PT power densities of 330 W/cm<sup>3</sup>. More comparisons of ET with EMT and PT will be presented in the next section.

### 3.5. Comparison of Electrodynamic Transformers with Other Transformer Technologies

In this section, the function and performance of the ET are compared with the EMT and the PT through the use of LEM. The comparison is based on qualitative analysis and literature reviews. Comparison with the EMT will be first performed, followed by the comparison with the PT.

#### 3.5.1. Comparison with Electromagnetic Transformer

The equivalent circuit model of EMT is well known. As shown in [Figure 3-7\(a\)](#), the LEM of the EMT is similar to that of the inductively coupled coils described in [Section](#)

2.5.1. The only difference is that an equivalent core loss resistance exists in cored EMTs. The LEM of EMT agrees with the canonical circuit model as shown in [Figure 3-7\(b\)](#). Note that the EMT discussed here is assumed to operate at frequency much lower than the ferromagnetic resonant frequency (usually >10 MHz), so that the parasitic capacitances are ignored. For simplicity, it is also assumed that the core loss resistance is a linear resistance, which is not actually true since the core loss is frequency dependent. However, for qualitative analysis at lower frequency, the error from this assumption is not substantial.

The open-circuit voltage gain frequency response of the EMT modeled by [Figure 3-7\(b\)](#) is given by

$$\frac{V_{out}}{V_s} = \frac{N_2}{N_1} \frac{L_M R_c s}{L_1 L_M s^2 + (L_M R_1 + L_1 R_c + L_M R_c) s + R_1 R_c}. \quad (3-54)$$

Like the ET, the EMT is a second-order bandpass system. However, due to the practical design parameters, the EMT behaves very differently from ET. In a well-designed EMT, the total impedance magnitude of the leakage inductances ( $L_{L1}$  and  $L_{L2}$ ) and the coil resistances ( $R_1$  and  $R_2$ ) (collectively the “series impedance”) should be much smaller than the impedance magnitude of the magnetizing branch ( $L_M$  and  $R_c$ ) (collectively the “shunt impedance”) over a wide range of frequency:

$$R_{1,2} + L_{L1,L2} \omega \ll \frac{R_c L_M \omega}{R_c + L_M \omega} < \min \{R_c, L_M \omega\}. \quad (3-55)$$

Under these idealized conditions, the first order term in the denominator of (3-54) becomes much larger than the other denominator terms within a wide range of frequency. Therefore, within the frequency range where (3-55) holds, (3-54) becomes

$$\frac{V_{out}}{V_s} = \frac{N_2}{N_1} \frac{L_M R_c}{L_M R_1 + L_1 R_c + L_M R_c} \approx \frac{N_2}{N_1}. \quad (3-56)$$

As a consequence, the EMT generally has a large flat band with voltage gain close to  $N_1/N_2$ . Although the flat band is very wide, the voltage will decrease if the operating frequency is too low or too high. When the frequency is too low, the last term in the denominator of (3-54) dominates; when the frequency is too high, the first term in the denominator dominates. In both cases, the voltage gain approaches zero.

The efficiency and output power of the EMT are also maximized within its flat band. When the operating frequency is too low, the power loss is dominated by the conductive loss in the coil resistance. When the frequency is too high, the power loss is dominated by the core loss. Also, as the frequency increases, the increase in the core loss may become more significant.

It is well known that macroscale EMTs are highly efficient devices with efficiency generally over 95% when operating within the flat band frequency range. However, for the reasons stated in [Section 1.2](#), the miniaturization of EMTs is challenging due to the material limitations. As the dimensions of the EMT reduces, the magnetizing inductance reduces more rapidly than the coil resistance. This situation is worsened by the magnetic quality of microfabricated core materials, whose permeability is generally smaller than bulk core materials. With a relatively smaller magnetizing inductance, higher frequency is required to achieve sufficient magnetizing reactance, so that adequate proportion of voltage drop occurs on the magnetizing branch ( $R_c // L_M$ ). However, the higher operating frequency increases core loss and decreases the skin depth in the coils, which results in decreased  $R_c$  and increased  $R_1$  and  $R_2$ . As a result, both core loss and copper loss will increase. Many microscale power transformers use

air-core for easy fabrication and zero core loss. However, without the help of the core permeability, even higher frequency is required to establish the magnetizing reactance, which further reduces the skin depth and increases the copper loss. In short, EMT's fundamentally do not scale very favorably to small dimensions.

The power density of EMTs is limited by the maximum current density in the coils and the saturation flux density in the core. For microscale devices, the maximum current density limits are usually less restrictive, due to the increased ratio of the surface area and the heat-generating volume. In microscale transformers, the core saturation is usually the power limiting factor. The power density in the magnetic core is equal to the product of its energy density and the operating frequency. However, as the operating frequency increases, more heat dissipation is generated due to the increased core loss and copper loss. This often sets an upper bound on current density and frequency, and therefore the magnetic energy density in the core. The maximum achievable power density is highly dependent on the device structure, rated voltage, operating frequency, etc.

Existing works on microfabricated EMTs are mostly scaled-down versions of conventional macroscale EMTs. Brunet *et al.* [84] reported an E-core microtransformer with electroplated Permalloy ( $\text{Ni}_{81}\text{Fe}_{19}$ ) as core material. The  $0.33 \text{ cm}^2$  transformer provides an output power of  $0.4 \text{ W}$  at 40% efficiency in a 2 MHz dc/dc converter. Sullivan *et al.* [85] improved the power density and efficiency of the microtransformer using laminated core to reduce eddy current loss.  $\text{SiO}_2$  was used as the insulation layer between ten Permalloy layers. An efficiency of 61% and surface power density of  $22.4 \text{ W/cm}^2$  was achieved in a 8 MHz dc/dc converter. O'Donnell *et al.* [86] investigated the

optimization of microtransformers, and further improved the efficiency to 78% and the power density to 28 W/cm<sup>2</sup>. More recent effort focused on the air-core transformers. However, most of these efforts are devoted to signal processing instead of power converting applications. This is partially due to the extremely high frequency required for air-core transformers. For example, Kim *et al.* [87] reported a CMOS compatible air-core transformer with maximum efficiency of 81% at 2.4 GHz. As one of the few studies on air-core transformer for power converters, Meyer *et al.* [88] reported a transformer with multi-layer electroplated copper on Pyrex substrate. The estimated maximum efficiency of the transformer is up to 78% at frequency down to 125 MHz. Note that power densities reported for microscale EMTs are typically reported as areal surface power densities. Since the devices are generally very thin (0.1-1 mm), the calculated volumetric power density can reach 1 kW/cm<sup>3</sup>. However, these low-profile devices are not generally stackable while still maintaining the high volume power density. This is because of the heat dissipation and magnetic field interference issues.

In summary, ET has a much narrower bandwidth than EMT, which provides frequency selectivity but on the other hand creates challenge on frequency control. The macroscale EMT is more efficient than ET, but at microscale, it is possible for ET to be more efficient than EMT. There is no easy way to directly compare power density between ET and EMT.

### **3.5.2. Comparison with Piezoelectric Transformer**

A well-accepted equivalent circuit model of the PT is shown in [Figure 3-8](#) [89]. This model is very similar to that of the ET. The differences are the input and output electrical domains and the electromechanical transduction. In a PT, the input and output shunt capacitances are typically too large to be ignored due to the nature of the piezoelectric

materials. Additionally, the interface between the electrical and mechanical domains is piezoelectric transduction, which is modeled with a transformer instead of a gyrator. The transformer ratios  $d_1$  and  $d_2$  are the proportionality constants with unit of V/N. More details of piezoelectric transduction can be found in [25, 28, 90-92].

The inherent input and output capacitors of the PT makes the voltage gain frequency response highly dependant on the load condition. The resonant frequency is known to shift as the load resistance changes [89]. The derivation is mathematically complicated, thus not shown here. Since the quality factor of the PT is typically high, it is typically desired for the PT to operate very close to the resonant frequency to achieve high output power and efficiency. Therefore, if the PT is operating with a load that is dynamically changing, a sophisticated frequency control circuit is needed to make sure the PT is excited at the optimum frequency.

Another consequence of the capacitive input and output impedance is the difficulties in driving and loading. Specifically, a typical PT requires at least tens of volts of input voltage to create measurable mechanical vibration. On the output side, load resistance is typically on the order of tens of kilo ohms, so that the output voltage does not drop too much. These characteristics create further challenge for the peripheral circuit design. On the contrary, since the input and output impedance of an ET is usually in the ohm range. As will be shown in the experimental demonstrations in [Chapters 4 and 5](#), driving voltage of several millivolts may be sufficient for significant mechanical vibration. The output port of an ET can usually drive loads of tens of ohms without significant voltage drop. Therefore, ET has relatively smaller impact on the external

circuit, although it needs to be admitted that the small input impedance requires the output impedance of the previous stage to be small, too.

Since the electrical and mechanical domains are interfaced with transformers instead of gyrators, the mechanical resonator appears to the source and the load as a series RLC network that is in series with the source and the load (as shown in [Figure 3-9\(a\)](#)). In the ET, the mechanical resonator appears as a parallel RLC network that is in shunt connection with the source and the load (as shown in [Figure 3-9\(b\)](#)). This creates difference in the voltage gain frequency response. Also, when the transformers are used as resonant tanks in a circuit, the types of resonant tank are different: the PT resembles a series resonant tank, while the ET resembles a parallel resonant tank.

In terms of efficiency, the absence of the conductive loss tends to increase the efficiency of the PT comparing to ET. The main loss mechanism in the PT is the mechanical damping. The dielectric loss is usually negligible compared to the mechanical loss [93]. Reported efficiencies of PTs are usually above 90% [94-97].

The power density of PTs is limited by the dielectric strength, mechanical strength, saturation electric charge density, etc. Flynn *et al.* [48] estimated that the theoretical maximum power density of a PT using material PZT-5H is about  $330 \text{ W/cm}^3$  or an areal density of  $16.5 \text{ W/cm}^2$  assuming 0.5 mm thickness.

In summary, both ET and PT are resonant type transformers with relatively high quality factors. The capacitive input and output impedances creates challenges in the design of peripheral circuits, which need to provide sufficiently high driving voltage, large load impedance, and frequency control capability. The resonators in ET and PT

are different in topology when used as electrical resonant tanks. While PT generally has higher efficiency than ET, the power density of ET may be higher than that of the PT.

Table 3-1. List of common conductive materials' resistivity and density

Material name	Resistivity $\rho_c$ ( $\Omega \cdot m$ )	Density $\rho_m$ ( $kg/m^3$ )	$\frac{1}{\rho_c \rho_m}$ ( $m^2 / (\Omega \cdot kg)$ )
Copper	$1.72 \times 10^{-8}$	$8.92 \times 10^3$	$6.52 \times 10^3$
Aluminum	$2.82 \times 10^{-8}$	$2.71 \times 10^3$	$1.31 \times 10^4$
Silver	$1.59 \times 10^{-8}$	$1.05 \times 10^4$	$5.99 \times 10^3$
Gold	$2.44 \times 10^{-8}$	$1.93 \times 10^4$	$2.12 \times 10^3$
Platinum	$1.06 \times 10^{-7}$	$2.14 \times 10^4$	$4.41 \times 10^2$

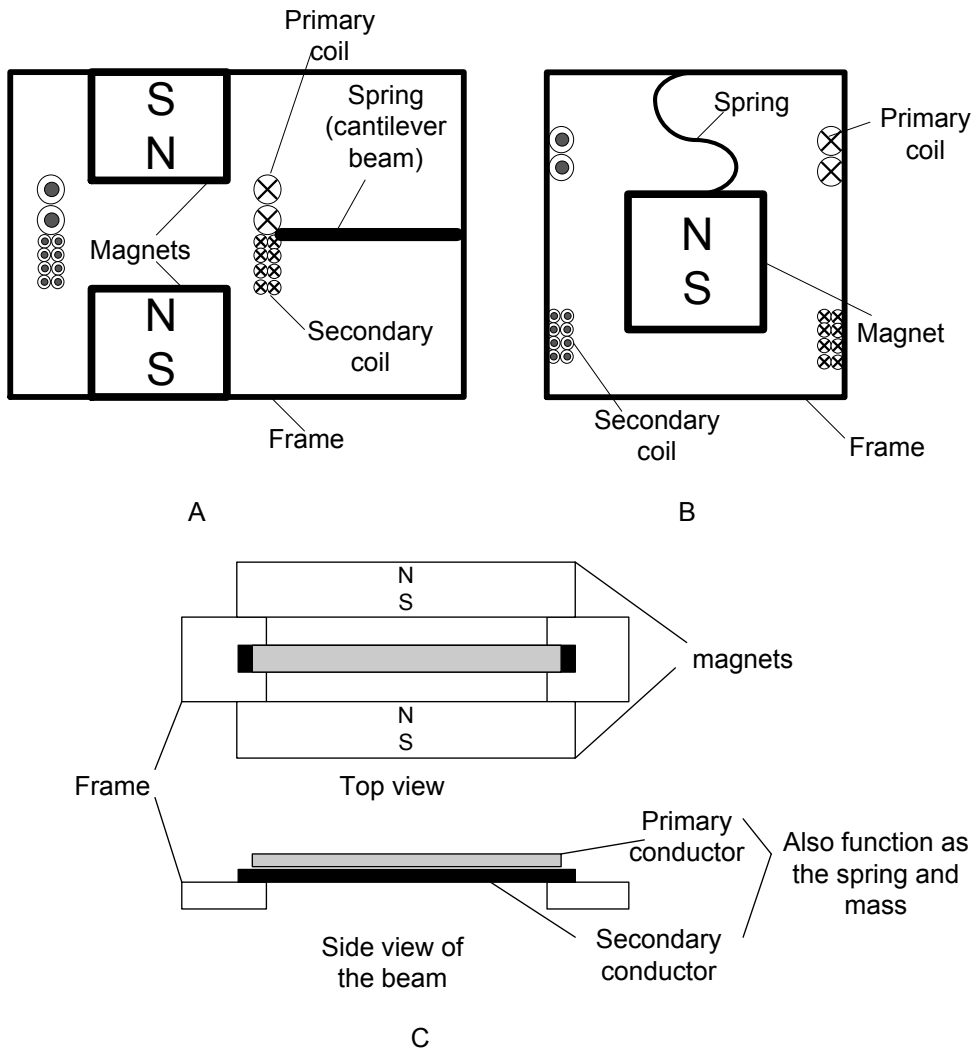


Figure 3-1. Three types of ET topologies. A) Type A: moving conductor with separate spring. B) Type B: moving magnet. C) Type C: moving conductor with conductor functioning as the spring.

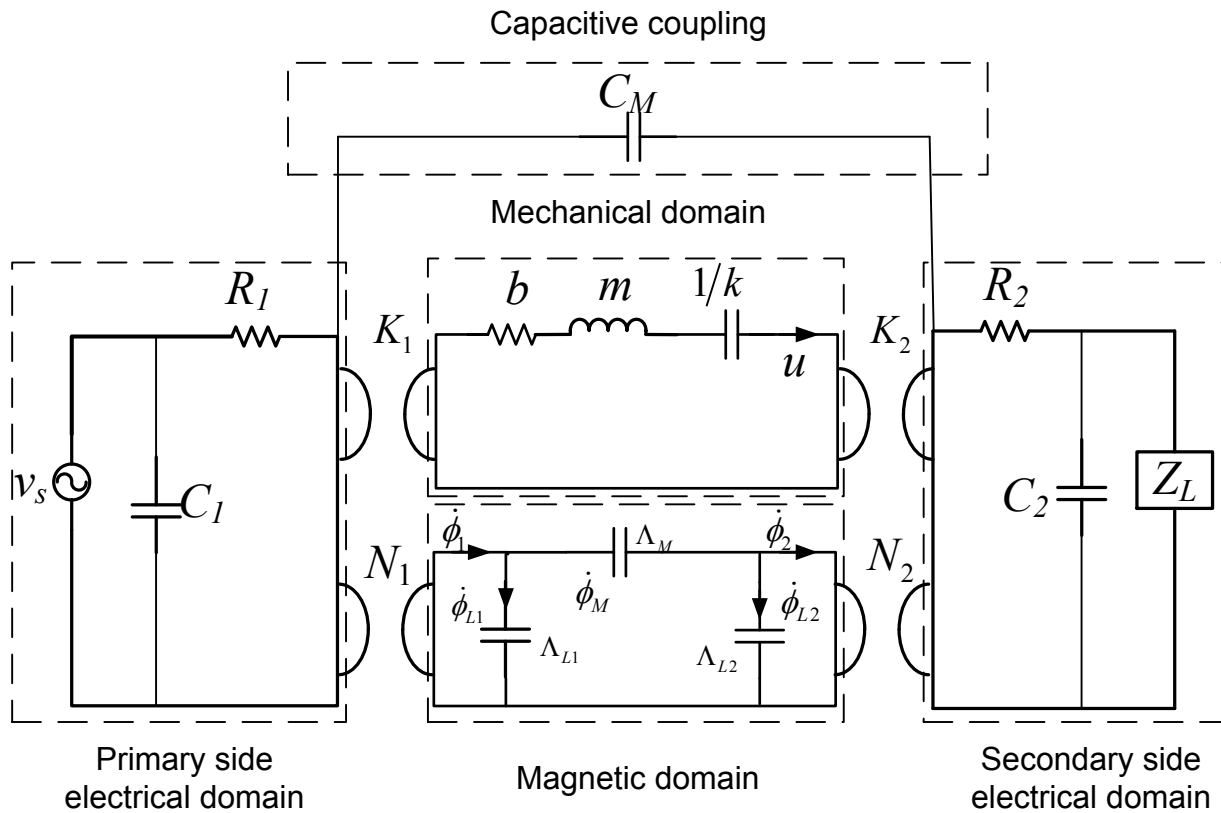


Figure 3-2. Complete lumped element model of an electrodynamic transformer.

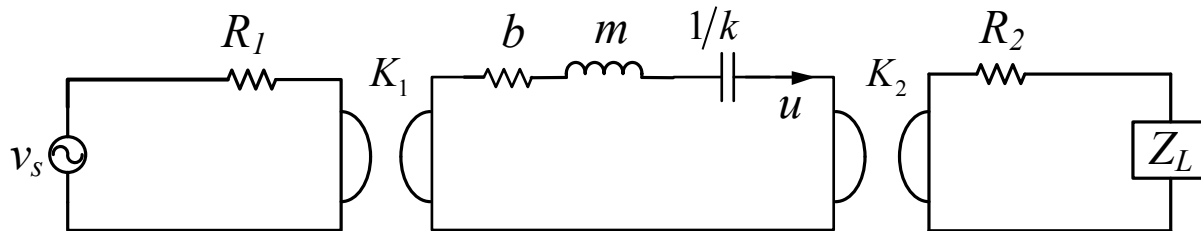


Figure 3-3. Simplified lumped element model of an electrodynamic transformer where only electrodynamic coupling is considered.

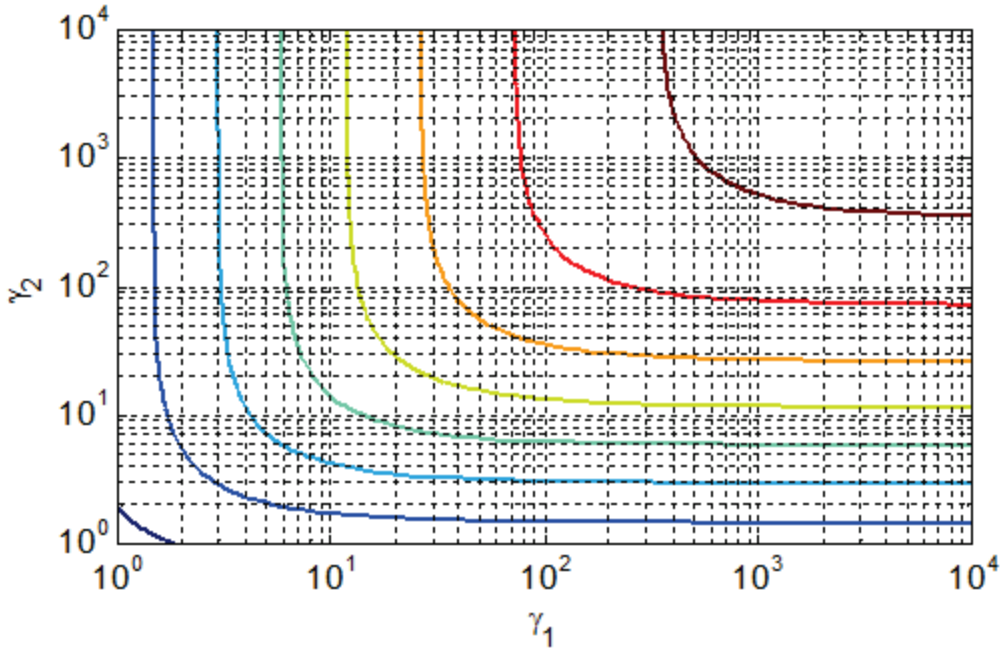


Figure 3-4. Contour plot of efficiency vss coupling strengths.

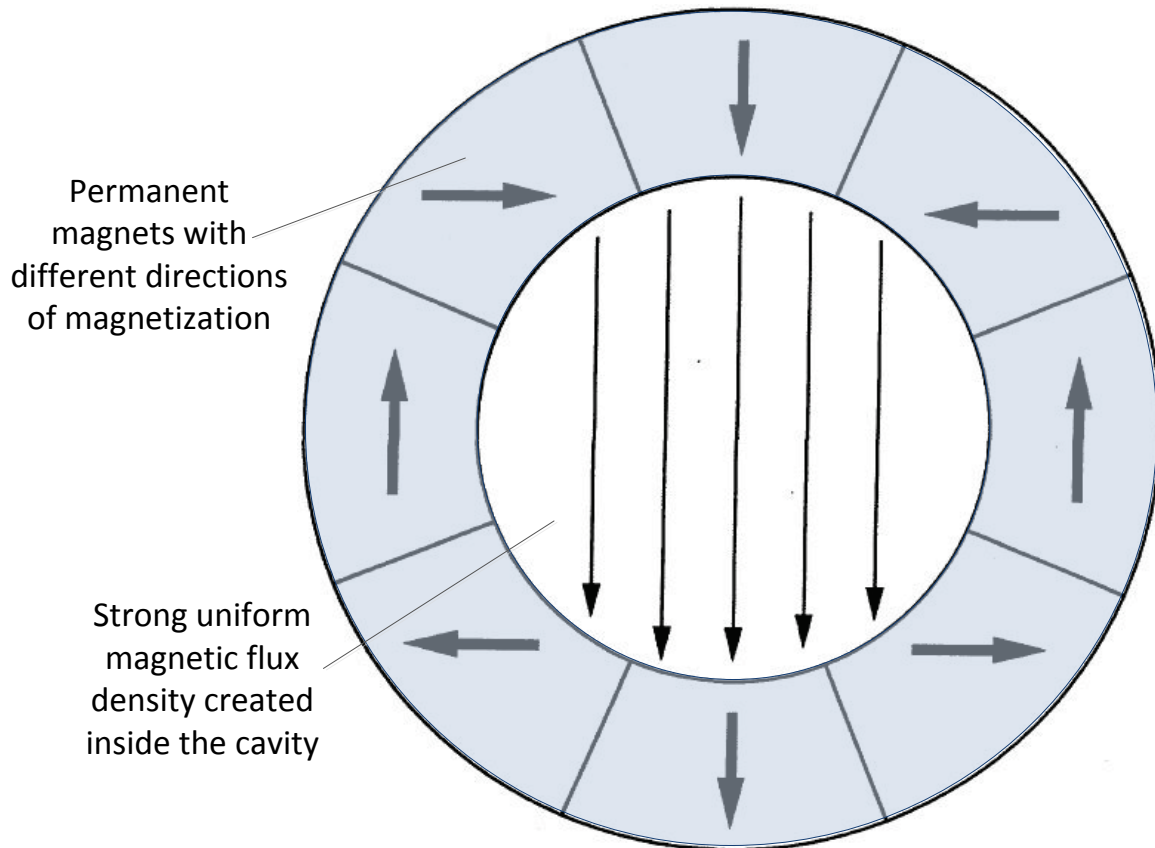


Figure 3-5. Strong uniform magnetic field created by a Halbach cylinder.

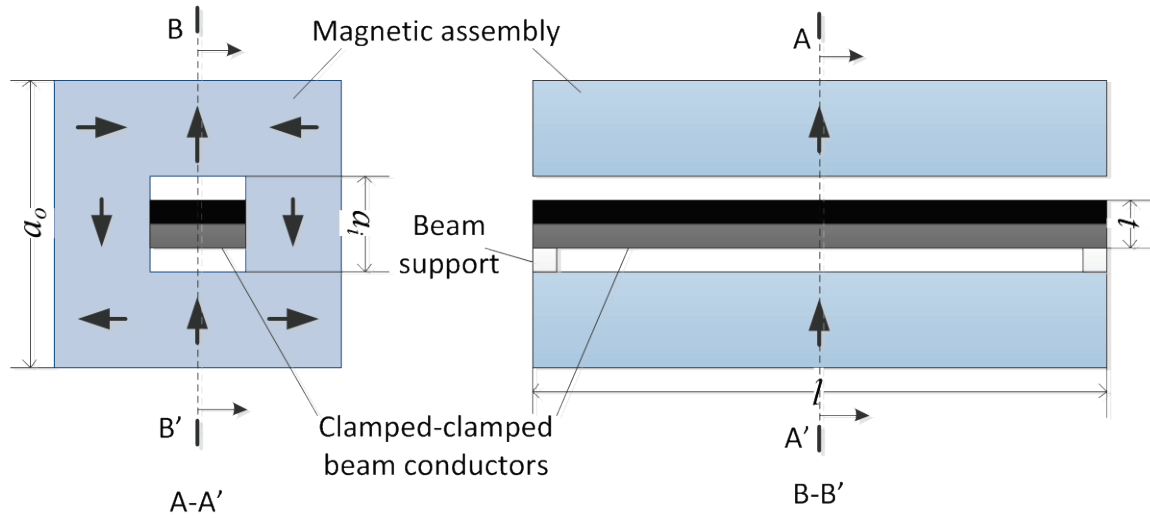


Figure 3-6. ET structure for power density estimation.

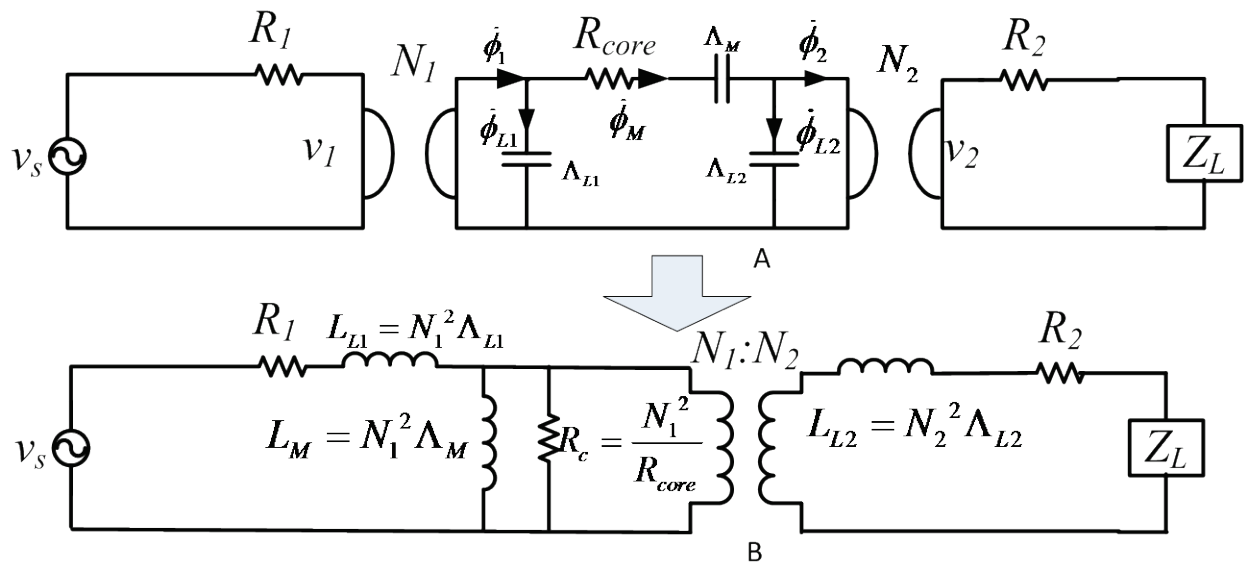


Figure 3-7. Lumped element model of an electromagnetic transformer. A) The model using magnetic permeances. B) The canonical circuit model using inductances.

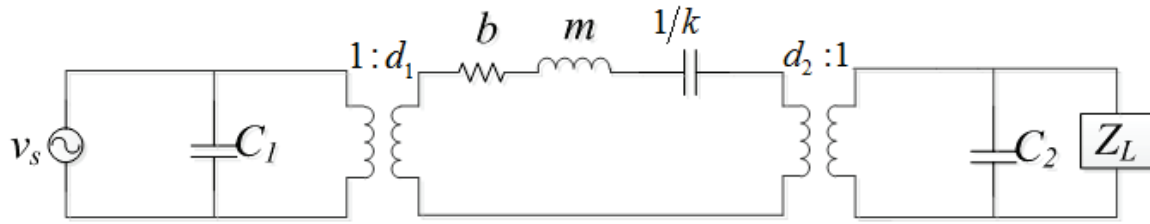
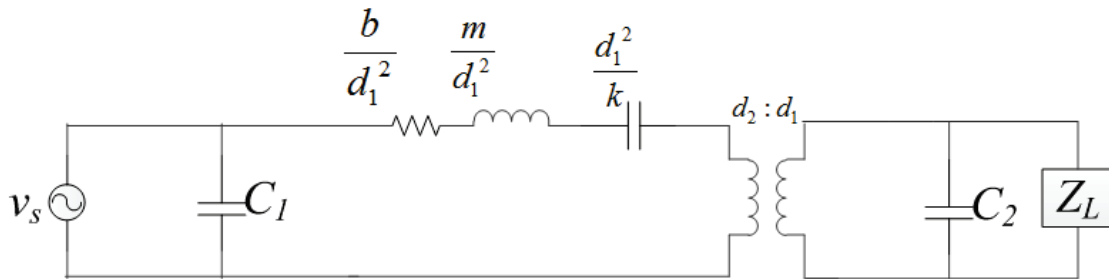
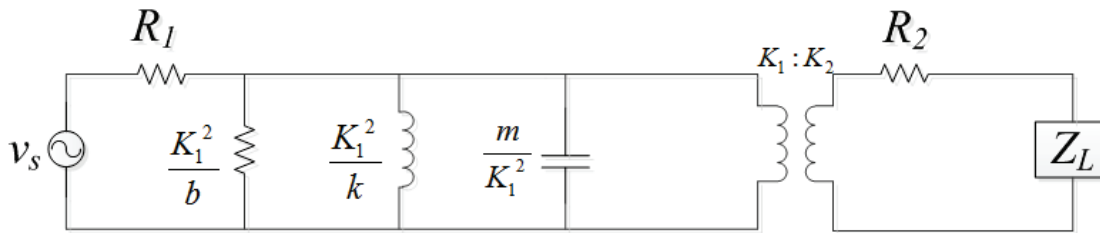


Figure 3-8. Lumped element model of a piezoelectric transformer.



A



B

Figure 3-9. Lumped element models with mechanical domain reflected to the primary electrical domain. A) The model for a piezoelectric transformer. B) The model for an electrodynamic transformer.

## CHAPTER 4 MACROSCALE DEVICE AND MODEL VALIDATION

In this chapter, the lumped element model of the ETs is validated through experiments on a macroscale prototype device. [Section 4.1](#) describes the construction of the prototype device. [Section 4.2](#) details the experimental procedures to extract the lumped parameters of the prototype device. In [Section 4.3](#), the extracted parameters are substituted into the lumped element model to predict the performance of the device, and the results are compared with the experimentally measured results. [Section 4.4](#) summarizes the work presented in this chapter.

### 4.1. Device Construction

The device constructed for model validation purpose is designed to behave as an ideal, linear, time-invariant system with parameters in the lumped element model easily measurable. A picture of the device is shown in [Figure 4-1](#). The device adopts the moving-coil configuration, shown in [Figure 1-1\(a\)](#). The magnetic field is created with two opposing disc-shaped NdFeB magnets (K&J Magnetics, Inc.; Grade N52; 1.11 cm diameter x 0.635 thickness). The primary and secondary coils are built using bondable wires (MWS Wire Industries, NEMA-MW29C) of AWG 25 and AWG 28, respectively. Both coils have the same dimensions (2.54 cm outer diameter, 1.5 cm inner diameter and 0.5 cm height), but differing number of turns (111 for the primary and 230 for the secondary coil). The coils are bonded together (via the bondable coating outside the insulation layer of the wires) and glued to a coil holder. The coil holder is attached to one end of a cantilever beam (aluminum beam with length 1.27 cm, width 1.27 cm, and thickness 0.1 cm). The other end of the cantilever beam is attached to the frame of the device. The overall size of the entire structure is 10 cm x 2.6 cm x 6.6 cm.

## 4.2. Parameter Extraction

In this section, the procedures of extracting the device parameters are presented.

The complete ET lumped model has 12 parameters. They are listed as follows.

- Two electrical parameters: the primary and secondary coil resistances ( $R_1$  and  $R_2$ ).
- Three mechanical parameters: the mass ( $m$ ) of the translator (the coils, the coil holder and equivalent moving mass of the cantilever beam), the stiffness of the cantilever beam ( $k$ ), and the damping coefficient ( $b$ ).
- Three magnetic parameters: leakage permeances of the primary and the secondary coil ( $\mathcal{A}_1, \mathcal{A}_2$ ), and the mutual permeance between the two coils ( $\mathcal{A}_M$ ).
- Two electromechanical transduction parameters: primary and secondary electrodynamic transduction coefficients ( $K_1$  and  $K_2$ ).
- Two electromagnetic transduction parameters: primary and secondary coil turns ( $N_1$  and  $N_2$ ). These two parameters are accurately known by counting the turns while winding the coils.

The extraction procedures of these parameters and results are introduced below.

Unless otherwise noted, all the uncertainty values are obtained using 95% confidence intervals.

### 4.2.1. Standalone Measurement of the Coils

Before assembling the magnets, the parameters of the coils ( $R_1, R_2, \mathcal{A}_1, \mathcal{A}_2$ , and  $\mathcal{A}_M$ ) are extracted. Since the magnets are not present, both primary and secondary electromechanical transduction coefficients are zero, and the system is reduced to a pair of inductively coupled coils. When the operating frequency is well below the self-resonant frequencies of the coils, the parasitic capacitances of the coils can be ignored. The equivalent model is the same as the example presented in [Section 2.5.1](#) (see [Figure 2-9](#)).

The coil parameters measured via these standalone tests are assumed to be the same with the permanent magnets present. The assumption of such usage is that the

addition of permanent magnets and mechanical structures does not alter the permeances. Although the NdFeB magnet has an effective permeability ( $\sim 1.05$ ) slightly higher than that of the air ( $\sim 1$ ), the change of permeances due to such small difference is believed to be negligible. Furthermore, it would be much more difficult to perform the coil measurements with the magnets mounted. The magnetic forces arising from the electrodynamic transduction would inevitably induce mechanical motion or strain, which may affect the measurement of the true permeances even more seriously.

The resistances of the coils are measured using a Keithley 2400 sourcemeter. Four-point measurements are used, which is especially important considering the small resistance values. The measured resistances of the primary and the secondary coil are  $0.72 \Omega$  and  $2.96 \Omega$ , respectively. Using the information in the sourcemeter's datasheet, the percentage uncertainties of the measurement are estimated to be 2% and 0.5 %, respectively.

As has been discussed in [Section 2.5.1](#), while the permeance model of the inductively coupled coils provides better physical insight, the canonical equivalent circuit model based on leakage and magnetizing inductances is more convenient for parameter extraction. Therefore, the canonical circuit model is used to extract the effective inductance values, and the permeance values are derived from the inductance values and the number of coil turns. The procedure of extracting the three inductance values is detailed in the following.

First, the impedance of each individual coil is measured (in isolation from the ET construction) using Agilent 4294A Impedance Analyzer with Agilent 16047A test fixture. With the frequency sweeping from 40 Hz to 10 MHz (201 total data points sampled

logarithmically, input signal set to 0.5 Vrms), the equivalent series resistance and inductance of each coil are measured and plotted in [Figure 4-2](#) and [Figure 4-3](#).

It can be seen that both coils have a self-resonant frequency of about 1.5 MHz. From 40 Hz to 10 kHz, the equivalent resistance and inductance values are very consistent, which means that the series R-L model depicts the behavior of the coils accurately within 40 Hz to 10 kHz. Throughout this frequency range, the average equivalent self-inductances of the primary and the secondary coils are 196  $\mu\text{H}$  ( $\pm 0.46\%$ ) and 834  $\mu\text{H}$  ( $\pm 0.48\%$ ), respectively. Note that the uncertainty bound of the self-inductances are obtained via Monte Carlo method. Specifically, 100 inductance vs. frequency (between 40 Hz to 10 kHz) curves are randomly generated according to the uncertainty chart of inductance measurement on the equipment.<sup>1</sup> Each of these curves is fitted with a horizontal line. The 95% boundary is calculated for the intercepts of the fitting results.

From the LEM of the inductively coupled coils shown in [Figure 2-9](#), the self-inductance of the primary coil can be expressed as the total inductance appears to the primary port with the secondary port open:

$$L_1 = L_{L1} + L_M. \quad (4-1)$$

Similarly, the self-inductance of the secondary coil can be calculated as the total inductance appears to the secondary port when the primary port is open:

$$L_2 = L_{L2} + \frac{N_2^2}{N_1^2} L_M. \quad (4-2)$$

---

<sup>1</sup> The uncertainty chart of the Agilent 4294A impedance analyzer is available at <http://cp.literature.agilent.com/litweb/pdf/5968-3809E.pdf> (accessed on November 5, 2011)

In order to solve for  $L_{L1}$ ,  $L_{L2}$  and  $L_M$ , another equation is needed. This is obtained by measuring the voltage transfer characteristic. The measurement is performed using a Stanford Research Systems SR785 Network Signal Analyzer. The signal analyzer operates at the swept sine mode, generating a  $0.1 V_{pk}$  sinusoidal waveform with frequency sweeping from 10 Hz to 10 kHz. The waveform is supplied to the primary coil, and the ratio between the actual voltage on the primary coil and the open-circuit voltage on the secondary coil is measured versus the frequency. The frequency response is plotted in [Figure 4-4](#).

The theoretical open circuit voltage gain based on the equivalent circuit model is given by

$$\frac{V_{oc}}{V_{in}} = \frac{N_2}{N_1} \frac{2\pi f L_M}{2\pi f (L_{L1} + L_M) + R_1}. \quad (4-3)$$

Fitting the measured voltage gain to the theoretical equation, and with previous measurement of the term  $(L_{L1} + L_M)$ ,  $L_M$  is estimated to be  $113 \mu\text{H}$  ( $\pm 1.6\%$ ). From [Figure 4-4](#), the theoretical equation agrees moderately ( $R^2=0.974$ ) with the measured data. Larger discrepancy occurs for frequency higher than 100 Hz. Since the ET will be operating at the mechanical natural frequency, which is later measured to be around 34 Hz, this discrepancy does affect the parameter estimation at the operating frequency.

Solving (4-1) and (4-2) using the estimated  $L_M$  value,  $L_{L1}$  and  $L_{L2}$  are found to be  $83 \mu\text{H}$  ( $\pm 2.4\%$ ) and  $350 \mu\text{H}$  ( $\pm 2.5\%$ ), respectively. By using (2-39), the values of  $A_1$ ,  $A_2$ , and  $A_M$  are estimated to be  $6.7 \text{ nWb/A}$  ( $\pm 2.4\%$ ),  $6.6 \text{ nWb/A}$  ( $\pm 2.5\%$ ) and  $9.2 \text{ nWb/A}$  ( $\pm 1.6\%$ ), respectively. As expected from the symmetric of the magnetic flux path, the leakage permeances for the primary and the secondary coils are almost the same. In addition, since the coils are glued together and their diameter is greater than the

thickness, it is reasonable that the mutual permeance is greater than the leakage permeances.

#### **4.2.2. Extraction of the Mechanical and Electromechanical Parameters**

After the standalone measurement of the coils, the magnets are mounted on the frame, and the complete device is characterized to extract the five other model parameters ( $m$ ,  $k$ ,  $b$ ,  $K_1$  and  $K_2$ ).

First, the spring constant is extracted. When the ET operates, the driving force is provided by the electrodynamic force associated with the current in the primary coil, which is assumed to be an evenly distributed load across the volume of the coil. Since the coil is relatively rigid, the distributed load is equivalent to a point load acting at the center of the coil. Therefore, in the spring constant measurement, a known external load is applied to the coils, and the resulting displacement is measured. Specifically, two equal forces are applied to the outer edge of the two through-holes on the coil holder, and the displacement is measured at one of the edges. In this setup, each end of a soft and smooth cord (an AWG 36 magnetic wire) is tied to one of the two through holes on the coil holder. A hook is hung on the cord and allowed to slide smoothly along it. Different numbers of metal rings are applied on the hook to create a variable point load on the coil holder. Since the friction between the cord and the hook is made very small and the cord is very soft, the force is nearly equally distributed on both anchor points at the coil holder. With the number of metal rings hanging at the hook increasing from zero to seven and then decreasing back to zero, the center displacement of the coil is measured using a laser displacement sensor (Keyence LK G-32). The measured force vs. displacement is plotted in [Figure 4-5](#). A linear curve fitting determines that the spring constant is 1215 N/m ( $\pm 2.6\%$ ). The observed hysteresis is attributed to the static friction

between the hook and the cord that are used to attach the weights. Due to the uncertainty of the static friction, the actual force distribution between the two segments of the cord on each side of the hook can be different even when identical amount of weight is attached (during loading and unloading procedure). More accurate measurement can be performed by using a force gauge and a rigid testing stage.

The transduction coefficient extraction procedure is also performed along with the spring constant extraction procedure. Whenever the loading weight is changed, a dc current is supplied to one of the coils to create an electrodynamic force that counterbalances the load. By increasing the current amplitude, the displacement is forced back to zero, and the electrodynamic force resulting from the current is assumed equal to the gravitational force of the load. The transduction coefficient at the equilibrium position is given by the ratio of the gravity force and the current. The force vs. current for both coils is plotted in [Figure 4-6](#). A linear curve fitting shows that the primary transduction coefficient is 0.662 N/A ( $\pm 5.7\%$ ), and the secondary transduction coefficient is 1.614 N/A ( $\pm 1.5\%$ ).

The transduction coefficients measured using the method above are strictly only applicable when the coils are at the equilibrium position. Since the coils will be moving during the operation of the ET, it is interesting to see how much the transduction coefficients vary with position. To explore this effect separate experiments are conducted using increasing dc current amplitudes to force the deflection of the cantilever beam. By measuring the displacement with the laser displacement sensor, the spring force of the cantilever beam is calculated using the afore-measured spring constant. Since the electrodynamic force is equal and opposite to the spring force at

each steady-state position, the electrodynamic forces corresponding to each current values are obtained, and the transduction coefficients are calculated for each displacement value. The results are shown in [Figure 4-7](#). It can be seen that when the displacement is between -0.6 mm and 0.5 mm, the variations of the transduction coefficients for both the primary and the secondary coils are smaller than  $\pm 10\%$ . This experiment is useful, since later models assume that the transduction coefficients are fixed, i.e. do not change with the displacement of the beam.

Last, the mass and the damping coefficient are extracted from the time response of the free vibration. At the beginning of the experiment, a force is applied to the coils to establish an initial displacement. The force is generated by applying a dc current in one of the coils. Then the current flow is abruptly cut off by physically disconnecting the power supply electrical connections. This suddenly removes the force, leaving the translator free to vibrate due to the non-equilibrium initial condition. The time response of the translator displacement is sensed using the laser displacement sensor and recorded on an oscilloscope (Tektronix TDS5104B). An example time response curve is shown in [Figure 4-8](#).

The damped resonant frequency ( $f_d$ ) and the decay rate ( $\alpha$ ) can be directly obtained from the curve. The damped resonant frequency is given by the reciprocal of the time difference between the adjacent peaks. By using different pairs of peaks, ten values of  $f_d$  are obtained, giving an estimate of 34.3 Hz ( $\pm 1.6\%$ ). The decay rate is obtained by fitting the curve envelope (all the peaks) to an exponential function

$$d_p(t) = Ae^{-\alpha t}, \quad (4-4)$$

where  $d_p$  is the value of the peak displacement, and  $A$  is a proportionality constant. As shown in Figure 4-8, the estimated decay rate is  $3.048 \text{ s}^{-1}$  ( $\pm 2\%$ ). From the damped resonant frequency and the decay rate, the damping ratio ( $\zeta$ ) and the natural frequency ( $f_n$ ) can be calculated by

$$\zeta = \frac{\alpha}{2\pi f_n}, \quad (4-5)$$

and,

$$f_n = \frac{f_d}{\sqrt{1-\zeta^2}}. \quad (4-6)$$

The resulting values  $\zeta$  are and  $f_n$  are  $0.0141$  ( $\pm 2.6\%$ ) and  $34.3 \text{ Hz}$  ( $\pm 1.6\%$ ), respectively. The equivalent mass of the translator is then calculated using

$$m = \frac{k}{(2\pi f_n)^2} \quad (4-7)$$

to be  $0.0262 \text{ kg}$  ( $\pm 4.1\%$ ). The damping coefficient is calculated using

$$b = 2\zeta\sqrt{km} \quad (4-8)$$

to be  $0.159 \text{ N}\cdot\text{s/m}$  ( $\pm 3.6\%$ ).

A summary of the extracted parameters is listed in [Table 4-1](#). It needs to be noted that the mechanical natural frequency of the device ( $34.3 \text{ Hz}$ ) is lower than the measurement range of the impedance analyzer (minimum  $40 \text{ Hz}$ ). However, since the inductances of the coils are sufficiently consistent in the measured frequency range, it is believed that the estimated inductances are valid at the natural frequency.

### 4.3. Performance Prediction and Verification

In this section, the parameters values extracted in 4.2 are plugged into the LEM derived in 3.4 to predict the performance of the device. The purpose is to provide a

benchmark performance data to be compared with the actual performance data. Circuit simulations and experiments will be performed under several different source and load conditions in order to validate the model over varying performance conditions.

Specifically, the open-circuit voltage gain frequency response is simulated and measured with frequency-sweeping voltage source and  $1\text{ M}\Omega$  (representing the input impedance of the output voltage measurement equipment), and the output power and efficiency is simulated and measured with fixed-frequency voltage source (34.3 Hz) and a range of load resistances.

The equivalent circuit of the ET is simulated with circuit simulation software (Linear Technology Co., LTspice v4.11). A screen capture of the schematic is shown in [Figure 4-9](#). All the gyrators are implemented using pairs of current-controlled voltage sources (CCVS) that are controlled by the current through each other. The uncertainties of the circuit parameters are embedded in the SPICE model to perform Monte Carlo simulation. The Monte Carlo analysis is performed by perturbing the model parameters twenty times, generating twenty voltage frequency response curves. The composite superposition of these curves is shown in later data plots. Furthermore, in order to validate the analytical expressions derived in [Section 3.3.2](#) using the simplified model, a third plot is generated using (3-8), which is derived by assuming ignorable inductive coupling.

First, the system is simulated with a swept sine voltage input of  $0.1\text{ V}_{\text{pk}}$  (10 Hz to 10 kHz), and a load resistance of  $1\text{ M}\Omega$  (the actual load resistance when measuring the open-circuit voltage with oscilloscopes and signal analyzers). The experimental measurement is performed by measuring the transfer function of the ET using a signal

analyzer (Stanford Research Systems SR785). A  $0.1 V_{pk}$  swept sine input signal is provided to the primary coil by the source terminal, and the actual voltages on the primary and the secondary coils are measured with the first and the second channels of the same signal analyzer, respectively. The voltage gain and phase shift vs. frequency are analyzed.

The measured response and the simulation results are shown in [Figure 4-10](#). The curves generated by the full-model Monte Carlo simulation are so close to each other that they cannot be clearly distinguished as separate curves in the plot. This indicates that the parameter uncertainty incurred in the previous measurements does not contribute significantly to the discrepancy in the open-circuit voltage gain prediction. The predicted frequency response shows a resonant peak at between 33.5 Hz and 35.1 Hz with a gain from 5.2 dB to 5.8 dB (1.8 to 1.9 in linear scale), and an anti-resonant valley at 74.6 Hz with a gain of -53 dB (0.28 in linear scale). The measured response has similar trend as the simulation predicted, with a maximum gain of 4 dB (1.6 in linear scale) at 34.9 Hz, and a minimum gain of -50 dB (0.00312 in linear scale) at 80.3 Hz. In both cases, the anti-resonant behavior is due to the inductance of the primary coil (the secondary coil inductance does not affect the open-circuit measurement), which increases the system order from two to three. This is evident from the simulated response of the simplified model, where the anti-resonant behavior is not observed because inductance is ignored. Nevertheless, the simplified model provides reasonably accurate prediction of the result up to the resonant frequency (with a predicted gain of 5.7 dB or 1.93 at 33.5 Hz). The measured voltage gain is lower than the predicted value, which is later found to be the over-measured input voltage due to the parasitic

wiring resistance. Since the primary coil resistance is comparable to the resistance of the cable, any voltage drop on the cable has been accounted for as the input voltage. This could be resolved by using a separate cable for the measurement, rather than sharing the cable between sourcing and measurement. In the experimental results, two additional minor resonant peaks are noted between 60 Hz and 80 Hz that are not reflected in the LEM predicted response. These peaks may be attributed to torsional and lateral vibration modes.

Recall that in [Section 3.3.1](#), the simplified model is valid on when the frequency is much lower than the value given by (3-7), as repeated here

$$f \ll \frac{K_1 I_1 - K_2 I_2}{2\pi b} \min \left\{ \frac{K_1}{N_1 [N_1 I_1 \Lambda_{L1} + (N_1 I_1 - N_2 I_2) \Lambda_M]}, \frac{K_2}{N_2 [(N_1 I_1 - N_2 I_2) \Lambda_M - N_2 I_2 \Lambda_{L2}]} \right\}. \quad (4-9)$$

Since the secondary coil is open (with an actual load resistance of 1 MΩ due to the input impedance of the signal analyzer),  $I_2$  is close to zero, (4-9) can be rewritten as

$$\begin{aligned} f &\ll \frac{K_1 I_1}{2\pi b} \min \left\{ \frac{K_1}{N_1^2 I_1 (\Lambda_{L1} + \Lambda_M)}, \frac{K_2}{N_2 N_1 I_1 \Lambda_M} \right\} \\ &= \frac{K_1}{2\pi b} \min \left\{ \frac{K_1}{N_1^2 (\Lambda_{L1} + \Lambda_M)}, \frac{K_2}{N_2 N_1 \Lambda_M} \right\} \\ &= 2237 \text{ Hz} \end{aligned} \quad (4-10)$$

Since the first resonant frequency is only around 34 Hz, the simplified model provides accurate prediction up to the first resonance as expected.

Next, power and efficiency data are obtained both from simulation and experiments, and also compared with the analytical expression derived in (3-16) which assumes strong electrodynamic coupling as well as ignorable inductive coupling. With

the frequency fixed to 34.3 Hz, different load resistances are connected to the secondary coil. In the experiment, the input power is measured by calculating the time average product of the input voltage and the input current, where the input current is measured with a current probe (Tektronix TCP 312). The time-average power is automatically calculated by the oscilloscope (Tektronix TDS5104B). The output power is calculated by dividing the mean square output voltage by the load resistance. The efficiency is then obtained by calculating the ratio of the output power and input power.

The measured and predicted power efficiency and output power curves are shown in [Figure 4-11](#) and [Figure 4-12](#). Note that the uncertainty of the measurement results has been considered negligible compared to that of the predicted results, which comprises of multiple sources of error from the parameter extraction. In the measurement result, a maximum output power of 778  $\mu\text{W}$  is delivered to a 10  $\Omega$  load at an efficiency of 34.4%. About same efficiency is obtained at 20  $\Omega$  load resistance, while the output power is only 688  $\mu\text{W}$ . It can be seen that the LEM full model correctly predicts the optimum load resistance. However, the LEM predicts lower efficiency (26%-31%) than the actual measurement. The source of the error may be associated with some variation of the system parameters since the parameter extraction. However, as stated in [Section 3.3.2.1](#), the model that assumes strongly coupled transductions predicts higher efficiency than the full model and offsets the error. It is interesting that the prediction of the strongly coupled model matches the measurement much better, because the coupling strengths of the primary and the secondary transductions are only 3.8 and 5.5, respectively.

From an absolute performance perspective, a peak efficiency of 35% is much smaller than most EMTs and PTs. However, since the prototype is designed for model validation, where easy measurement of the lumped parameter was given the highest priority, there are many ways to improve the efficiency in future designs. For example, a better designed magnetic assembly with higher radial magnetic flux density can be achieved by using multiple hard and soft magnets to guide the flux lines. A more rigid frame material that provides better anchoring of the beam may be able to significantly reduce the mechanical damping coefficient. A larger conductor volume can be used to make better use of the space and to decrease the resistances. Since this dissertation is really focused on preliminary investigations of the ET, construction and realization of an optimized device has been left as a future work.

#### **4.4. Summary**

In this chapter, a macroscale ET prototype is constructed to validate the LEM. The LEM parameters have been extracted via a series of experiments, and plugged into the equivalent circuit model that is simulated with a circuit simulation tool. The model precisely predicted the general trend of the open-circuit voltage gain frequency response. A slightly lower voltage gain is achieved in the experiment due to the parasitic wiring resistance. The full LEM underestimates the power efficiency by 3%-8%, while the simplified LEM that ignores the magnetic domain and assumes strongly coupled electrodynamic transduction provides a more accurate estimation of the frequency.

Since the purpose of the prototype is to validate the device, a low efficiency of 35% does not represent the potentially achievable efficiency in an optimized device. Future works have been suggested that could potentially optimize the device

performance and achieve higher efficiency. However, detailed study of optimization is out of the scope of this preliminary study of ET.

Table 4-1. List of extracted parameters.

Parameter	Value
Primary coil resistance ( $R_1$ )	0.72 $\Omega$ ( $\pm 2\%$ )
Secondary coil resistance ( $R_2$ )	2.96 $\Omega$ ( $\pm 0.5\%$ )
Mass of the translator ( $m$ )	0.026 kg ( $\pm 4.1\%$ )
Spring constant ( $k$ )	1215 N/m ( $\pm 2.6\%$ )
Damping coefficient ( $b$ )	0.159 N*s/m ( $\pm 3.6\%$ )
Primary leakage permeance ( $A_1$ )	$6.7 \times 10^{-9}$ Wb/A ( $\pm 2.4\%$ )
Secondary leakage permeance ( $A_2$ )	$6.6 \times 10^{-9}$ Wb/A ( $\pm 2.5\%$ )
Mutual permeance ( $A_M$ )	$9.2 \times 10^{-9}$ Wb/A ( $\pm 1.6\%$ )
Primary transduction coefficient ( $K_1$ )	0.662 N/A ( $\pm 5.7\%$ )
Secondary transduction coefficient ( $K_2$ )	1.614 N/A ( $\pm 1.5\%$ )
Primary coil turns ( $N_1$ )	111
Secondary coil turns ( $N_2$ )	230

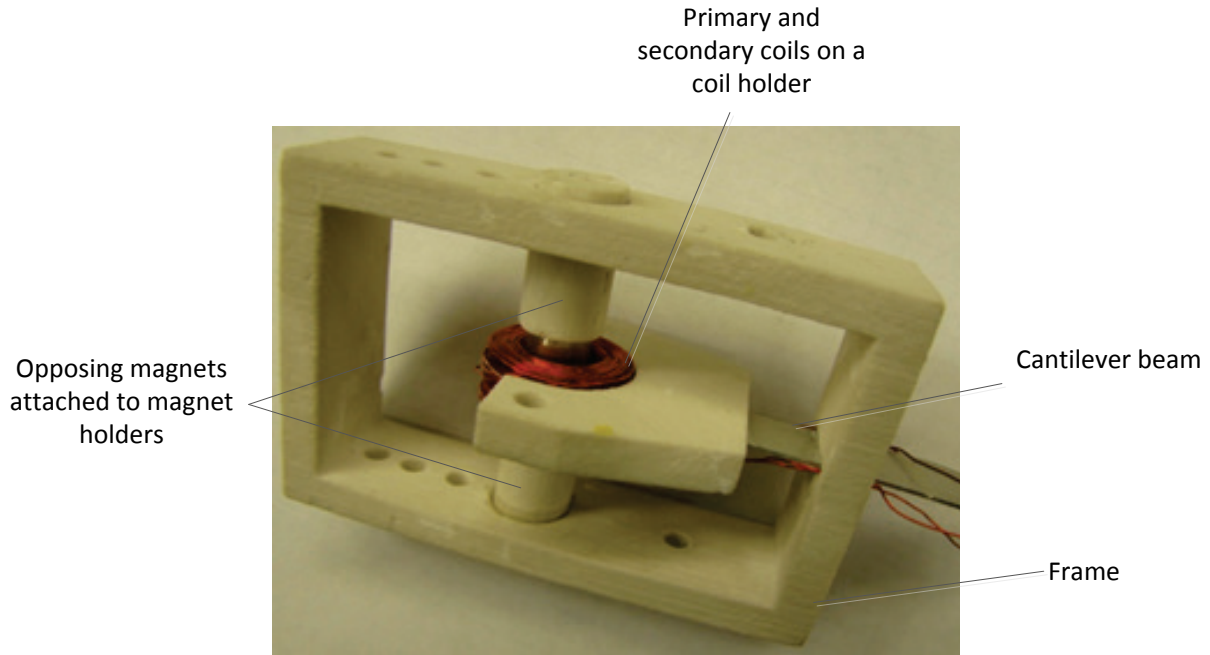


Figure 4-1. A picture of the macroscale prototype

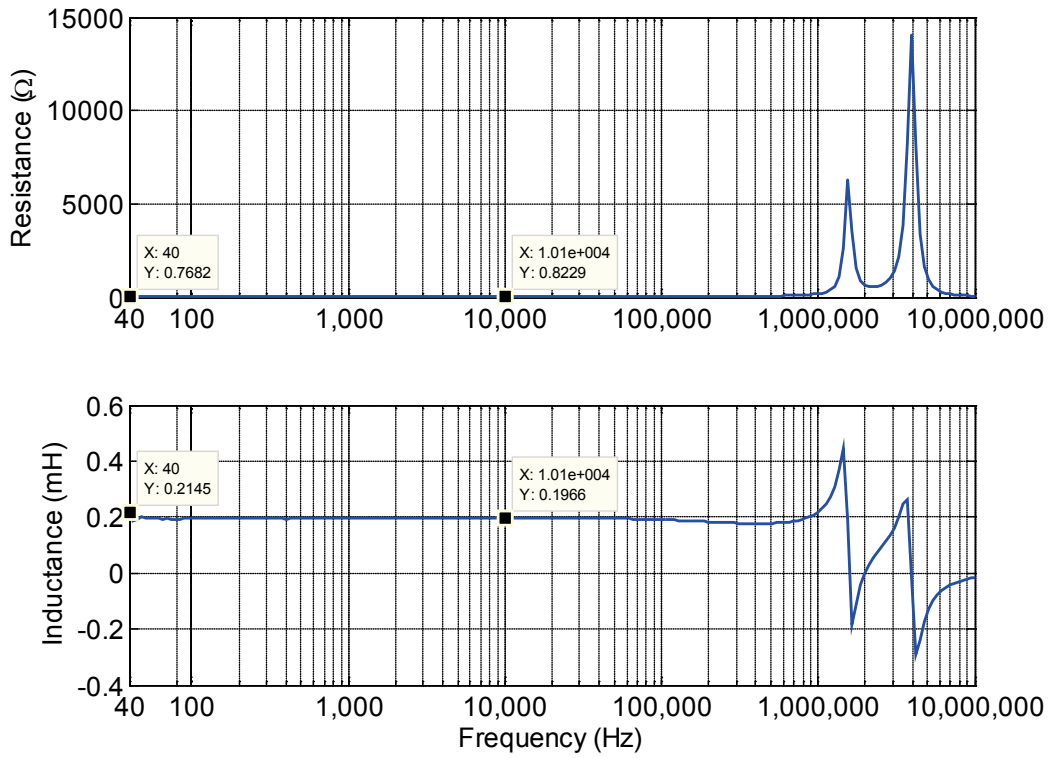


Figure 4-2. The series resistance and inductance of the primary coil

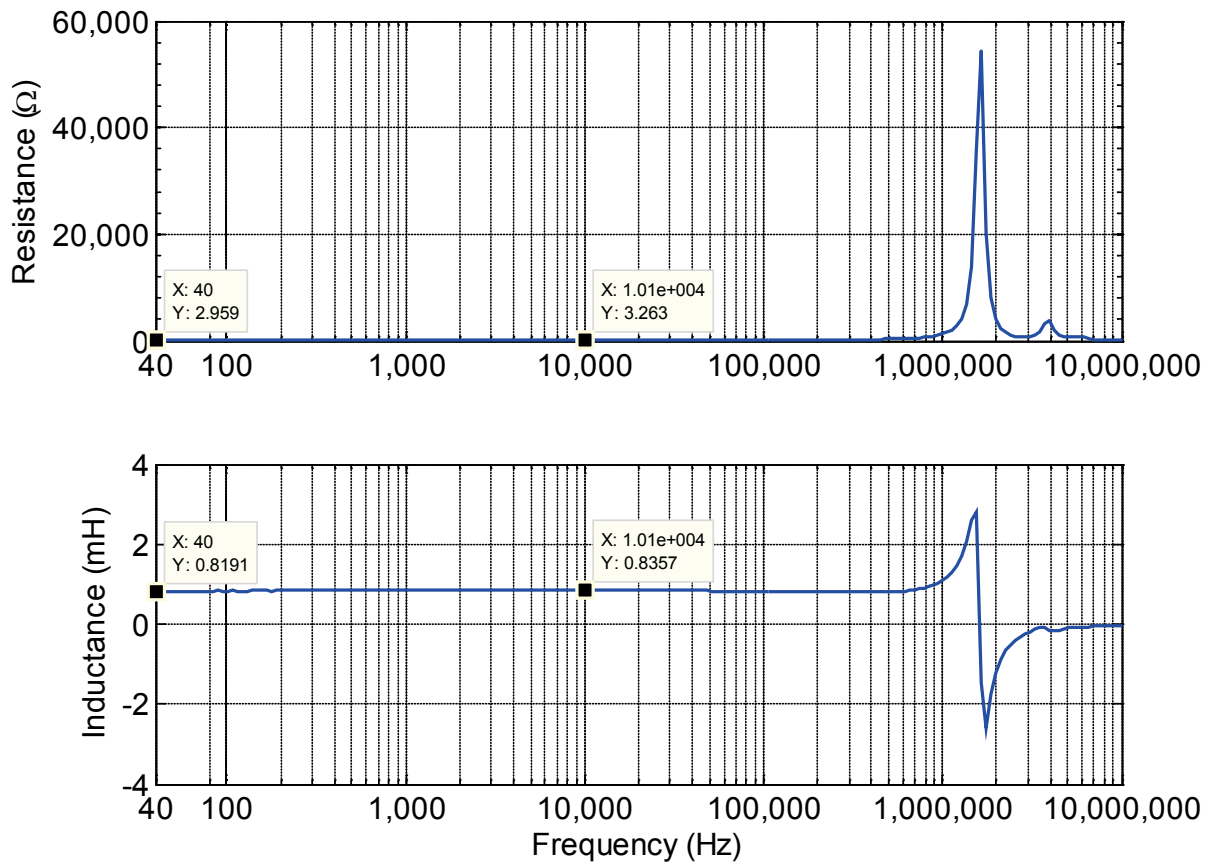


Figure 4-3. The series resistance and inductance of the secondary coil

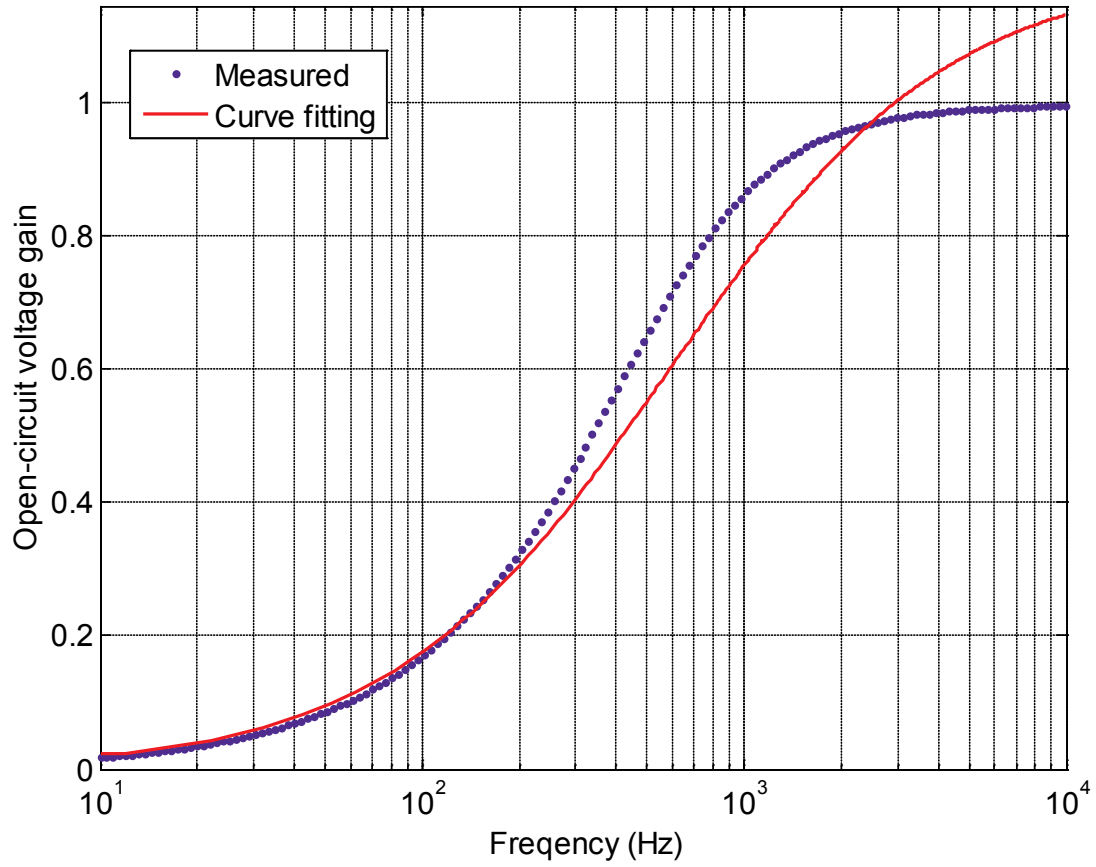


Figure 4-4. Curve fitting of the voltage gain frequency response.

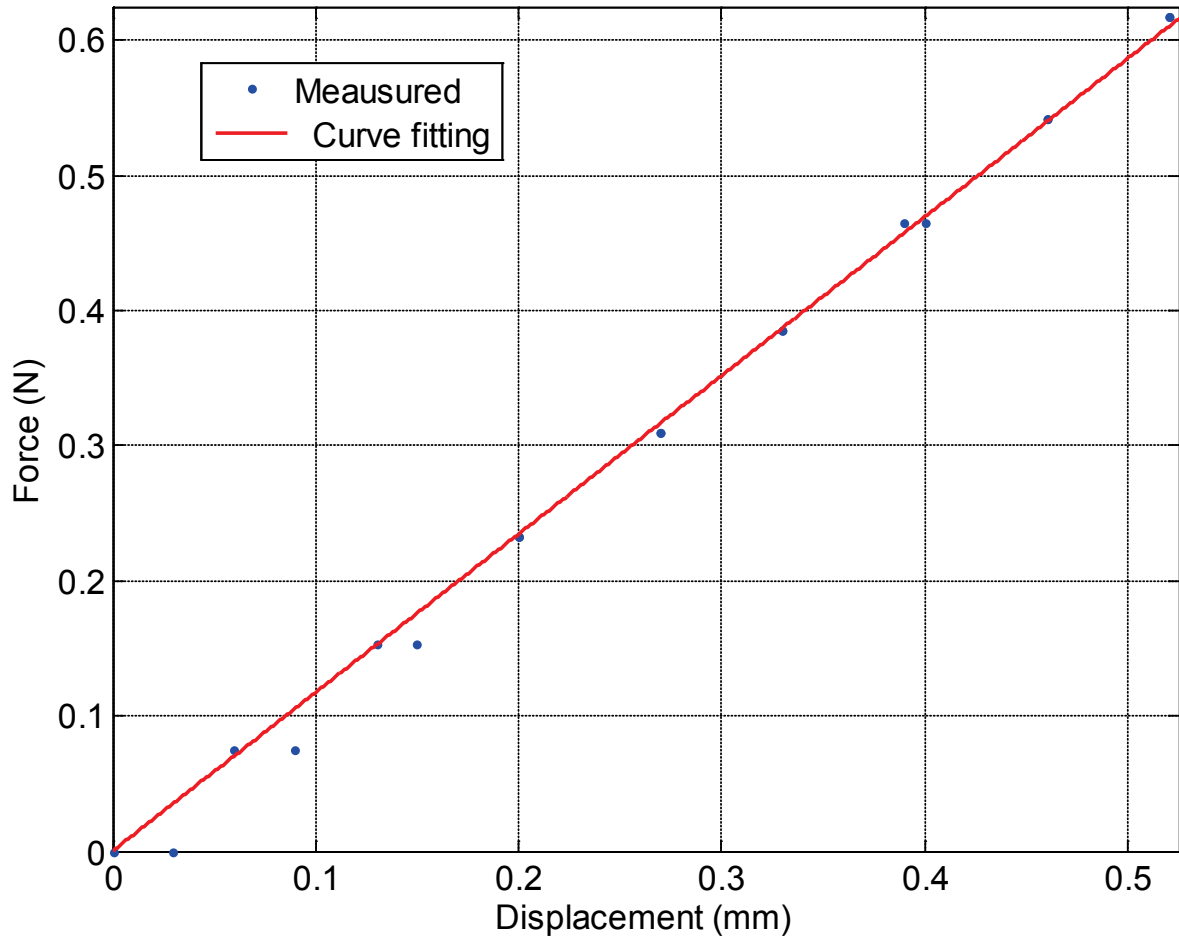


Figure 4-5. Force vs. displacement of the spring.

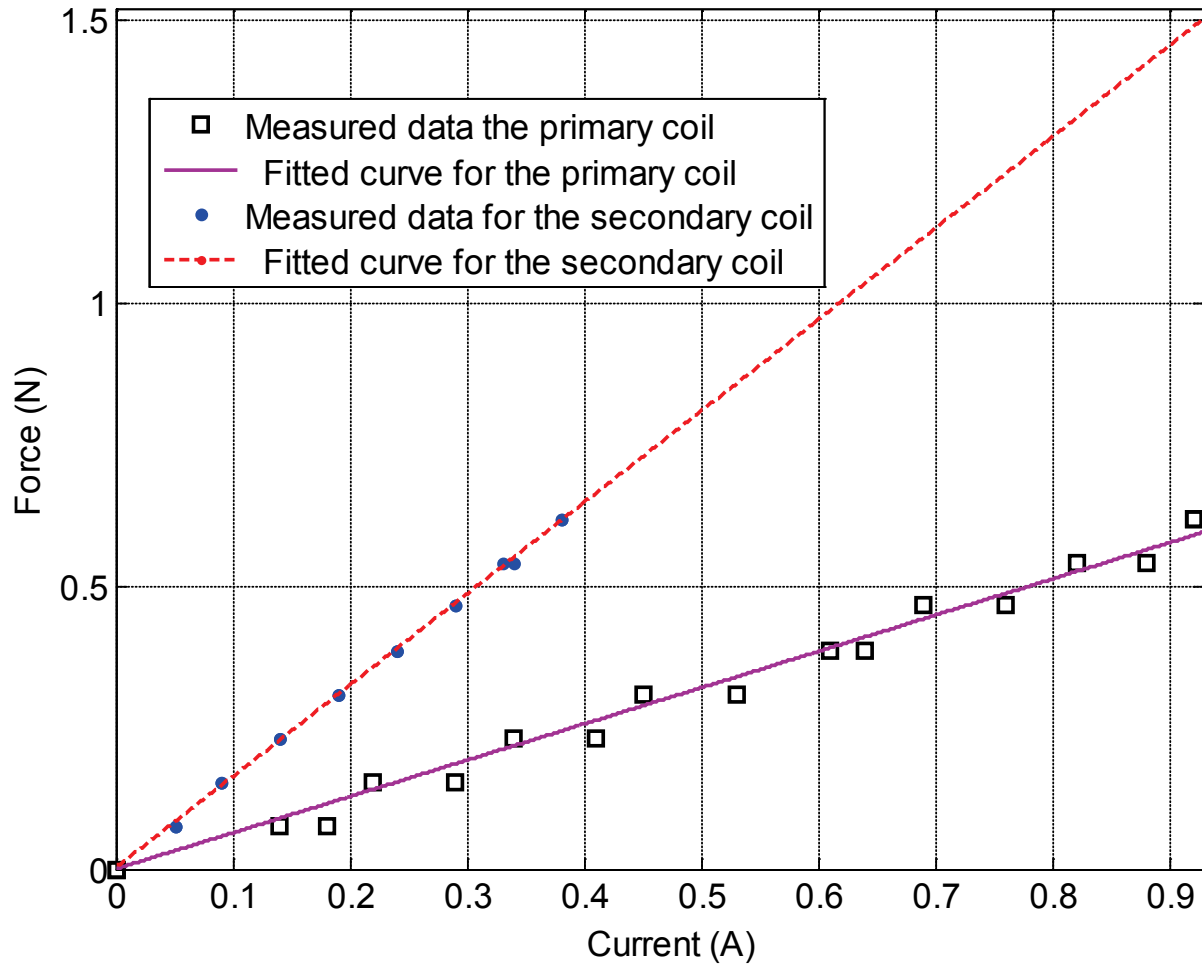


Figure 4-6. Force vs. current for the primary and secondary coils.

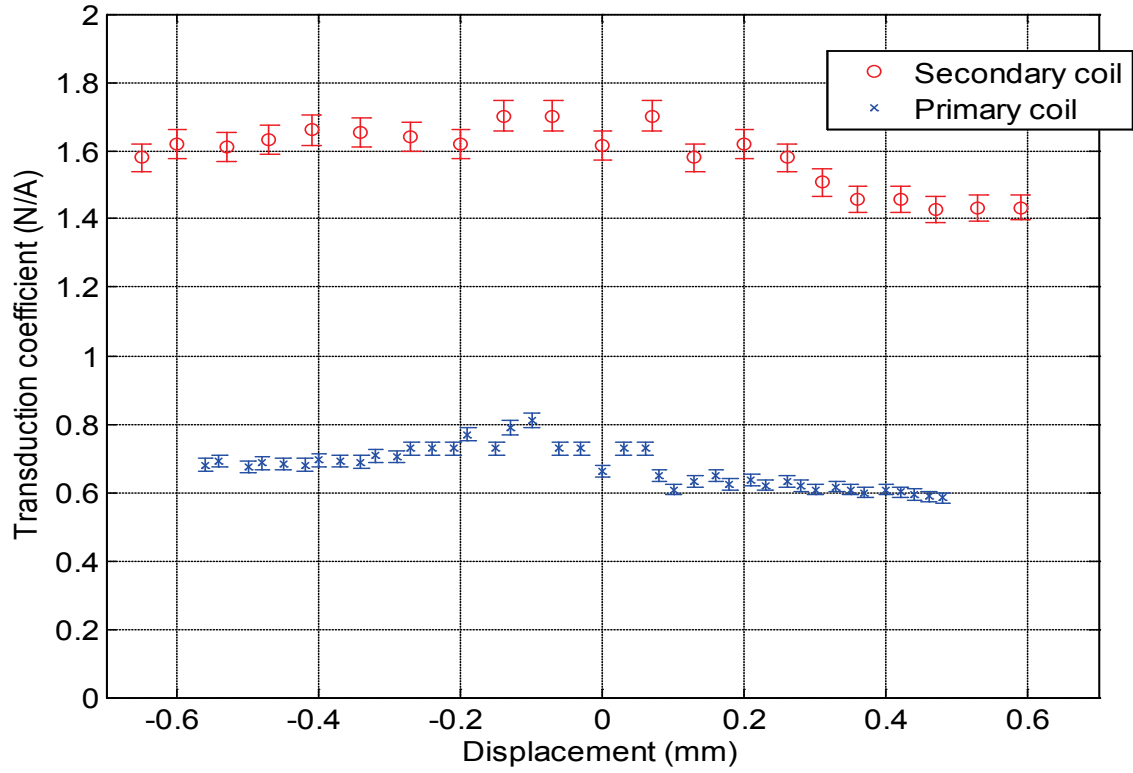


Figure 4-7. Transduction coefficient variation with displacement.

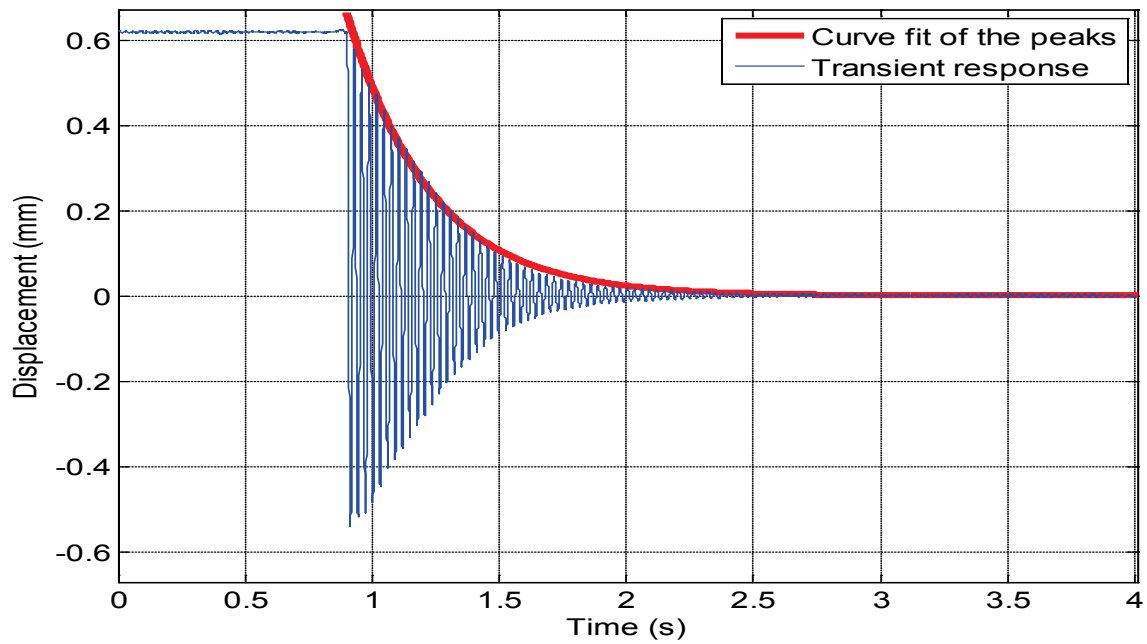


Figure 4-8. Transient response of the mechanical resonator.

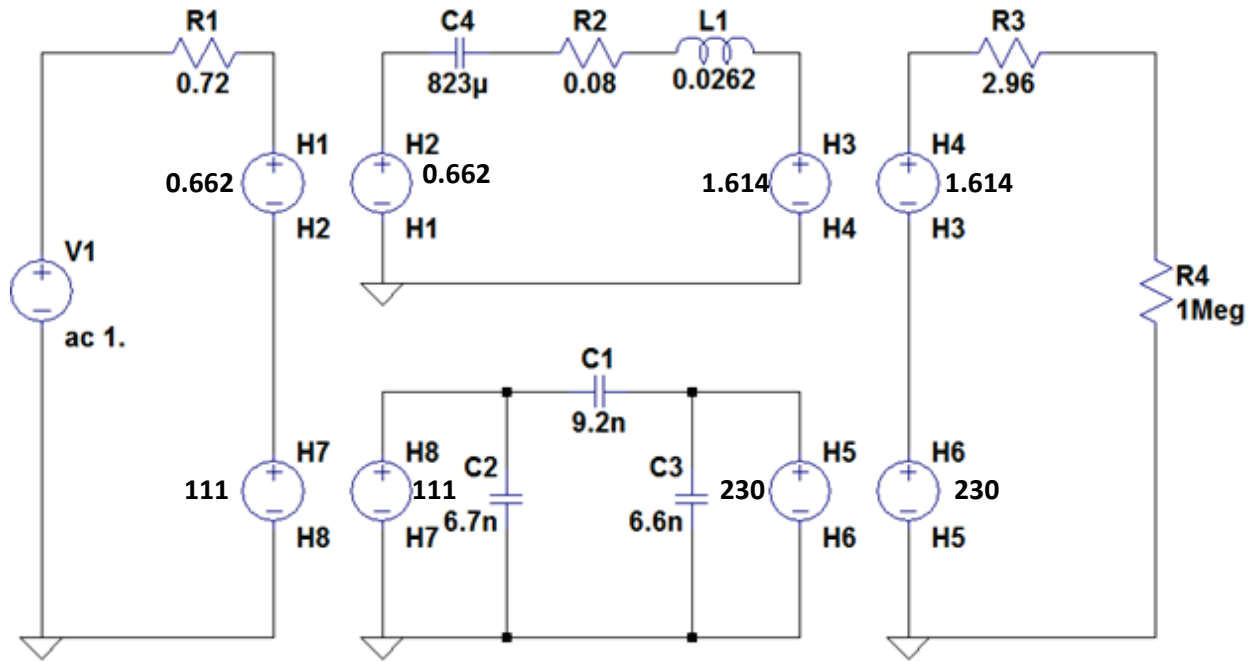


Figure 4-9. Circuit model simulated in LTSpice.

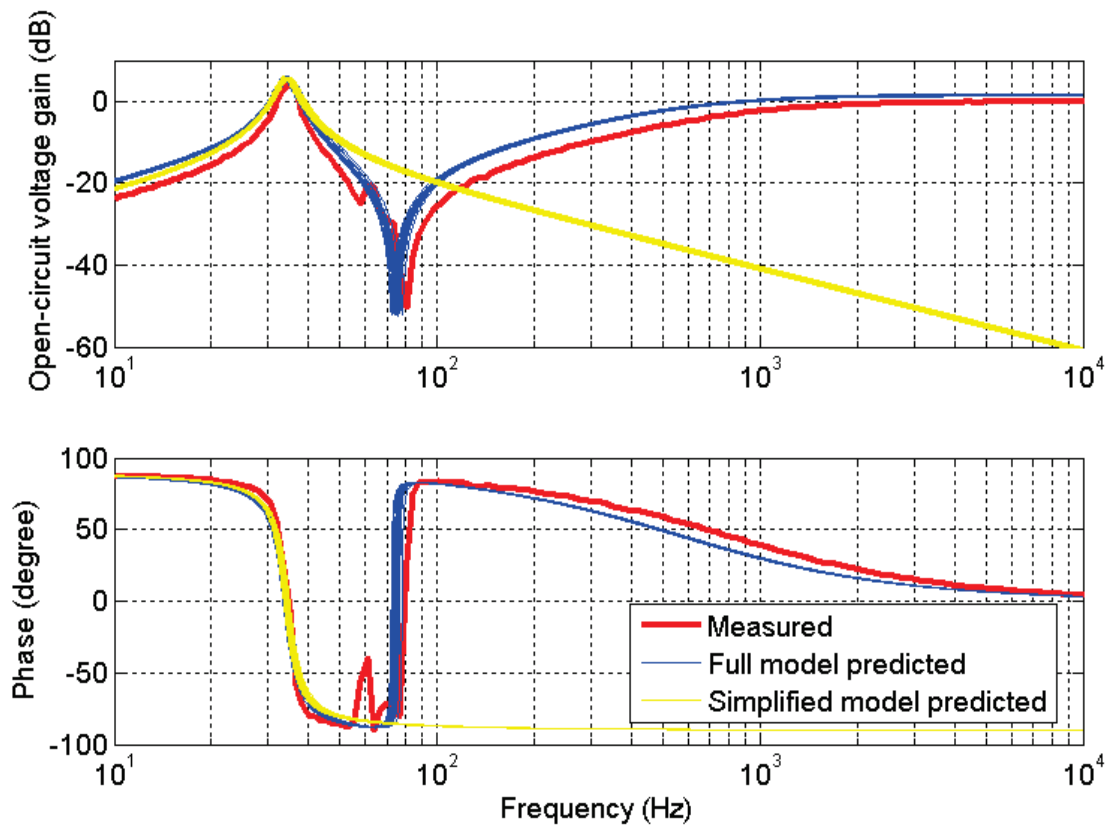


Figure 4-10. Measured and predicted open-circuit voltage gain frequency response.

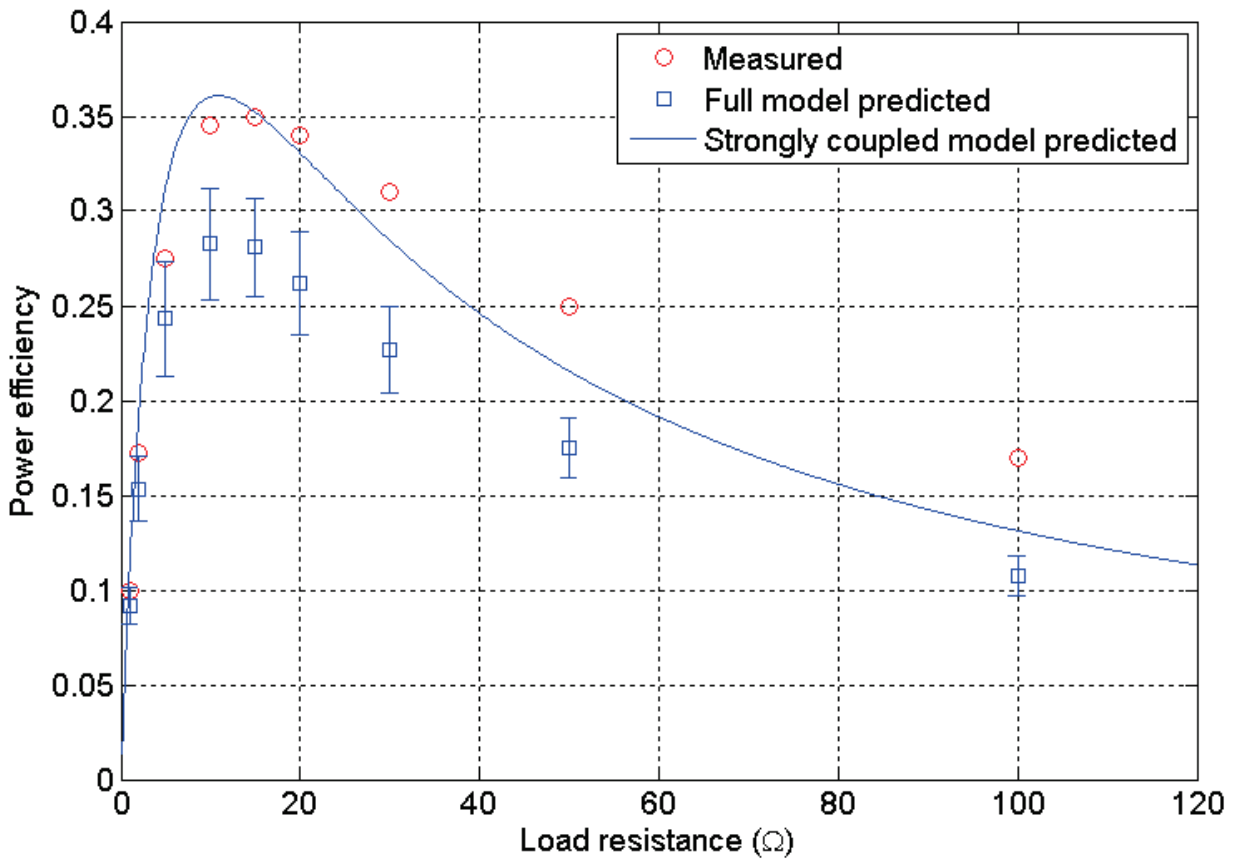


Figure 4-11. Measured and model predicted efficiency vs. load resistance.

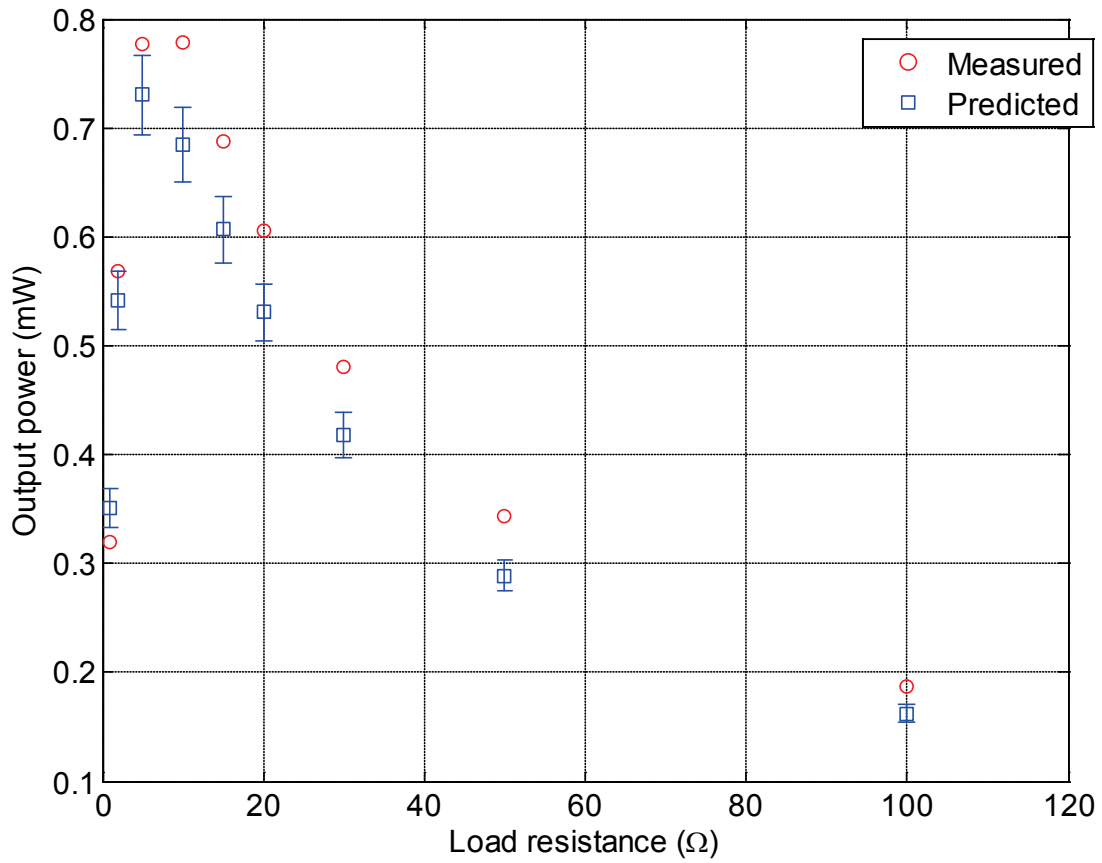


Figure 4-12. Measured and model predicted output power vs. load resistance.

## CHAPTER 5 MICROSCALE DEVICE AND EXAMPLE APPLICATION

The end goal of the proposed ET effort is motivated by the potential for fully integrated power converters with higher power density and efficiency. Owing to the substantially different behaviors of macroscale and microscale systems, a study of a microscale ET is warranted. This chapter presents a partially microfabricated ET using the Type C topology introduced in [Chapter 3](#). In this device, all except the magnetic assembly is microfabricated. The device design is first introduced, followed by the microfabrication process of the microscale components. Next, the experimental characterization of the device is presented. Then, an example application of the device is described. Last, a summary and outlook of the microscale ET is provided.

### 5.1. Device Design

As shown in [Figure 5-1](#), the device consists of an external macroscale magnetic assembly and a microscale clamped-clamped-beam structure that spans across an inner frame. The device employs a Type C architecture, where the beam serves as the moving element, the compliant element, and the electrical conductor. The device design is similar to what is presented in [98], where a microelectromechanical inductor is implemented.

The magnetic assembly comprises two NdFeB bar magnets (Grade N42 6.35 mm x 6.35 mm x 25.4 mm) magnetized in the transverse direction (along one of the short axes of the magnet). The magnets are arranged side by side with anti-parallel magnetization directions. The microfabricated clamped-clamped beam structure is mounted above the intersection along the length of the magnets. The magnets establish a transverse (in-plane) magnetic field acting on the clamped-clamped beam. As shown

in [Figure 5-2](#), the FEM simulated average transverse flux density within the conductor region is about 0.9 T.

The microscale clamped-clamped beam structure consists of two sandwiched copper beams ( $5700\ \mu\text{m} \times 300\ \mu\text{m} \times 5\ \mu\text{m}$  each) as the primary and the secondary conductors, and a layer of Parylene C polymer ( $1.5\ \mu\text{m}$  thick) in between to provide electrical insulation. The sandwiched beam structure sits on a silicon substrate (overall dimensions:  $7900\ \mu\text{m} \times 2500\ \mu\text{m} \times 500\ \mu\text{m}$ ), which acts as the frame. Except for the contact pads, the silicon underneath the beam is removed, thereby allowing the beam to move (out-of-plane).

The copper layers are overlapped everywhere except for the contact pads. To enable electrical contact to the lower conductor, the electrical contacts of the top copper layer are half the size of that of the bottom copper layer. The insulation material Parylene C is known to have low dielectric constant ( $\sim 3$ ), good dielectric strength ( $\sim 200\ \text{V}/\mu\text{m}$ ) [99], and suitable adhesion to copper. Also, since Parylene C's Young's Modulus is much smaller than that of copper (2.7 GPa vs. 110 GPa), its impact on the beam's mechanical response is small.

Either layer of the copper can be used as the primary conductor, because of their equal size the voltage gain is expected to be  $\sim 1$ . When the input current flows in one of the conductors, the electrodynamic force drives the sandwiched beam structure to bend in/out of the mounting surface. The movement of the beam induces an output voltage on the other conductor. Since the beam is fabricated on a  $500\ \mu\text{m}$  thick silicon substrate whose mass is sufficiently larger, the beam vibration is not expected to cause the substrate to move.

## 5.2. Device Fabrication

The microscale part is fabricated with the process flow shown in [Figure 5-3](#). There are four primary steps: forming the first copper conductor layer; forming the Parylene C insulation layer; forming the second copper conductor layer; releasing the sandwiched beams. The process uses standard single-side-polished, 100-mm-diameter, (100) silicon wafers.

The process begins by depositing titanium-copper-titanium seed layers on the front (polished) side of the wafer. The e-beam evaporated seed layers have thicknesses of 20 nm, 200 nm and 20 nm from top to down. The copper beam structures are then electroplated on these seed layers using photoresist molds. An electroplating mask is first patterned on the seed layers using 10  $\mu\text{m}$  thick photoresist AZ9260. Before electroplating copper, the top seed layer titanium is removed by dipping into 1:18 HF:H<sub>2</sub>O for 20 seconds, and 1:10 HCl:H<sub>2</sub>O for 20 seconds, respectively. The electroplating is performed in a standard electroplating solution of CuSO<sub>4</sub> and H<sub>2</sub>SO<sub>4</sub> [100] for 25 minutes using 10 mA/cm<sup>2</sup> of current density and a copper anode, yielding a 5  $\mu\text{m}$  thick copper layer. After copper electroplating, the photoresist mold is stripped in acetone, and the seed layers in the non-plated regions are removed. The thin copper is removed by dipping the sample into NH<sub>4</sub>OH saturated with CuSO<sub>4</sub> (“blue etch”) for 4 minutes. The titanium layers are removed again in the 1:18 HF:H<sub>2</sub>O.

The next step is to form the Parylene C insulation layer. Before coating the Parylene C, the copper surface is thoroughly cleaned via solvents and O<sub>2</sub> plasma. The 1.5  $\mu\text{m}$  thick Parylene C is then coated to the entire sample via CVD using SCS PDS2010 LABCOTER® 2 coating system. Before depositing the second layer conductor, the Parylene surface is pretreated with O<sub>2</sub> plasma to remove organic

contaminants and to roughen the surface. The plasma treatments before and after the Parylene coating are very important for adhesion at the Parylene-copper interfaces.

The second conductor layer is fabricated in a similar manner. After both layers of conductors are fabricated, the exposed Parylene is removed by O<sub>2</sub> reactive ion etch. The second conductor layer acts as a mask during this etch step, so that the only Parylene that remains is in between the two layers. The two conductor layers are then tested for electrical insulation via simple conductivity checks. Once the insulation is confirmed, the front side process is finished.

The backside of the wafer is then patterned via front-to-back alignment using AZ9260 photoresist defining the etch mask for the through-wafer backside silicon etch. Then using photoresist for temporary adhesion, the wafer is mounted front-side down to a dummy wafer to protect the front surface. The backside deep reactive ion etching is then performed using standard Bosch process [101]. Since the streets between the dies are patterned on the backside, the dies become separated from each other after the etching. The dies are then released from the dummy wafer by immersing in acetone for ~5 hours. A picture of the final microfabricated structure is shown in [Figure 5-4](#).

### **5.3. Device Testing**

Before mounting the microfabricated part to the magnet assembly, the impedances of the conductors are tested using an Agilent 4294A impedance analyzer. The testing is performed on a probe station shield in a Faraday cage. Since the resistances of the conductors are expected to be very small, any parasitic resistance such as a contact resistance or the probe wiring could significantly affect the measurement. To mitigate this, four-point impedance measurements are used for each measurement. Two probes are in contact with each electrode, one for sourcing, and the

other for measurement. Using a current of 1 mA, the self-impedance of the top and the bottom conductors between 4 kHz and 10 kHz (the frequency range is selected around the expected resonant frequency) are plotted in [Figure 5-5](#). From the plot, the resistances of the top and the bottom conductors within the specified frequency range are estimated to be 0.12  $\Omega$  and 0.35  $\Omega$ , respectively. The self-inductances of the top and the bottom conductors are both around 1  $\mu\text{H}$ . The measured results are questionable due to the unexpected large difference between the beam resistances, the larger than normal inductance, and the unusual spikes in the bottom beam's inductance and resistance curves. The sources of the measurement error include the quality of the electrical contact between the probe and the electrodes, the effectiveness of the equipment calibration when non-standard test cables are used. All are limited by the quality of the test facility.

After the standalone testing, the microfabricated structure is mounted on the magnet assembly for whole device characterization of the ET, as shown in [Figure 5-6](#). Again, to ensure the accuracy of the results, each bond pad is contacted by two separate test probes, and a total of eight probes are used. On each of the primary conductor's electrodes, one probe is used to source power, and the other is used to measure the actual input voltage across the conductor. On each of the secondary conductor's electrodes, one probe is used to connect to the load, while the other is used to measure the output voltage.

Before attaching any load, the open-circuit voltage gain frequency response is measured with the SR785 signal analyzer. The system is tested using each of the conductors as the primary conductor alternately. With excitation voltage amplitude

of 1 mV, the frequency response of the open-circuit voltage gain is measured between 1 kHz and 10 kHz. As shown in [Figure 5-7](#), when the top conductor is used as the primary conductor, a peak voltage gain of 0.978 is obtained at 5.69 kHz; when the bottom conductor is used as the primary conductor, the peak voltage gain of 0.723 is obtained at the same frequency. The difference in the voltage gain may be attributed by the difference in the transverse flux density of the conductors (they are at slightly different vertical positions with respect to the underlying magnets), which differentiates the transduction coefficients and the coupling strengths.

The coupling strengths can be estimated by using (3-39) or the definition  $\gamma = \frac{K^2}{Rb}$  to obtain the same result. Since the quality factor is easier to extract than the damping coefficient from the open-circuit voltage gain frequency response, and all the other parameters in (3-39) are readily available, (3-39) is used to estimate the coupling strength. The average transverse flux density along each conductor is estimated from FEM simulation to be 0.926 T and 0.931 T, respectively. By measuring the -3 dB bandwidth of the response curve, the measured mechanical quality factors in each configuration are estimated to be 17 and 51, respectively. Theoretically, these two numbers should be the same, because the mechanical resonator is the same for both configurations. The difference in the measured mechanical quality factors may arise from simple experimental variations or because of different thermal conditions in each configuration. Specifically, the primary conductor is heated to a higher temperature than the secondary, because there is no current flow in the secondary conductor at open-circuit condition. Further investigation is out of the scope of the study. The next term,

$\frac{1}{\rho_c \rho_m}$  is calculated to be  $\sim 6,532 \text{ m}^2/(\Omega \cdot \text{kg})$ , assuming that the electroplated copper

shares the same density and resistivity as bulk copper. The volume ratio is calculated as 1.22 for the clamped-clamped beam, assuming that the Parylene layer adds negligible mass. Using all these parameters, the top and bottom coupling strengths are estimated to be 21 and 63, respectively. According to (3-17), the maximum efficiency is expected to be  $\sim 78\%$ .

Next, the power efficiency measurement is performed using different load resistances. In this measurement, the bottom conductor is used as the primary conductor. The signal analyzer is used to provide a  $1 \text{ mV}_{\text{pk}}$  source voltage to the bottom conductor. A variable resistor is connected to the top conductor. With each resistance value, the input power is first measured, followed by the output power and the actual load resistance. Due to the substantial measurement noise and the low signal magnitude, it is difficult to calculate the power from the time waveforms, like what is presented in [Chapter 4](#). Therefore, the power is measured via measuring the real part of the cross-spectrum of the voltage and current spectra in the swept sine mode, which theoretically gives the frequency response of the real power. The power at the mechanical natural frequency is recorded. To obtain the cross spectrum, the current is measured with the Tektronix TCP312 current probe.

To measure the actual load resistance that “appears” to the secondary conductor without disturbing the setup, the ratio between the measured output voltage and output current is used to calculate the load resistance. As expected, the ratio does not change with frequency, because the load is resistive.

The measured input/output power and power efficiency is shown in [Figure 5-8](#). A maximum efficiency of 40% was obtained with 0.9  $\Omega$  load resistance. Since this is the minimum possible load resistance (achieved when the output cable was shorted), a higher efficiency may be possible if a lower load resistance were possible.

#### **5.4. Application Example**

Since the microscale prototype of ET has demonstrated expected functionality and the theoretical analysis has shown promise for potential improvements in efficiency and power density. This section attempts to investigate the potential application of the ET through a simple example: a resonant power inverter. First, a brief background review of resonant power converter is provided, followed by an overview of the proposed concept. Last, experimental demonstration and characterization of the system is presented.

##### **5.4.1. Background**

Resonant power converters, as shown in [Figure 5-9](#), are a new generation of switched-mode power converters that use an LC resonant tank as a part of the circuit. In a resonant converter, the input voltage or current is converted to a square wave via the use of a switching network [102]. The square wave is converted (filtered) to a sinusoidal wave by the resonant tank. The sinusoidal wave is then stepped up or down by a transformer. If a dc output is desired, an output rectifier is connected. If an ac output is needed, an LC filter is connected to the output to further remove unwanted harmonics. The major advantage of the resonant converter is its zero-voltage-switching (ZVS) or zero-current-switching (ZCS) capability. Since the switches in the switching network experience alternating voltage and current for each cycle, it is possible to turn on or off the switches when the current or voltage is zero. This dramatically reduces the

transistor switching loss and enables high switching frequency to reduce the size of the passive components.

Passive components involved in a resonant converter include at least one inductor, one capacitor, and a transformer, which are all among the largest components in a power electronic circuit. In both the PT and the ET, these “components” are all embedded in the transformer itself. Therefore, these resonant type transformers are good candidates to replace conventional solutions where discrete passive components are used. In fact, numerous works have been published on PT-based resonant converters. Most of these works adopt class E [103-108] or half-bridge [31, 33] amplifiers as the input stage, as shown in [Figure 5-10](#). Due to the lack of the inductive components in the PT electrical domain, at least one external inductor is used in these topologies to smooth the input current and enable ZVS. Inductor-less half-bridge resonant converter with ZVS capability is possible by operating the PT at a frequency just above the resonant frequency when the apparent input impedance is inductive [35, 109]. However, this requires even more complicated control and model analysis techniques. Also, operating at non-resonant frequency could reduce the efficiency and power density of the PT [110].

Like the PT, the LEM circuit model for the ET also comprises an embedded resonator and transformer, which makes possible its use in a resonant converter. More importantly, the input impedance of an ET is inductive, even while operating at the resonant frequency. Therefore, no external inductor or complicated frequency control is needed to implement ZVS.

As seen in [Figure 5-11](#), a resonant converter topology with parallel connected LLC resonant tank [111-114] (also known as LLC-PRC topology) provides near seamless adoption of the ET. The circuit shown is configured as an inverter, which will be implemented later in this work. The ET provides all of the LLC-PRC “circuit elements” which are required; no additional passive components are needed on the input end. This topology is known to have low voltage stress on the tank capacitor, which in the ET is interpreted as small velocity, or strain on the compliance element. A half-bridge switching network is also a good candidate for the input stage.

#### **5.4.2. Demonstration of Resonant Inverter Using Electrodynamic Transformer**

For this preliminary demonstration, a single switch that is connected in series with the source is used to build a simple demonstration system to validate the concept. The system implementation is shown in [Figure 5-12](#). The demonstrated system is configured as a resonant inverter with a 10 nF filter capacitor connected at the output. The input is provided by an isolated voltage source (Stanford Research Systems, SIM928) generating 0.01 V<sub>dc</sub>. The power supply output is connected to a P-channel MOSFET (NDP6020P), which is controlled by a function generator (Agilent 33120A) providing a 1 V<sub>pk</sub> square wave. The switched waveform is directly connected to the ET and filtered by the mechanical resonator, creating a close-to-sinusoidal vibration of the beam. As a result, a near-sinusoidal output voltage is generated. The voltage is slightly smoothed out by the output filter capacitor.

With the switching frequency tuned to the resonant frequency of the ET, the captured waveforms are shown in [Figure 5-13](#). It can be seen that the output voltage is sinusoidal with two spikes in each cycle. This is due to the non-zero-voltage switching of the MOSFET. As the MOSFET is turned on, the input voltage abruptly jumps to the

source voltage of 0.01 V, because the voltage across the MOSFET is not zero before switching. As the input current suddenly increases, the input voltage rapidly drops due to the voltage drop across the MOSFET on-resistance and the internal resistance of the voltage source. When the MOSFET is turned off, the input voltage slightly rises after a brief oscillation due to the parasitic MOSFET capacitor. However, the MOSFET turns on again before the input voltage rises to the level of the source voltage to enable ZVS. The situation improves slightly as the duty ratio of the switching waveform is decreased. However, in the implementation here, ZVS could not be achieved, possibly due to the small value of the input inductance of the ET.

The efficiency and input/output power of the ac inverter are measured on the oscilloscope with different load resistances. The power and efficiency vs. load resistance is plotted in [Figure 5-14](#). It can be seen that a maximum efficiency of 16% is obtained at the minimum achievable load resistance of 0.9  $\Omega$ . The efficiency is significantly lower than that of the ET itself. The reason probably lies in the lack of ZVS, and the performance of the MOSFET. To implement ZVS, a higher input inductance may be desired. A maximum power of 0.25  $\mu\text{W}$  is delivered to the load with the 0.01  $V_{\text{dc}}$  input. This is not the power capacity of the device. Unfortunately, the device is mechanically damaged before attempting to capture the power capacity with the extreme input condition. Therefore, the maximum possible power density of the device is unknown.

## 5.5. Summary and Discussion

A microfabricated ET has been demonstrated in this chapter. A maximum measured efficiency of 40% is promising as a pilot prototype, while the estimated coupling strengths predict a maximum efficiency of 78%. The discrepancy is possibly

due to the error in the coupling strength estimation and possible nonlinearity of the device.

While the semi-microfabricated device here demonstrates basic functionality of the ET, there is plenty of room for improvement. First, the magnetic field strength could be increased. For example, the  $\sim 500$   $\mu\text{m}$  gap between the copper and the magnet surface due to the thickness of the silicon substrate could be reduced to achieve much higher flux density. As shown in [Figure 5-15](#), up to 1.7 T could be achieved if the gap is reduced to 100  $\mu\text{m}$ . This could be possible through microfabricating the magnets on the same substrate. Alternatively, soft magnetic material could be integrated to the magnetic assembly to concentrate flux. Second, the mechanical quality factor could be improved. The measured mechanical quality is lower than normal (typically  $>100$ ) possibly due to the impact of the testing probe and viscous air damping. A much higher quality factor is expected on a vacuum-packaged wire-bonded device. The Parylene insulation layer may also have effect on the quality factor. A further investigation can be performed via varying the thickness of the Parylene insulation layer or changing the insulation material. Third, the volume ratio could be improved by adopting tapered structure as shown in [Figure 5-16](#), where the width of the beam is narrower at the center than at the ends, so that the volume attributed to the dynamic mass is reduced comparing to the total conductor volume. However, the trade-off of this design is the reduced maximum current, and therefore reduced device power density. Furthermore, dedicated efforts could be performed to analyze and optimize the material properties of the electroplated beams. Lastly, completely different device architectures could be considered. The clamped-clamped beam structure employed in these prototypes are

easy to fabricate, but are prone to in-plane stress/strain, which affects the mechanical compliance of the beam and overall device performance.

The application of ET in the LLC-PRC resonant inverter provides a promising example of how ET could reduce the physical size and complexity of power electronic system. The efficiency can be improved significantly by implementing ZVS through carefully designing the parameters of the device and the driving signal. In order to find the appropriate parameters, more investigation can be performed through circuit simulation using the equivalent circuit model of the ET. The efficiency can also be improved by using a better input stage, such as the half-bridge topology.

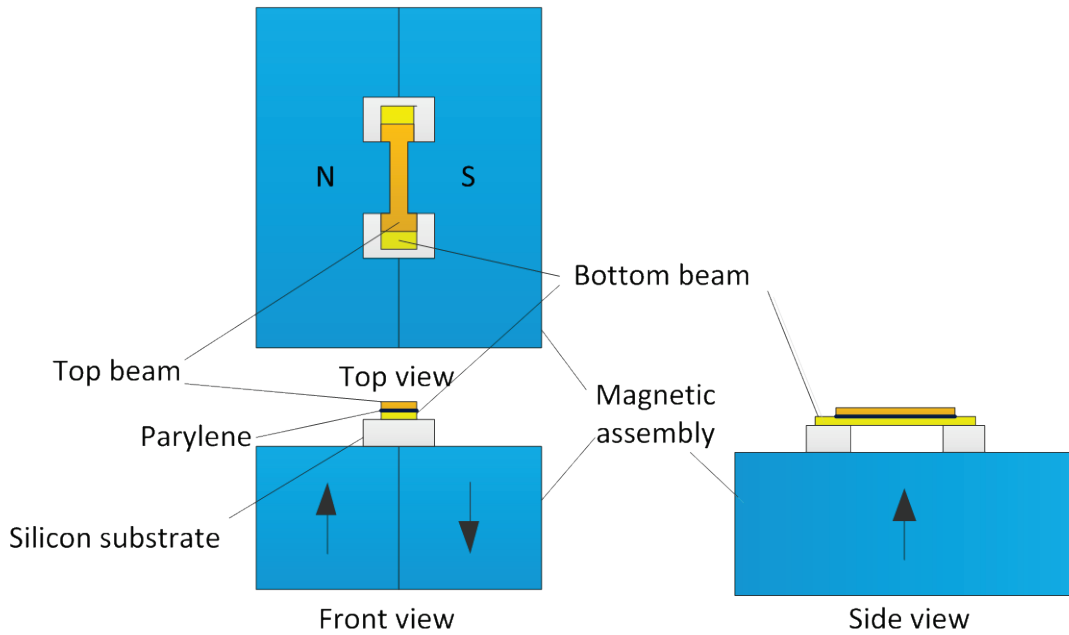


Figure 5-1. Schematic of the microscale electrodynamic transformer.

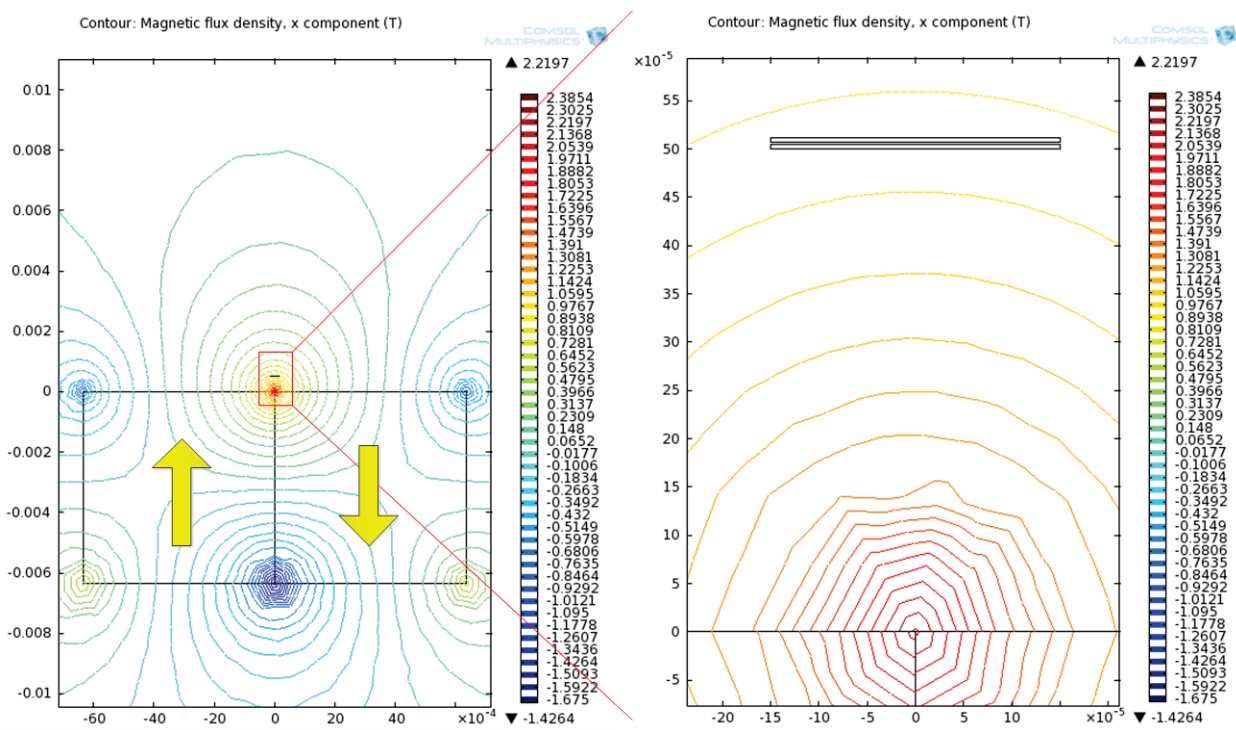


Figure 5-2. Finite element simulation of the magnetic assembly.

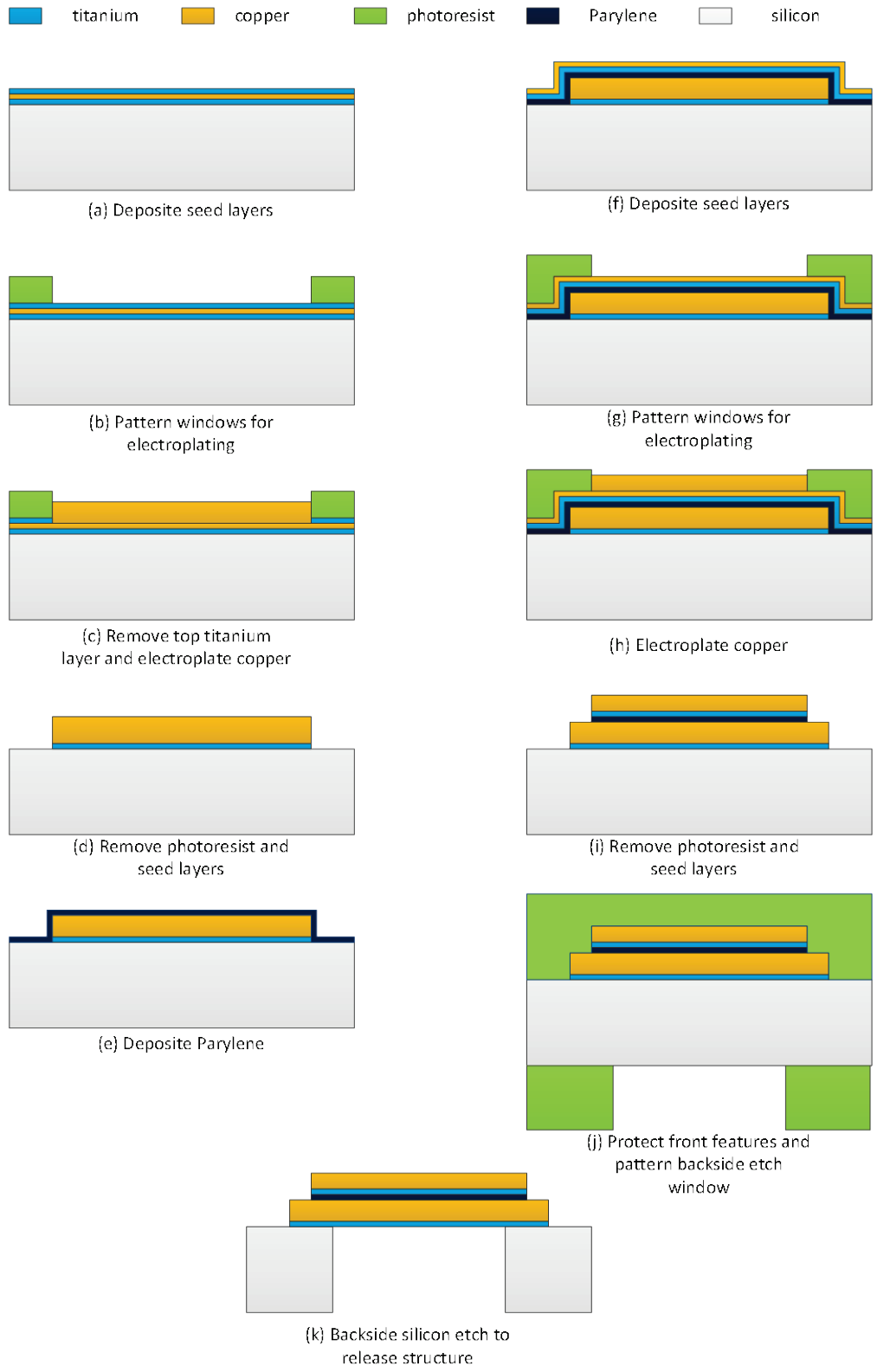


Figure 5-3. Fabrication process of the microfabricated part of the electrodynamic transformer (side view).

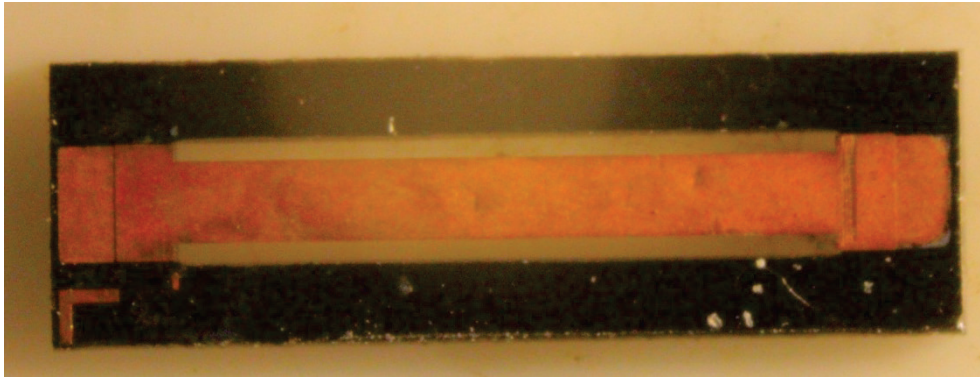


Figure 5-4. Top-view photograph of the microfabricated beam structures of the electrodynamic transformer.

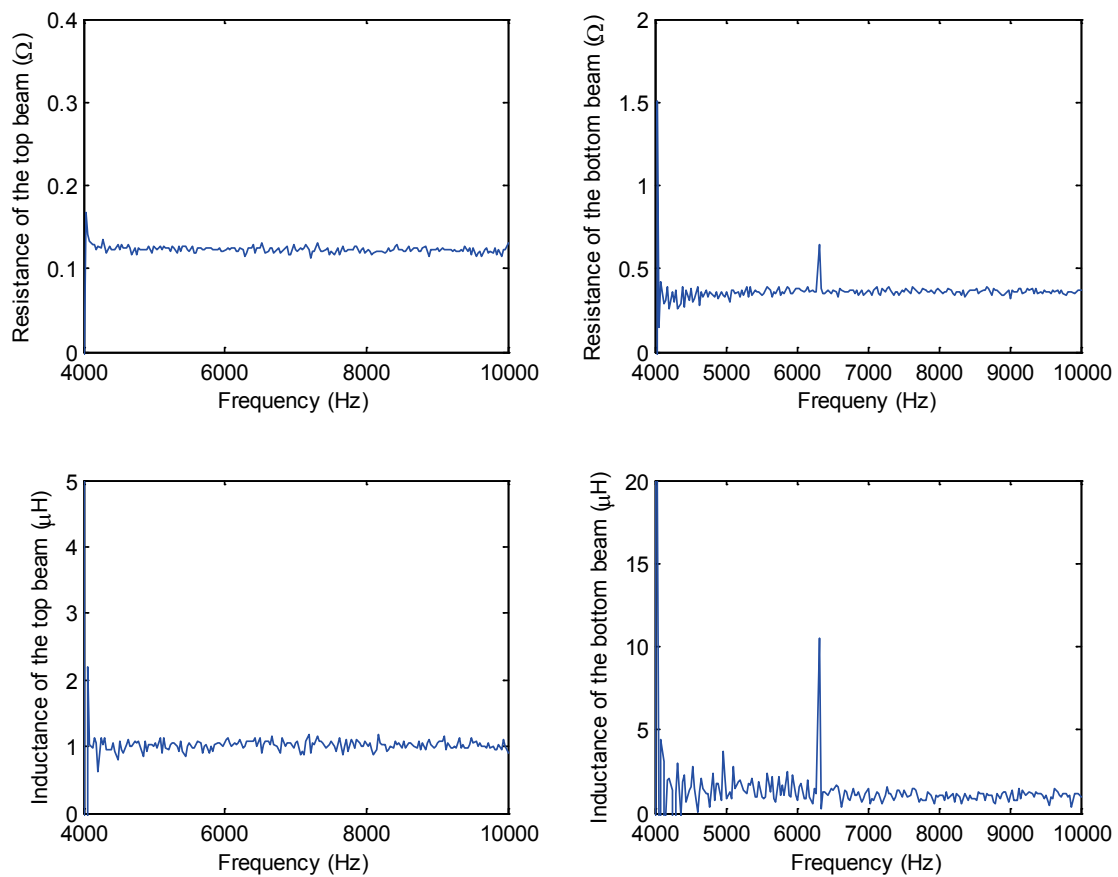


Figure 5-5. Measured impedance of the top and the bottom beams.

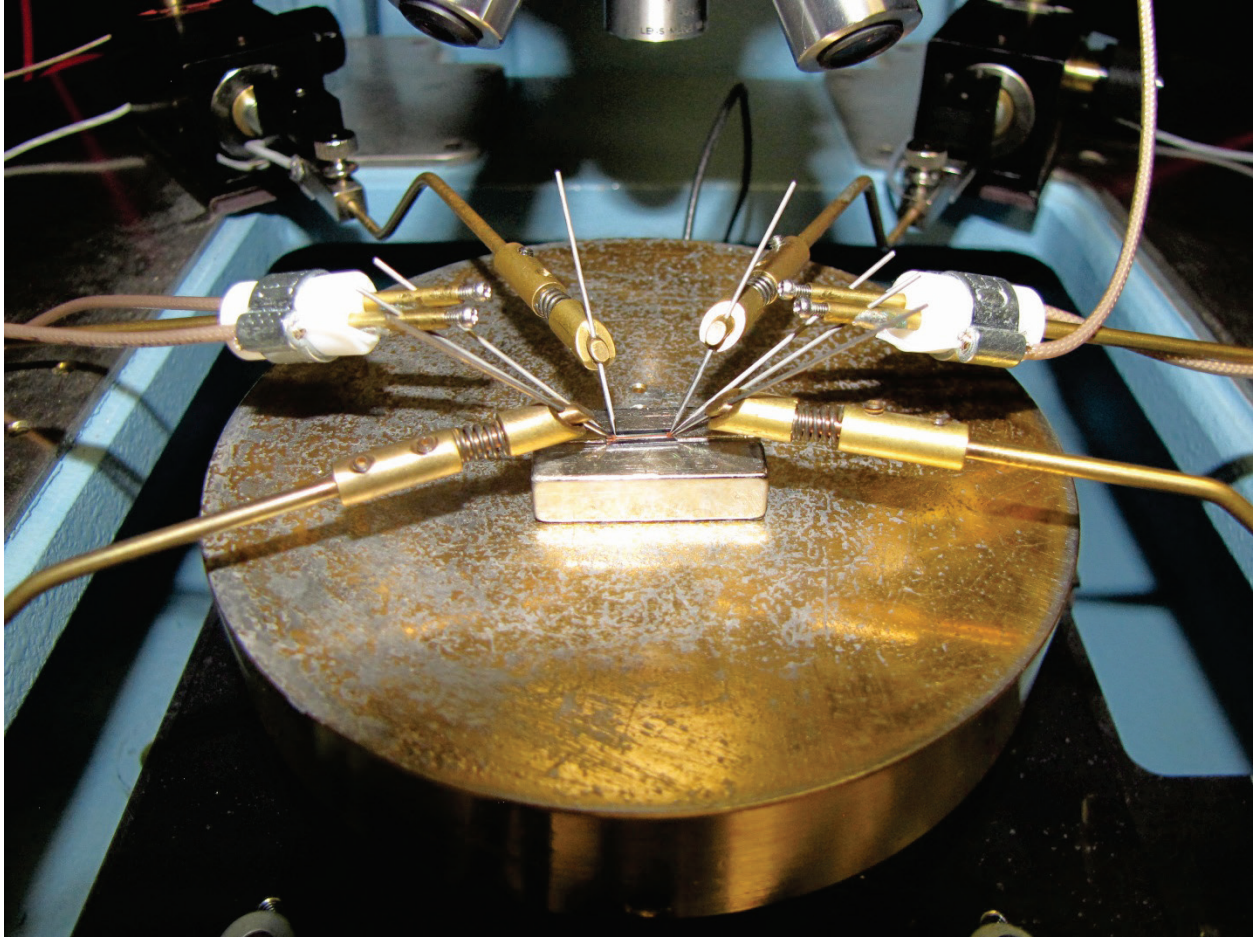


Figure 5-6. The microscale electrodynamic transformer under test on a probe station.

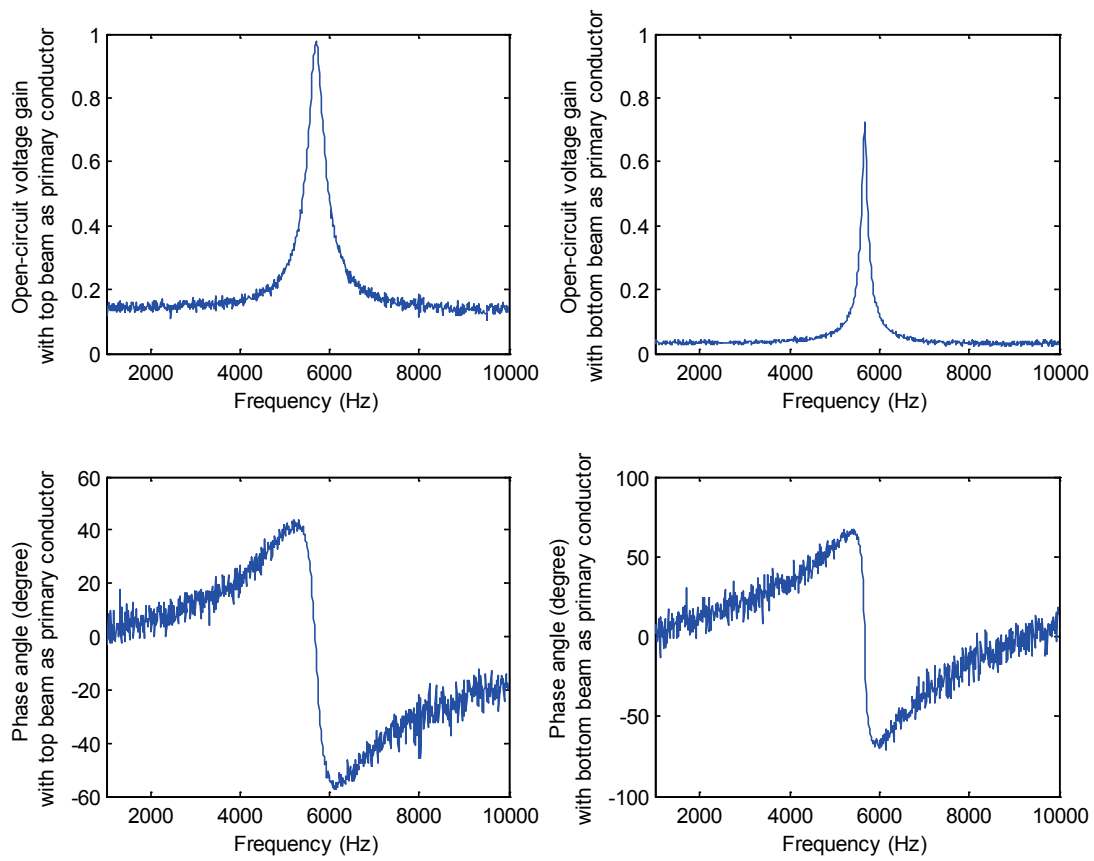


Figure 5-7. Open-circuit voltage gain frequency response with different beams as the primary conductor.

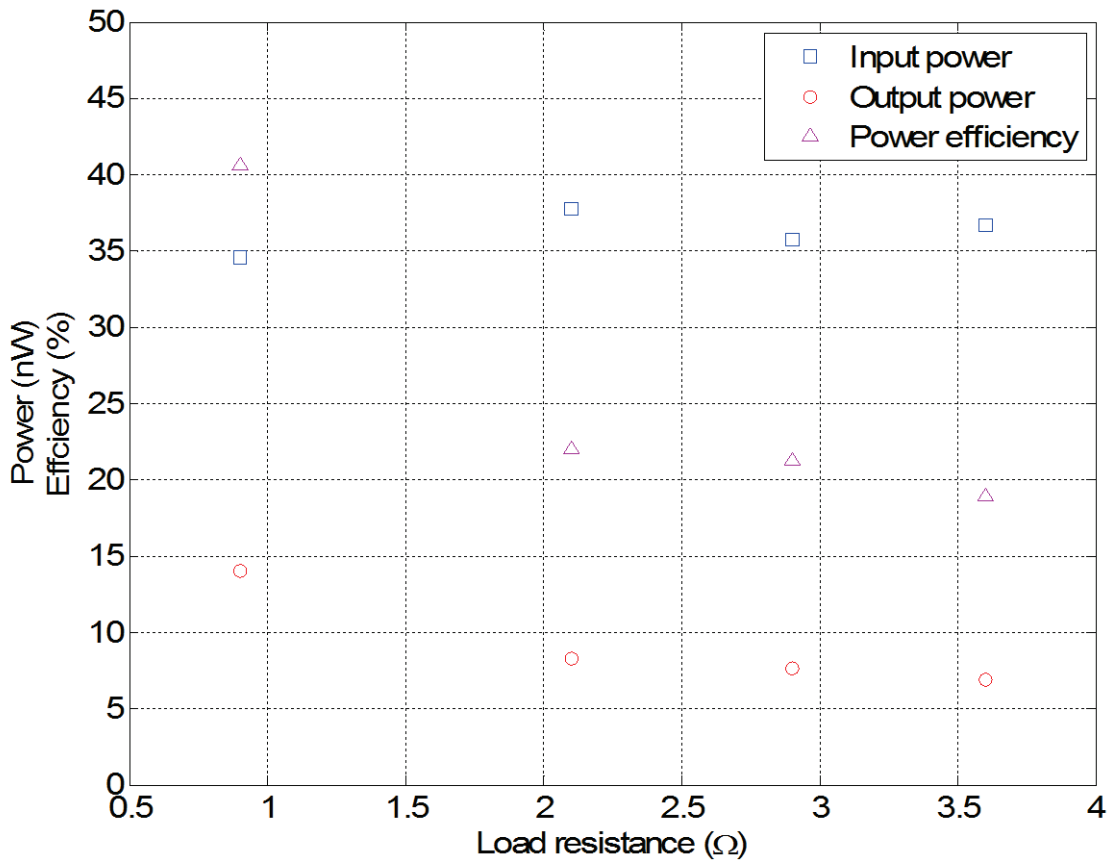


Figure 5-8. Input and output power, and efficiency measurements at different load resistances.

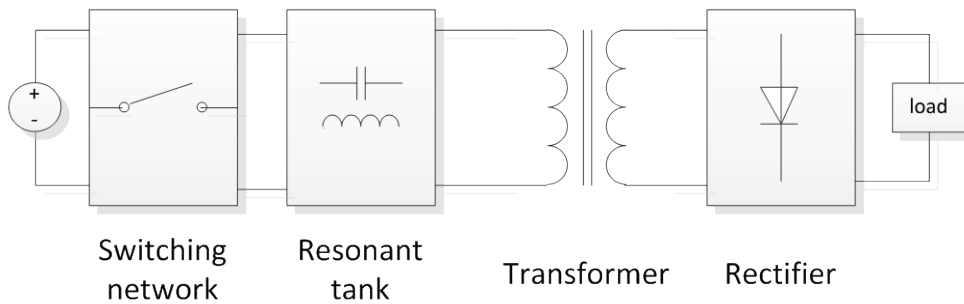


Figure 5-9. Block diagram of a resonant converter.

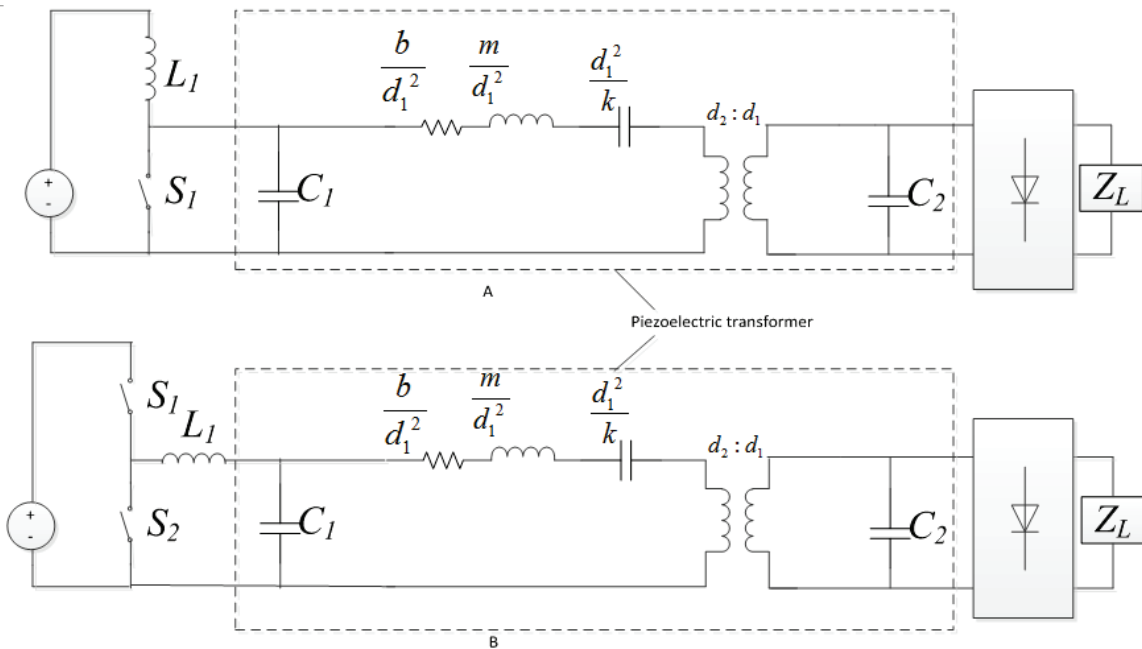


Figure 5-10. Resonant converters using a piezoelectric transformer. B) Converter using a class-E input stage. B) Converter using a half-bridge input stage.

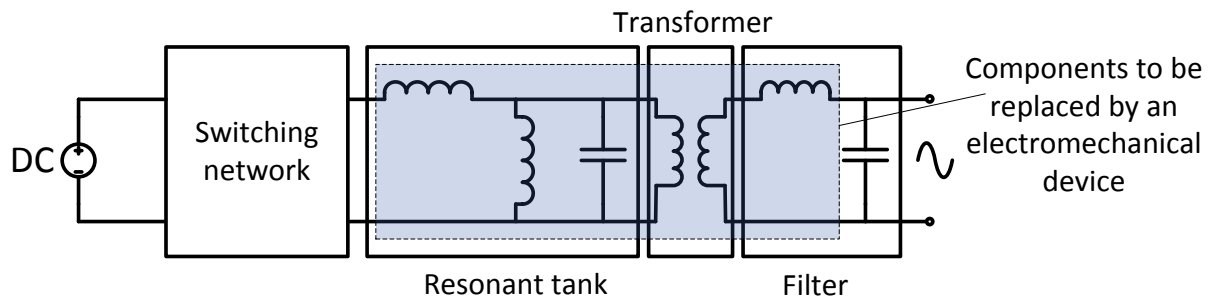


Figure 5-11. Circuit diagram of an LLC-PRC resonant inverter showing components that can potentially be replaced by an electrodynamic transformer.

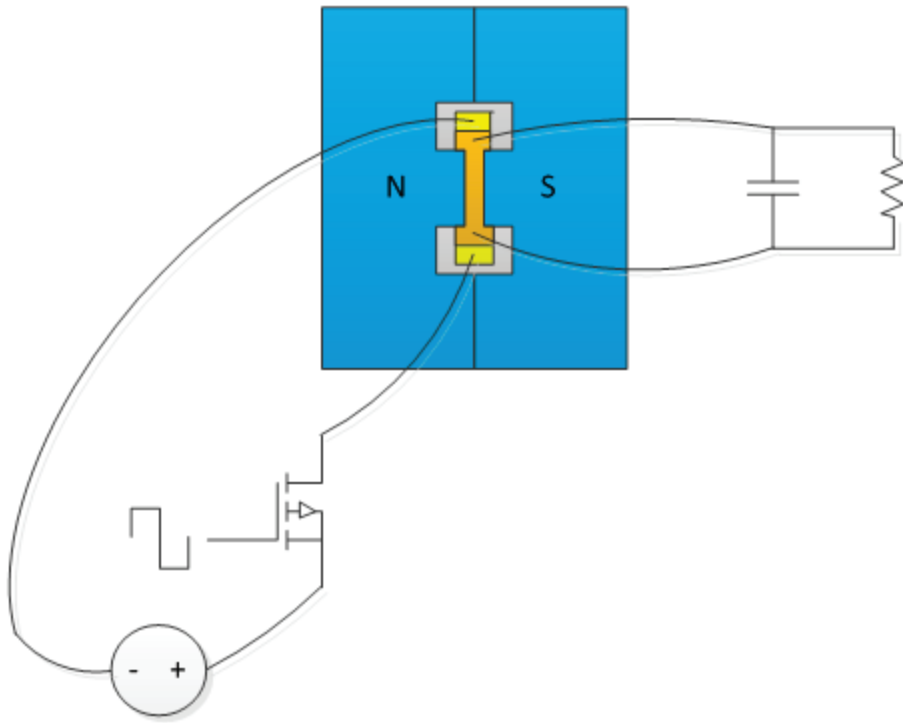


Figure 5-12. Implementation of LLC-PRC resonant inverter using an electrodynamic transformer.

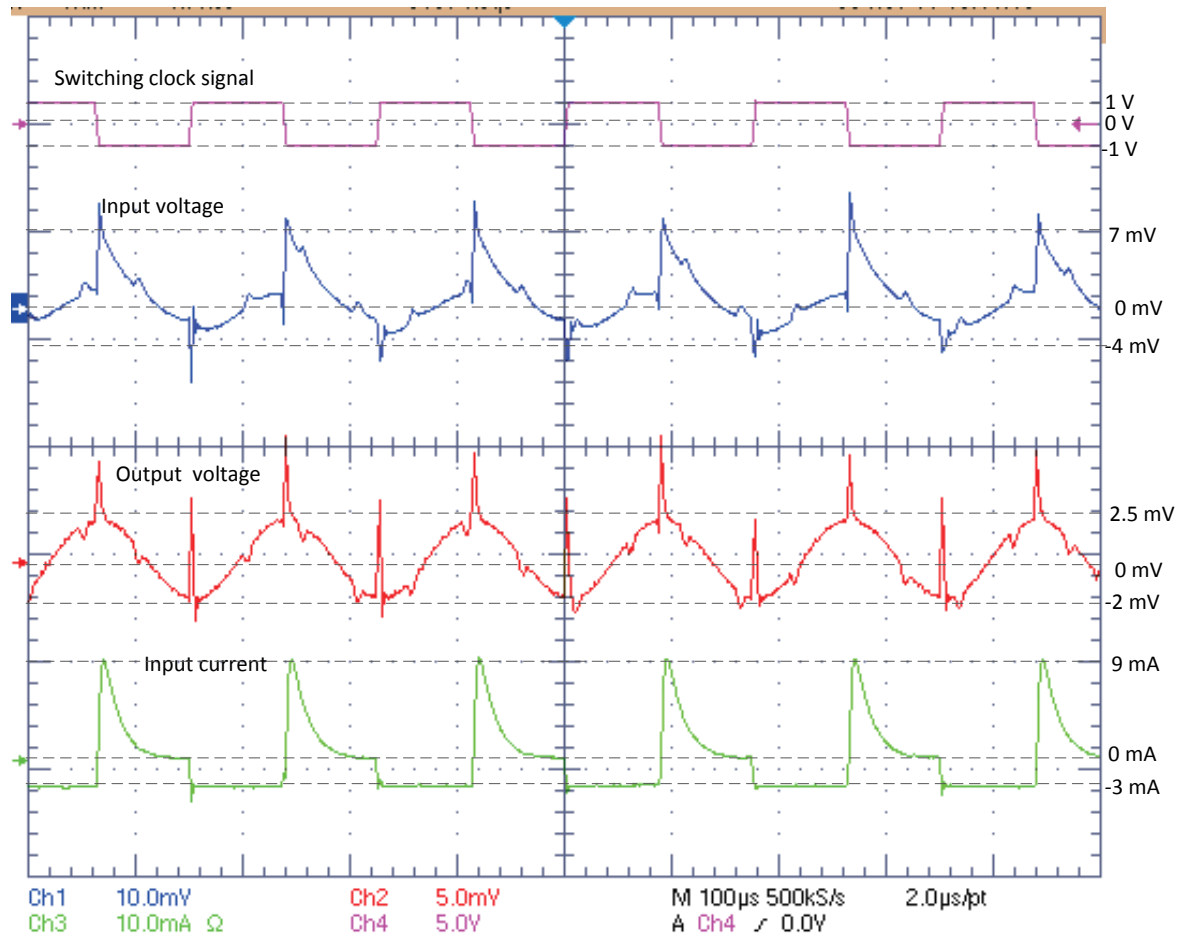


Figure 5-13. Waveforms captured for the resonant inverter.

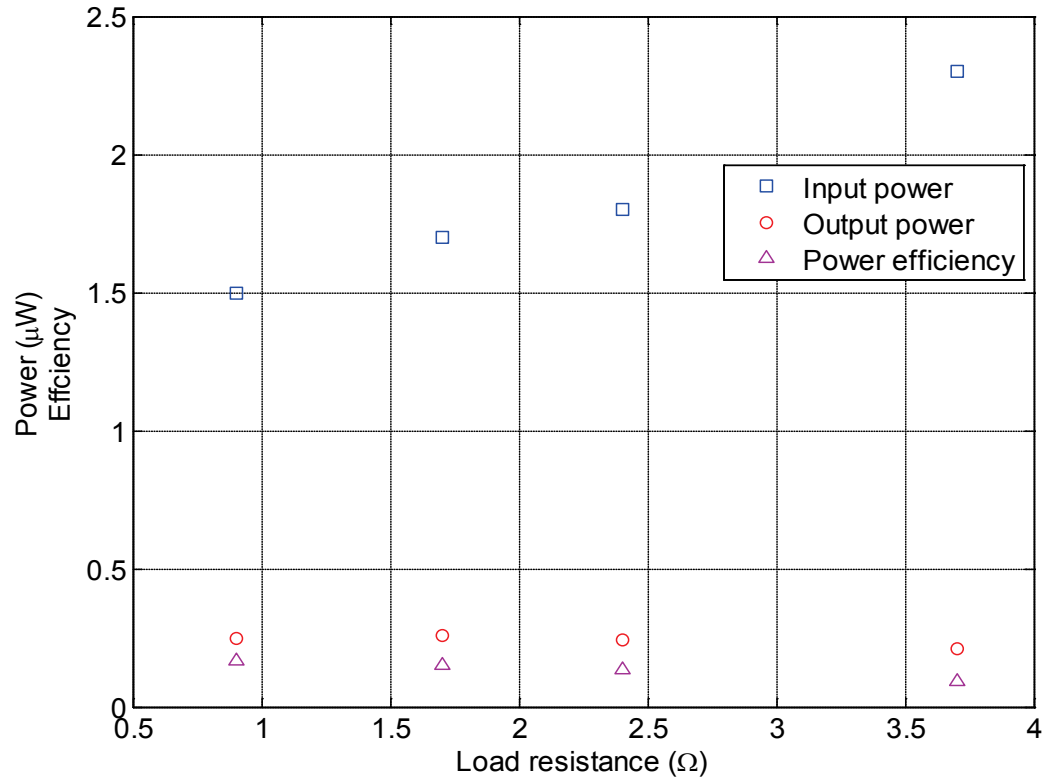


Figure 5-14. Input/output power and efficiency of the resonant inverter at different load resistances.

Line Graph: Magnetic flux density, x component (T)

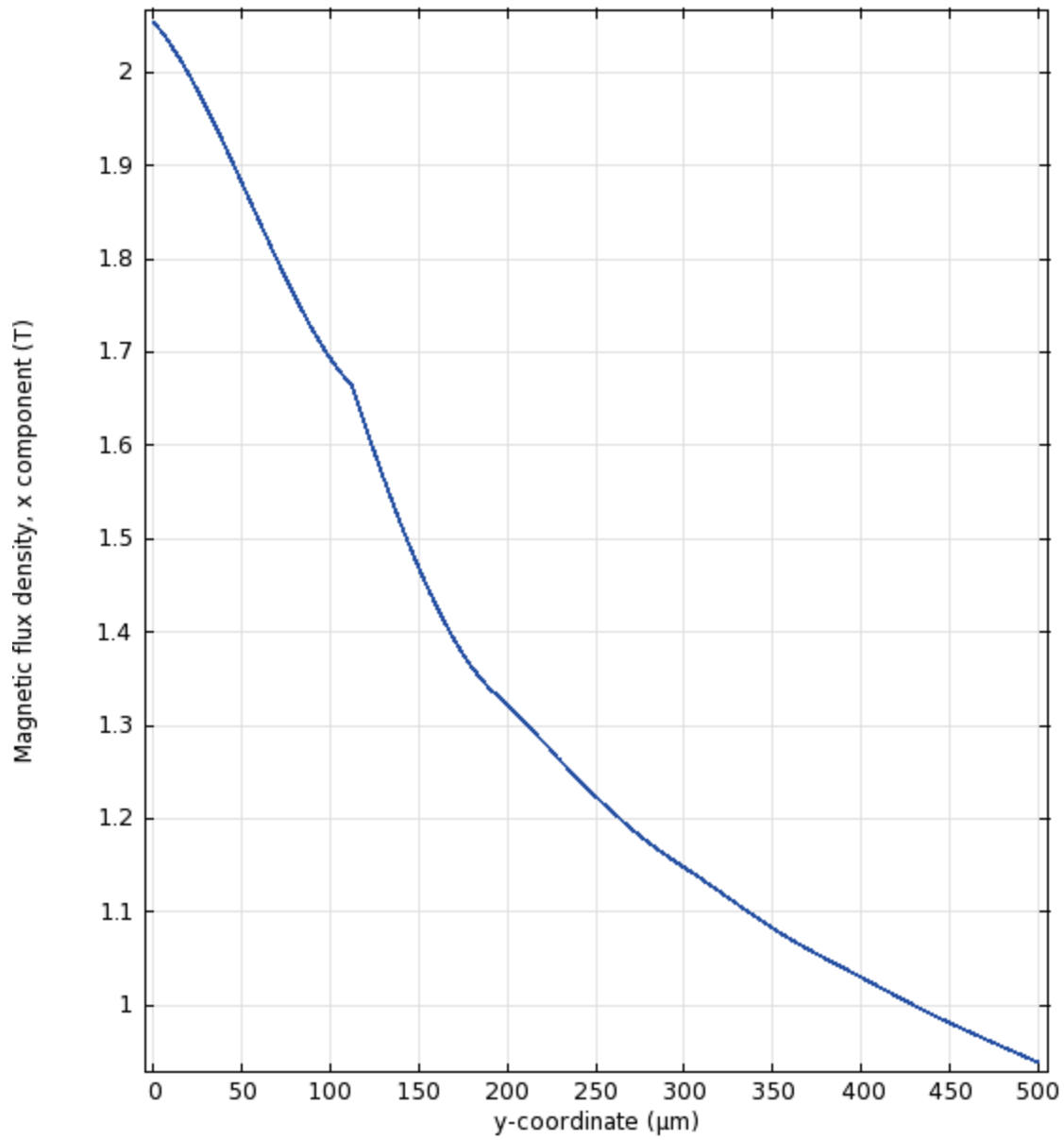


Figure 5-15. Transverse flux density vs. distance from the magnet surface.

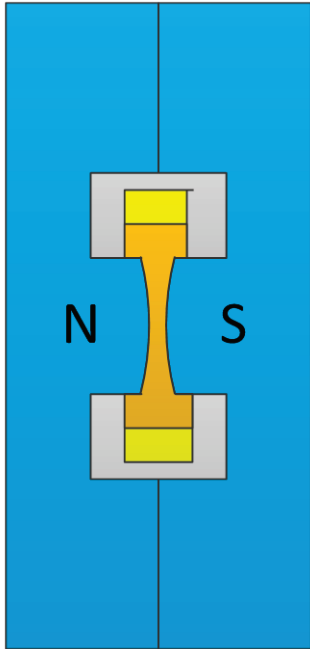


Figure 5-16. Electrodynamic transformer with tapered beam.

## CHAPTER 6 CONCLUSION

The major overall focus of this dissertation is to investigate the feasibility of the ET concept as an efficient, power-dense alternative to replace the EMT or PT in certain power electronic systems. The key figures of merit that are evaluated are the efficiency and the power density. Some other characteristics of the ET such as frequency response, input/output impedances are also investigated. Design considerations for performance improvement are also explored. In the first section of this chapter, the research contributions of this work are listed. The next section summarizes the major findings and conclusions. The final section suggests future works to continue the ET research.

### **6.1. Summary of Research Contributions**

The following is a list of research contributions of this work.

- Among the modern literature, this is the first systematic study of the two-port electrodynamic transducers for electrical energy transfer. The ET concept investigated here is a parallel concept to PTs, which have been investigated for several decades.
- Investigated the ET concept both theoretically and experimentally.
- Demonstrated and validated a LEM of the ET.
- Fabricated and characterized microscale ET and demonstrated its application in an ac/dc converter.
- Justified the viability of the ET's future application.

### **6.2. Summary of Major Conclusions**

Theoretical analysis on the LEM of the ET indicates that the efficiency of an ET is highly dependent on the coupling strength of both the primary and the secondary side. In order to increase the efficiency, both the primary and the secondary side coupling

strength need to be increased. In order to increase the coupling strength, the following design considerations have been generated:

- A well-designed electrodynamic transduction topology is desired. Specifically, an orthogonal transduction topology is suggested where the direction of the mechanical vibration, the magnetic flux density and the electric conductor length are perpendicular with each other. Such topology maximizes the electrodynamic transduction coefficient.
- A strong magnetic field oriented according to the orthogonal condition is desired. To achieve a strong magnetic field, the distance between the conductor and the magnetic field source need to be minimized. Delicate magnetic assemblies comprising multiple hard magnets and/or soft magnets (such as Halbach cylinder) are exceptionally effective in creating a strong magnetic field.
- A highly under-damped mechanical structure is desired. A key figure of merit is the settling time of the structure's self-oscillation after an initial disturbance. A long settling time is preferred. This is interpreted as high mechanical quality factor and low natural frequency.
- Materials need to be selected so that the conductors possess low resistivity, while the moving mass has low density. In a moving-conductor topology, ideal candidate conductor material possesses low resistivity-density-product.
- Volumetric distribution between the conductor and the moving mass is also important. The ratio of the conductor volume to the effective moving mass volume should be maximized.

Reported data in literature suggest a favorable scaling law of efficiency as the device scales down. It is estimated that a maximum efficiency of over 95% is possible for microscale ET. In the experimental demonstration, the microfabricated ET achieved a maximum efficiency of 40%, which is slightly higher than the macroscale prototype. Both the theoretical and experimental results suggest a promising efficiency for microscale ET. This compares favorably with EMT, whose efficiency decreases sharply as the dimension scales down.

The maximum power density of ET is a function of the maximum current density of the primary and the secondary conductors, the maximum spring force, and the

maximum displacement. A high-power-density ET needs to be designed such that all these limits are met simultaneously. Specific design guidelines to improve power density are reserved as a future work due to the complexity. Although experimental measurement of the maximum power density has not been successful, the theoretical analysis suggests that the maximum power density scales favorably as the device dimension reduces. An upper limit of  $100 \text{ W/cm}^3$  is estimated for macroscale ET, while it can reach  $10,000 \text{ W/cm}^3$  for microscale device. This is promising comparing to the PTs whose maximum power density is estimated to be  $330 \text{ W/cm}^3$ .

For practical application in power conversion systems, the ET offers embedded frequency selectivity, which is one of the major selling points of PT against EMT. The mechanical resonator inside the ET makes the implementation of resonant converter more compact and simple comparing to systems using a conventional EMT. Also, the inherent inductive input impedance makes it competitive to the PT-based resonant converter, where a separate inductor is needed to realize ZVS. Although the demonstrated ET-based resonant inverter does not achieve ZVS, it is possible through better device and circuit design (e.g. increase parasitic leakage inductance, adopt half-bridge input stage, etc.). This advantage of ET may possibly make one more step towards fully-integrated power converters.

### **6.3. Future Work**

Due to its exploratory nature, this study is far from exhaustive. However, since the results obtained herein provide a promising outlook for the future application of ET, it is advisable to lay out a road map for future research.

On the theoretical aspect, the lumped element model may be modified to accommodate more complicated operating conditions, such as nonlinearity and time- or

space-varying parameters, etc. In author's previous work [115], it has been demonstrated that it is possible for LEM to accommodate these complexities. Including nonlinearity into LEM facilitates the study on the maximum power density of the ET, because the device demonstrates substantial nonlinearity while operating at extreme conditions.

A dedicated effort on device optimization will be useful to further establish the potential of the ET performance. Such optimization effort requires a preliminary study on a variety of ET topologies, and more understanding on the physical relationships between LEM parameters.

It is also interesting to explore options of integrating magnetic assemblies "on-chip" via microfabrication, as well as packaging considerations of the whole device. With the magnets integrated on chip with the conductors, it is possible to improve the coupling strength and therefore the efficiency through increased flux density. Specifically, the package may provide vacuum environment to reduce the mechanical damping coefficient and increase the efficiency. A more reliable package allows more accurate characterization of the device, so that more insight can be provided on the future design and application.

From the application standpoint, an effort to search for other application areas would be interesting. The unique characteristics of ET (such as low input/output impedance, load-independent resonant frequency, etc.) may motivate special applications that are most suitable for the ET behavior. Eventually, ET-based fully-integrated power electronic systems could potentially reduce the size and weight of

electronic products, and extend battery life of portable devices. These enable more advanced technologies in areas such as remote sensing, autonomous robotics, etc.

APPENDIX A  
ELECTRODYNAMIC TRANSDUCTION AND FARADAY'S LAW OF INDUCTION

Consider an  $N$ -turn filamentary coil with area  $A$  translating in a time- and space-varying magnetic field pattern. Specifically, the real-time 3D position of a reference point on coil is given by

$$\bar{p}(t) = (x(t), y(t), z(t)). \quad (\text{A-1})$$

The flux density at a given point of the space at a given time instant is given by

$$\bar{B}(\bar{p}, t) = \bar{B}(x, y, z, t). \quad (\text{A-2})$$

Therefore, the total flux inside the coil at a given time instant is given by

$$\phi(\bar{p}(t), t) = \iint_A \bar{B}(\bar{p}(t), t) \cdot d\bar{A}. \quad (\text{A-3})$$

According to Faraday's Law of Induction, the voltage induced on the coil is given by

$$v = -N \frac{d\phi}{dt} = -N \frac{d \iint_A \bar{B}(\bar{p}(t), t) \cdot d\bar{A}}{dt} = -N \iint_A \frac{d\bar{B}(\bar{p}(t), t)}{dt} \cdot d\bar{A}. \quad (\text{A-4})$$

The right hand side of (A-4) can be further written as

$$-N \iint_A \frac{d\bar{B}(\bar{p}(t), t)}{dt} \cdot d\bar{A} = -N \iint_A \left[ \frac{d\bar{B}(\bar{p}, t)}{dt} + \frac{d\bar{B}(\bar{p}, t)}{d\bar{p}} \frac{d\bar{p}(t)}{dt} \right] \cdot d\bar{A}. \quad (\text{A-5})$$

Where  $\frac{d\bar{B}(\bar{p}, t)}{dt}$  measures the time variation of the magnetic field, and  $\frac{d\bar{B}(\bar{p}, t)}{d\bar{p}} \frac{d\bar{p}(t)}{dt}$

measures the spatial distribution of the field and the motion of the coil. Therefore, the

inducted voltage or EMF can be divided into two components that are called

“transformer EMF” and “motional EMF”, respectively:

$$v = v_{transformer} + v_{motional}, \quad (A-6)$$

Where

$$v_{transformer} = -N \iint_A \frac{d\bar{B}(\bar{p}, t)}{dt} \cdot d\bar{A}, \quad (A-7)$$

and

$$v_{motional} = -N \iint_A \frac{\partial \bar{B}(\bar{p}, t)}{\partial \bar{p}} \frac{d\bar{p}(t)}{dt} \cdot d\bar{A}. \quad (A-8)$$

Of these two components, the motional EMF is a part of the electrodynamic transduction that depicts the mechanical to electrical transduction. The transformer EMF is a part of the electromagnetic transduction where the transduction is from magnetic domain to electrical domain.

Now consider the motional EMF to further investigate the electrodynamic transduction. Notice that

$$\frac{\partial \bar{B}(\bar{p}, t)}{\partial \bar{p}} = \nabla \cdot \bar{B}(\bar{p}, t) \quad (A-9)$$

is the divergence of the magnetic flux density, and that

$$\frac{d\bar{p}}{dt} = \bar{u}(t) \quad (A-10)$$

is the velocity of the coil. Therefore, (A-8) can be rewritten as

$$v_{motional} = -N \iint_A \frac{\partial \bar{B}(\bar{p}, t)}{\partial \bar{p}} \frac{d\bar{p}(t)}{dt} \cdot d\bar{A} = -\bar{u}(t) \cdot N \iint_A [\nabla \cdot \bar{B}(\bar{p}, t)] \cdot d\bar{A}. \quad (A-11)$$

According to Stoke's Theorem, the surface integral a field's divergence is equal to the line integral (along the boundary of the surface) of the field's curl. Assuming that the

length of each turn of the coil is  $l_t$ , and the total length is  $Nl_t = l_c$ , (A-11) can be rewritten as

$$\begin{aligned} v_{\text{motional}} &= -\bar{u}(t) \cdot N \iint_A [\nabla \cdot \bar{B}(\bar{p}, t)] \cdot d\bar{A} = -\bar{u}(t) \cdot N \oint_{l_t} [\nabla \times \bar{B}(\bar{p}, t)] \cdot d\bar{l} \\ &= -\bar{u}(t) \cdot \oint_{l_c} [\nabla \times \bar{B}(\bar{p}, t)] \cdot d\bar{l} = -\bar{u}(t) \cdot \oint_{l_c} \bar{B}(\bar{p}, t) \times d\bar{l}. \end{aligned} \quad (\text{A-12})$$

The last equation of (A-12) is the integral form of the electrodynamic constitutive equation for mechanical to electrical transduction. The differential form of the equation that represents the voltage generated from an infinitesimal length of coil segment can be written as

$$dv_{\text{motional}} = -\bar{u}(t) \cdot \bar{B}(\bar{p}, t) \times d\bar{l}. \quad (\text{A-13})$$

Equation (A-13) is the electrodynamic constitutive equation used in [Section 2.4.2](#) for mechanical to electrical transduction. Unlike the direct use of the Faraday's Law in (A-4) where the flux inside a closed loop conductor is needed, (A-13) can be integrated to calculate the voltage generated by a coil segment of any shape (not necessarily a loop).

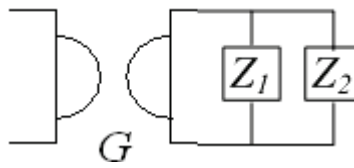
APPENDIX B  
PROPERTIES OF THE GYRATOR

The properties of the gyrator are listed in [Table B-1](#).

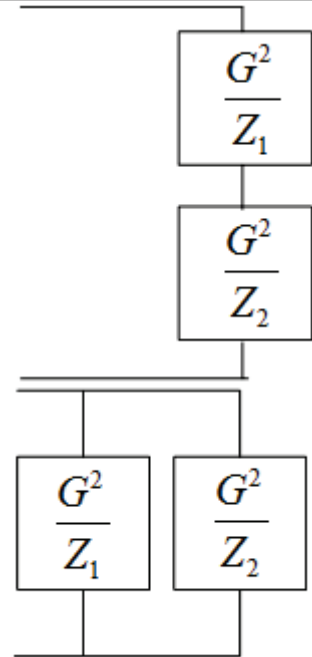
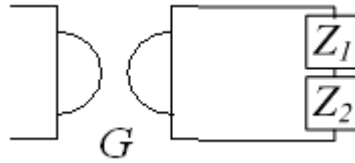
Table B-1. Properties of the gyrator

Property	Illustration	
	Original circuit	Equivalent Circuit
An effort source on one side of a gyrator appears as a flow source on the other side		
A flow source on one side of a gyrator appears as an effort source on the other side		
A generalized resistance connected to one side of a gyrator appears as a conductance on the other side		
A generalized compliance connected to one side of a gyrator appears as a generalized inertance on the other side		
A generalized inertance connected to one side of a gyrator appears as a generalized compliance on the other side		
Two cascaded gyrators are equivalent to a transformer		

Parallel-connected elements on one side of a gyrator appears as series-connected on the other side



Series-connected elements on one side of a gyrator appears as parallel-connected on the other side



## LIST OF REFERENCES

- [1] S. Duffy, C. Bozler, S. Rabe, J. Knecht, L. Travis, P. Wyatt, C. Keast, and M. Gouker, "MEMS microswitches for reconfigurable microwave circuitry," *IEEE Microwave and Wireless Components Letters*, vol. 11, pp. 106-108, 2001.
- [2] C. L. Goldsmith, Z. M. Yao, S. Eshelman, and D. Denniston, "Performance of low-loss RF MEMS capacitive switches," *IEEE Microwave and Guided Wave Letters*, vol. 8, pp. 269-271, 1998.
- [3] J. Y. Park, G. H. Kim, K. W. Chung, and J. U. Bu, "Monolithically integrated micromachined RF MEMS capacitive switches," *Sensors and Actuators a-Physical*, vol. 89, pp. 88-94, 2001.
- [4] I. J. Busch-Vishniac, *Electromechanical sensors and actuators*. New York: Springer, 1999.
- [5] S. D. Senturia, *Microsystem design*. Boston: Kluwer Academic Publishers, 2001.
- [6] H. A. C. Tilmans, "Equivalent circuit representation of electromechanical transducers .1. Lumped-parameter systems," *Journal of Micromechanics and Microengineering*, vol. 6, pp. 157-176, 1996.
- [7] F. A. Fischer, *Fundamentals of electroacoustics*. New York,: Interscience Publishers, 1955.
- [8] J. Merhaut, *Theory of electroacoustics*. New York ; London: McGraw-Hill International Book Co., 1981.
- [9] F. V. Hunt and Acoustical Society of America., *Electroacoustics : the analysis of transduction, and its historical background*. [New York]: Published by the American Institute of Physics for the Acoustical Society of America, 1982.
- [10] K. L. Ekinici, "Electromechanical transducers at the nanoscale: Actuation and sensing of motion in nanoelectromechanical systems (NEMS)," *Small*, vol. 1, pp. 786-797, 2005.
- [11] C. C. Chan, "An overview of electric vehicle technology," *Proceedings of the IEEE*, vol. 81, pp. 1202-1213, 1993.
- [12] Y. Hori, "Future vehicle driven by electricity and control - Research on four-wheel-motored "UOT Electric March II," *IEEE Transactions on Industrial Electronics*, vol. 51, pp. 954-962, 2004.

- [13] S. P. Beeby, M. J. Tudor, and N. M. White, "Energy harvesting vibration sources for microsystems applications," *Measurement Science & Technology*, vol. 17, pp. R175-R195, Dec 2006.
- [14] S. Muller, M. Deicke, and R. W. De Doncker, "Doubly fed induction generator systems for wind turbines," *IEEE Industry Applications Magazine*, vol. 8, pp. 26-33, 2002.
- [15] K. Rhinefrank, E. B. Agamloh, A. von Jouanne, A. K. Wallace, J. Prudell, K. Kimble, J. Aills, E. Schmidt, P. Chan, B. Sweeny, and A. Schacher, "Novel ocean energy permanent magnet linear generator buoy," *Renewable Energy*, vol. 31, pp. 1279-1298, 2006.
- [16] H. Akagi and H. Sato, "Control and performance of a doubly-fed induction machine intended for a flywheel energy storage system," *IEEE Transactions on Power Electronics*, vol. 17, pp. 109-116, 2002.
- [17] S. Krishnan, S. V. Garimella, G. M. Chrysler, and R. V. Mahajan, "Towards a Thermal Moore's Law," *Advanced Packaging, IEEE Transactions on*, vol. 30, pp. 462-474, 2007.
- [18] J. W. Kolar, U. Drofenik, J. Biela, M. L. Heldwein, H. Ertl, T. Friedli, and S. D. Round, "PWM Converter Power Density Barriers," in *Power Conversion Conference - Nagoya, 2007. PCC '07*, 2007, pp. P-9-P-29.
- [19] J. B. Wang, W. Y. Wang, G. W. Jewell, and D. Howe, "Design of a miniature permanent-magnet generator and energy storage system," *IEEE Transactions on Industrial Electronics*, vol. 52, pp. 1383-1390, 2005.
- [20] A. W. Lotfi and M. A. Wilkowski, "Issues and advances in high-frequency magnetics for switching power supplies," *Proceedings of the IEEE*, vol. 89, pp. 833-845, 2001.
- [21] P. Hazucha, G. Schrom, J. Hahn, B. A. Bloechel, P. Hack, G. E. Dermer, S. Narendra, D. Gardner, T. Karnik, V. De, and S. Borkar, "A 233-MHz 80%-87% efficient four-phase DC-DC converter utilizing air-core inductors on package," *IEEE Journal of Solid-State Circuits*, vol. 40, pp. 838-845, 2005.
- [22] S. C. Tang, S. Y. Hui, and H. S. H. Chung, "Coreless planar printed-circuit-board (PCB) transformers - A fundamental concept for signal and energy transfer," *IEEE Transactions on Power Electronics*, vol. 15, pp. 931-941, 2000.
- [23] P. D. Evans and B. Heffernan, "Electromagnetic considerations in power electronic converters," *Proceedings of the IEEE*, vol. 89, pp. 864-875, Jun 2001.

- [24] F. Uppenborn, *History of the transformer*. E. & F.N. Spon, 1889.
- [25] A. E. Crawford, "Piezoelectric ceramic transformers and filters," *Radio Engineers, Journal of the British Institution of*, vol. 21, pp. 353-360, 1961.
- [26] C. A. Rosen, "Ceramic transformers and filters," in *Proc. Electronic Comp. Symp.*, 1956, pp. 205-211.
- [27] C. A. Rosen, "Analysis and Design of Ceramic Transformers and Filter Elements " PhD, Syracuse University, 1956.
- [28] K. Uchino, "Piezoelectric Motors and Transformers," in *Piezoelectricity*. vol. 114, ed Berlin Heidelberg: Springer, 2008, pp. 257-277.
- [29] Y. Fuda, K. Kumasaka, M. Katsuno, H. Sato, and Y. Ino, "Piezoelectric transformer for cold cathode fluorescent lamp inverter," *Japanese Journal of Applied Physics Part 1-Regular Papers Short Notes & Review Papers*, vol. 36, pp. 3050-3052, 1997.
- [30] J. Yoo, K. Yoon, S. M. Hwang, S. Suh, J. Kim, and C. Yoo, "Electrical characteristics of high power piezoelectric transformer for 28 W fluorescent lamp," *Sensors and Actuators a-Physical*, vol. 90, pp. 132-137, 2001.
- [31] C. S. Moo, W. M. Chen, and H. K. Hsieh, "Electronic ballast with piezoelectric transformer for cold cathode fluorescent lamps," *IEE Proceedings-Electric Power Applications*, vol. 150, pp. 278-282, 2003.
- [32] Y. K. Lo, K. H. Wu, K. J. Pai, and H. J. Chiu, "Design and Implementation of RGB LED Drivers for LCD Backlight Modules," *IEEE Transactions on Industrial Electronics*, vol. 56, pp. 4862-4871, 2009.
- [33] M. Yamamoto, Y. Sasaki, A. Ochi, T. Inoue, and S. Hamamura, "Step-down piezoelectric transformer for AC-DC converters," *Japanese Journal of Applied Physics Part 1-Regular Papers Short Notes & Review Papers*, vol. 40, pp. 3637-3642, 2001.
- [34] P. Joung-hu, C. Sungjin, L. Sangmin, and B. H. Cho, "Gain-adjustment Technique for Resonant Power Converters with Piezoelectric Transformer," in *Power Electronics Specialists Conference, 2007. PESC 2007. IEEE*, 2007, pp. 2549-2553.
- [35] E. L. Horsley, N. Nguyen-Quang, M. P. Foster, and D. A. Stone, "Achieving ZVS in inductor-less half-bridge piezoelectric transformer based resonant converters," in *Power Electronics and Drive Systems, 2009. PEDS 2009. International Conference on*, 2009, pp. 446-451.

- [36] M. Pinto, H. Ribeiro, B. Borges, and M. Santos, "A resonant, frequency - tracking, step-down piezoelectric transformer based converter," in *Energy Conversion Congress and Exposition (ECCE), 2010 IEEE*, 2010, pp. 2004-2010.
- [37] J. C. Hathaway and D. F. Babcock, "Survey of Mechanical Filters and Their Applications," *Proceedings of the IRE*, vol. 45, pp. 5-16, 1957.
- [38] R. A. Johnson and A. E. Guenther, "III. Mechanical Filters and Resonators," *Sonics and Ultrasonics, IEEE Transactions on*, vol. 21, pp. 244-256, 1974.
- [39] K. Okazaki and T. Tanimoto, "ELECTROMECHANICAL STRENGTH AND FATIGUE OF FERROELECTRIC CERAMICS," *Ferroelectrics*, vol. 131, pp. 25-40, 1992.
- [40] T. Tanimoto, T. Yamamoto, and K. Okazaki, "Mechanical and electrical properties of piezoelectric ceramics under repeated compression fatigue tests," in *Applications of Ferroelectrics, 1990., IEEE 7th International Symposium on*, 1990, pp. 202-205.
- [41] R. G. Polcawich and S. Trolier-McKinstry, "Piezoelectric and dielectric reliability of lead zirconate titanate thin films," *Journal of Materials Research*, vol. 15, pp. 2505-2513, Nov 2000.
- [42] S. I. Shkuratov, E. F. Talantsev, J. Baird, H. Temkin, Y. Tkach, L. L. Altgilbers, and A. H. Stults, "Depolarization of a Pb(Zr<sub>52</sub>Ti<sub>48</sub>)O<sub>3</sub> Polycrystalline Piezoelectric Energy-Carrying Element of Compact Pulsed Power Generator by a Longitudinal Shock Wave," in *Pulsed Power Conference, 2005 IEEE*, 2005, pp. 529-532.
- [43] K. W. Kwok, M. K. Cheung, H. L. W. Chan, and C. L. Choy, "Depolarization of a piezoelectric film under an alternating current field," *Journal of Applied Physics*, vol. 101, pp. 054108-054108-6, 2007.
- [44] M. Al-Ahmad and R. Plana, "Material depolarization, dielectric hysteresis and power consumption investigations on tunable piezoelectric-based shunt microstrip resonator," in *Microwave Conference, 2007. European*, 2007, pp. 294-297.
- [45] H. Zhimin, L. Han Tong, and O. Eng Hong, "Reliability Evaluation of Piezoelectric Micro-Actuators With Application in Hard Disk Drives," *Magnetics, IEEE Transactions on*, vol. 44, pp. 3722-3725, 2008.
- [46] H. Zhimin, L. Han Tong, X. Min, and G. Guoxiao, "A reliability model for piezoelectric actuators," in *Power Engineering Conference, 2005. IPEC 2005. The 7th International*, 2005, pp. 939-944 Vol. 2.

- [47] L. Lin, C. T. C. Nguyen, R. T. Howe, and A. P. Pisano, "Microelectromechanical filters for signal processing," in *Micro Electro Mechanical Systems, 1992, MEMS '92, Proceedings. An Investigation of Micro Structures, Sensors, Actuators, Machines and Robot. IEEE, 1992*, pp. 226-231.
- [48] A. M. Flynn and S. R. Sanders, "Fundamental limits on energy transfer and circuit considerations for piezoelectric transformers," *Ieee Transactions on Power Electronics*, vol. 17, pp. 8-14, 2002.
- [49] F. Ashida and N. Noda, "Control of transient thermoelastic displacement in a piezoelectric based intelligent plate," *Journal of Intelligent Material Systems and Structures*, vol. 12, pp. 93-103, Feb 2001.
- [50] Y. Ootao and Y. Tanigawa, "Control of the transient thermoelastic displacement of a functionally graded rectangular plate bonded to a piezoelectric plate due to nonuniform heating," *Acta Mechanica*, vol. 148, pp. 17-33, 2001.
- [51] Y. P. Liu, D. Vasic, W. J. Wu, F. Costa, and C. K. Lee, "Electromagnetic Interference Analysis of DC-DC Converters Based on Piezoelectric Transformers," *Japanese Journal of Applied Physics*, vol. 49, p. 6, Jun 2010.
- [52] Y. Saito, H. Takao, T. Tani, T. Nonoyama, K. Takatori, T. Homma, T. Nagaya, and M. Nakamura, "Lead-free piezoceramics," *Nature*, vol. 432, pp. 84-87, Nov 2004.
- [53] J. F. Shepard, F. Chu, I. Kanno, and S. Trolier-McKinstry, "Characterization and aging response of the d(31) piezoelectric coefficient of lead zirconate titanate thin films," *Journal of Applied Physics*, vol. 85, pp. 6711-6716, May 1999.
- [54] A. Asiz, Z. Weiping, and X. Yunping, "Analysis of aging of piezoelectric crystal resonators," *Ultrasonics, Ferroelectrics and Frequency Control, IEEE Transactions on*, vol. 50, pp. 1647-1655, 2003.
- [55] M. G. Zhu, X. M. Li, Z. H. Guo, and W. Li, "Mechanism of low magnetic aging of Nd-Fe-B permanent magnet," *Acta Physica Sinica*, vol. 54, pp. 5895-5900, Dec 2005.
- [56] S. P. Thompson and M. B. Field, "Rotatory converters," *Electrical Engineers, Journal of the Institution of*, vol. 27, pp. 651-689, 1898.
- [57] L. Wilson, "A rotary converter," *Electrical Engineers, Journal of the Institution of*, vol. 28, pp. 367-388, 1899.

- [58] W. M. Thornton, "Experiments on synchronous converters," *Electrical Engineers, Journal of the Institution of*, vol. 32, pp. 573-596, 1903.
- [59] M. J. Tilney, "A new method of automatic boosting," *Electrical Engineers, Journal of the Institution of*, vol. 36, pp. 605-615, 1906.
- [60] M. Walker, "Rotary converters versus motor generators," *Electrical Engineers, Journal of the Institution of*, vol. 38, pp. 428-436, 1907.
- [61] P. T. Silvanus, "Note on Continuous-current Transformers," *Proceedings of the Physical Society of London*, vol. 9, p. 366, 1887.
- [62] A. Windhorn, "A hybrid static/rotary UPS system," *Industry Applications, IEEE Transactions on*, vol. 28, pp. 541-545, 1992.
- [63] C. Heising, M. Oettmeier, R. Bartelt, V. Staudt, and A. Steimel, "Single-phase 50-kW 16.7-Hz PI-controlled four-quadrant line-side converter lab model fed by rotary converter," in *Compatibility and Power Electronics, 2009. CPE '09.*, 2009, pp. 232-239.
- [64] C. Heising, F. Jie, R. Bartelt, V. Staudt, and A. Steimel, "Modelling of rotary converter in electrical railway traction power-systems for stability analysis," in *Electrical Systems for Aircraft, Railway and Ship Propulsion (ESARS), 2010*, 2010, pp. 1-6.
- [65] B. V. Jayawant, "Electromagnetic suspension and levitation," *Physical Science, Measurement and Instrumentation, Management and Education - Reviews, IEE Proceedings A*, vol. 129, pp. 549-581, 1982.
- [66] M. C. Marion-Pera and J. P. Yonnet, "Axial bearings using superconductors and permanent magnets," *Magnetics, IEEE Transactions on*, vol. 31, pp. 2112-2114, 1995.
- [67] C. Zhang, K. J. Tseng, and J. Zhou, "A compact and efficient flywheel energy storage system with integrated magnetic bearings," in *Power Electronics and Motion Control Conference, 2004. IPEMC 2004. The 4th International*, 2004, pp. 294-299 Vol.1.
- [68] J. A. Williams, "Friction and wear of rotating pivots in MEMS and other small scale devices," *Wear*, vol. 251, pp. 965-972, 2001.
- [69] D. P. Arnold, "Review of microscale magnetic power generation," *IEEE Transactions on Magnetics*, vol. 43, pp. 3940-3951, 2007.
- [70] L. Liwei, R. T. Howe, and A. P. Pisano, "Microelectromechanical filters for signal processing," *Microelectromechanical Systems, Journal of*, vol. 7, pp. 286-294, 1998.

- [71] F. Ayazi and K. Najafi, "A HARPSS polysilicon vibrating ring gyroscope," *Journal of Microelectromechanical Systems*, vol. 10, pp. 169-179, 2001.
- [72] G. M. Rebeiz, "RF MEMS switches: status of the technology," in *TRANSDUCERS, Solid-State Sensors, Actuators and Microsystems, 12th International Conference on, 2003*, 2003, pp. 1726-1729 vol.2.
- [73] S. C. O. Mathuna, T. O'Donnell, W. Ningning, and K. Rinne, "Magnetics on silicon: an enabling technology for power supply on chip," *Power Electronics, IEEE Transactions on*, vol. 20, pp. 585-592, 2005.
- [74] M. Rossi, *Acoustics and Electroacoustics*. Norwood, MA: Artech, 1988.
- [75] N. G. Stephen, "On energy harvesting from ambient vibration," *Journal of Sound and Vibration*, vol. 293, pp. 409-425, 2006.
- [76] N. R. Grossner and I. S. Grossner, *Transformers for electronic circuits*, 2nd ed. New York: McGraw-Hill, 1983.
- [77] B. D. H. Tellegen, "The gyrator, a new electric element," *Philips Research Report*, vol. 3, pp. 81-101, 1948.
- [78] P. R. Gray, *Analysis and design of analog integrated circuits*, 5th ed. New York: Wiley, 2009.
- [79] K. Halbach, "Design of permanent multipole magnets with oriented rare earth cobalt material," *Nuclear Instruments and Methods*, vol. 169, pp. 1-10, 1980.
- [80] R. J. Roark and W. C. Young, *Formulas for stress and strain*, 5th ed. New York: McGraw-Hill, 1975.
- [81] M. Imboden, P. Mohanty, A. Gaidarzhy, J. Rankin, and B. W. Sheldon, "Scaling of dissipation in megahertz-range micromechanical diamond oscillators," *Applied Physics Letters*, vol. 90, Apr 23 2007.
- [82] O. Cugat, J. Delamare, and G. Reyne, "Magnetic micro-actuators and systems (MAGMAS)," *IEEE Transactions on Magnetics*, vol. 39, pp. 3607-3612, 2003.
- [83] I. T. R. f. S. (ITRS). (2009). *2009 Edition Interconnect*.
- [84] M. Brunet, T. O'Donnell, L. Baud, N. N. Wang, J. O'Brien, P. McCloskey, and S. C. O'Mathuna, "Electrical performance of microtransformers for DC-DC converter applications," *IEEE Transactions on Magnetics*, vol. 38, pp. 3174-3176, Sep 2002.

- [85] C. R. Sullivan and S. R. Sanders, "Measured performance of a high-power-density microfabricated transformer in a DC-DC converter," in *Power Electronics Specialists Conference, 1996. PESC '96 Record., 27th Annual IEEE*, 1996, pp. 287-294 vol.1.
- [86] T. O'Donnell, N. Wang, M. Brunet, S. Roy, A. Connell, J. Power, C. O'Mathuna, and P. McCloskey, "Thin film micro-transformers for future power conversion," in *Applied Power Electronics Conference and Exposition, 2004. APEC '04. Nineteenth Annual IEEE*, 2004, pp. 939-944 vol.2.
- [87] K. Ki-Jin, L. Tae Ho, and K. H. Ahn, "The novel high efficiency on chip transformers for the CMOS power amplifier," in *Proceedings of the 12th International Symposium on*, 2009, pp. 401-404.
- [88] C. D. Meyer, S. S. Bedair, B. C. Morgan, and D. P. Arnold, "High-Inductance-Density, Air-Core, Power Inductors, and Transformers Designed for Operation at 100-500 MHz," *IEEE Transactions on Magnetics*, vol. 46, pp. 2236-2239, Jun 2010.
- [89] G. Ivensky, I. Zafrany, and S. Ben-Yaakov, "Generic operational characteristics of piezoelectric transformers," *IEEE Transactions on Power Electronics*, vol. 17, pp. 1049-1057, 2002.
- [90] "IEEE Standard on piezoelectricity," *IEEE Transactions on Ultrasonics Ferroelectrics and Frequency Control*, vol. 43, pp. A1-A54, Sep 1996.
- [91] A. Arnau, *Piezoelectric transducers and applications*, 2nd ed. New York: Springer, 2008.
- [92] A. Preumont, *Mechatronics: dynamics of electromechanical and piezoelectric systems*: Kluwer Academic Pub, 2006.
- [93] J. Hyun-Woo, L. Chang-Hwan, and J. Hyun-kyo, "Analysis of piezoelectric transformer by using finite element method and equivalent-circuit considering load variation," in *Ultrasonics Symposium, 2001 IEEE*, 2001, pp. 459-462 vol.1.
- [94] S. Priya, "High power universal piezoelectric transformer," *Ultrasonics, Ferroelectrics and Frequency Control, IEEE Transactions on*, vol. 53, pp. 23-29, 2006.
- [95] H. Kawai, Y. Sasaki, T. Inoue, T. Inoi, and S. Takahashi, "High power transformer employing piezoelectric ceramics," *Japanese Journal of Applied Physics Part 1-Regular Papers Short Notes & Review Papers*, vol. 35, pp. 5015-5017, 1996.

- [96] K. Tomalczyk, T. Swiatczak, and B. Wiecek, "Piezoelectric Transformer Efficiency Tests in a Digitally Controlled Converter Circuit," in *Mixed Design of Integrated Circuits and Systems, 2007. MIXDES '07. 14th International Conference on*, 2007, pp. 592-596.
- [97] Y. C. Wang, J. J. He, Y. P. Liu, J. Wu, C. K. Lee, and Y. T. Haung, "Theory and experiment of high voltage step-up ratio disk type piezoelectric transformer for LCD-TV," in *Mechatronics, 2005. ICM '05. IEEE International Conference on*, 2005, pp. 284-287.
- [98] V. Divakar, Y. Zhang, J. C. Zito, E. A. Salley, and D. P. Arnold, "Microelectromechanical inductors with high inductance density via mechanical energy storage," in *PowerMEMS 2011*, Seoul, Korea, 2011, pp. 181-184.
- [99] S. C. S. Inc. *SCS Parylene Properties Available*:  
<http://www.scscoatings.com/docs/coatspec.pdf>
- [100] W. H. Li, J. H. Ye, and S. F. Y. Li, "Electrochemical deposition of Copper on patterned Cu/Ta(N)/SiO<sub>2</sub> surfaces for super filling of sub-micron features," *Journal of Applied Electrochemistry*, vol. 31, pp. 1395-1397, 2001.
- [101] F. Laermer and A. Urban, "Milestones in deep reactive ion etching," in *Solid-State Sensors, Actuators and Microsystems, 2005. Digest of Technical Papers. TRANSDUCERS '05. The 13th International Conference on*, 2005, pp. 1118-1121 Vol. 2.
- [102] R. W. Erickson, D. Maksimovi\*\*, and Books24x7 Inc. (2004). *Fundamentals of power electronics, second edition (2nd ed.)* [Text].
- [103] F. E. Bisogno, S. Nittayarumphong, M. Radecker, and A. V. Carazo, "Dynamical Modelling of Class-E Resonant Converter for Step-Down Applications Using Piezoelectric Transformers," in *Power Electronics Specialists Conference, 2005. PESC '05. IEEE 36th*, 2005, pp. 2797-2803.
- [104] O. Ohnishi, Y. Sasaki, T. Zaitso, H. Kishie, and T. Inoue, "PIEZOELECTRIC CERAMIC TRANSFORMER FOR POWER-SUPPLY OPERATING IN THICKNESS EXTENSIONAL VIBRATION MODE," *Ieice Transactions on Fundamentals of Electronics Communications and Computer Sciences*, vol. E77A, pp. 2098-2105, Dec 1994.
- [105] T. Zaitso, T. Inoue, O. Ohnishi, and Y. Sasaki, "2 MHZ POWER CONVERTER WITH PIEZOELECTRIC CERAMIC TRANSFORMER," *Ieice Transactions on Electronics*, vol. E77C, pp. 280-286, Feb 1994.

- [106] S. Nittayarumphong, F. Bisogno, M. Radecker, A. Knoll, A. V. Carazo, and A. Riedlhammer, "Dynamic behaviour of PI controlled class-E resonant converter for step-down applications using piezoelectric transformers," in *Power Electronics and Applications, 2005 European Conference on*, 2005, pp. 10 pp.-P.10.
- [107] S. Nittayarumphong, F. Bisogno, M. Radecker, A. V. Carazo, A. Riedlhammer, and H. Guldner, "High efficiency control methods for class-E resonant converter for step-down applications using Piezoelectric Transformers (PT)," in *Power Electronics and Applications, 2007 European Conference on*, 2007, pp. 1-10.
- [108] R. Engleitner, F. E. Bisogno, J. R. Pinheiro, C. Rech, L. Michels, and M. Radecker, "Small-signal modeling of a DC-DC Class-E piezoconverter based on generalized averaging method," in *Industrial Electronics (ISIE), 2011 IEEE International Symposium on*, 2011, pp. 396-401.
- [109] S. Bronstein and S. Ben-Yaakov, "Design considerations for achieving ZVS in a half bridge inverter that drives a piezoelectric transformer with no series inductor," in *Power Electronics Specialists Conference, 2002. pesc 02. 2002 IEEE 33rd Annual*, 2002, pp. 585-590 vol.2.
- [110] M. Sanz, P. Alou, R. Prieto, J. A. Cobos, and J. Uceda, "Comparison of different alternatives to drive piezoelectric transformers," in *Applied Power Electronics Conference and Exposition, 2002. APEC 2002. Seventeenth Annual IEEE*, 2002, pp. 358-364
- [111] R. Liu, I. Batarseh, and C. Q. Lee, "Comparison of performance characteristics between LLC-type and conventional parallel resonant convertors," *Electronics Letters*, vol. 24, pp. 1510-1511, 1988.
- [112] R. Liu, C. Q. Lee, and A. K. Upadhyay, "Experimental investigation of the LLC-type parallel resonant converter," in *Applied Power Electronics Conference and Exposition, 1990. APEC '90, Conference Proceedings 1990., Fifth Annual*, 1990, pp. 723-732.
- [113] C. Jung-Hui and A. F. Witulski, "LLC parallel resonant converter design by scaling the LC converter," *Aerospace and Electronic Systems, IEEE Transactions on*, vol. 34, pp. 924-933, 1998.
- [114] R. Liu, C. Q. Lee, and A. K. Upadhyay, "A multioutput LLC-type parallel resonant converter," *Aerospace and Electronic Systems, IEEE Transactions on*, vol. 28, pp. 697-707, 1992.
- [115] S. Cheng, N. Wang, and D. P. Arnold, "Optimization of magnetic vibrational energy harvesting systems using equivalent circuit representations," presented at the PowerMEMS 2007, Freiburg, Germany, 2007.

## BIOGRAPHICAL SKETCH

Shuo Cheng was born in Jiangxi, China in 1985. He earned his Bachelor of Engineering Degree in automation from Beijing Institute of Technology in China in 2006, and Master of Science Degree in electrical and computer engineering from the University of Florida in Gainesville, FL in 2009. He is a Ph.D. candidate in electrical and computer engineering at the University of Florida in Gainesville, FL.